A FACILE HYBRID METHOD TO SYNTHESIZE METAL AND METAL CHALCOGENIDE NANOPARTICLES USING VARIOUS CAPPING GROUPS

Submitted to the Faculty of Science and Agriculture by

Nhlakanipho Mntungwa

20022499

In fulfilment of the requirement for the award of the degree of

Doctor of Science

in the Department of Chemistry

University of Zululand

Supervisor: Prof. N. Revaprasadu

Co-Supervisor: Dr V. S. R. Rajasekhar Pullabhotla

University of Zululand

Private bag X1001

KwaDlangezwa

3886

June 2014

DECLARATION STATEMENT

‘‘I hereby declare that the work on **A FACILE HYBRID METHOD TO SYNTHESIZE METAL AND METAL CHALCOGENIDE NANOPARTICLES USING VARIOUS CAPPING GROUPS** is my own work and that all the sources I have quoted have been indicated and acknowledged by means of complete references.’’

……..……..

NHLAKANIPHO MNTUNGWA (20022499)

ACKNOWLEDGEMENTS

A special thanks to my family members who through their patience allowed me to pursue my academic career. This journey was challenging but I was able to succeed and climb to the mountain top. For this I reject not my absence from home to another home far away. Both the young and old are together and in the midst of challenges stood the test of time by continuing to be united. These are people who have something to offer in order to accomplish a certain goal and nurture the vision.

My appreciation goes to Prof. Neerish for his supervision and for all the knowledge gained through his guidance. For the record since I started tertiary education, I have learnt a lot from him under different circumstances. We enjoy most of the time during the working hours and were able to spend quality time away from the campus as means of relaxation. His wife is a blessing from the time we met and a supportive person and a helper of the people. They are blessed with cute little triplets which are able to keep you company as they enjoy playing and seem not afraid of strangers. The kids are growing from strength to strength everytime you meet them.

My sincere gratitude is towards Dr Raj to learn from him to be where I am today. He helped me to improve in research related matters. Through his diligence I analysed the situation and task confronted, having to work swiftly and achieve both long term and short term goals. There a lot done during the period of my studies that was successful and without desired achievement but without given up. In this manner I would like to show appreciation to him for being supportive and being catalyst to make sure I complete all the assignments expected from me.

A special thanks is for my family members at Machibisa near Natshi Road in Pietermaritzburg. There was taught to have a vision and put myself in line with it so that at the end of the day I would win and climb higher. These people are recognized according to the heirachy which is based on the age where respect must be given. My granny there is always greatful when we meet and want to give, share and encourage you not to give up. We respect her for being there as iMbokodo in this family of KwaMahlaba. Uncle Mali is available for help and gives guidance to manhood situation. His wife is a wonderful person with their child as a blessing and a brother to me.

There is a person with a heart of wisdom that can understand the situation that I am facing because there is no other home that someone can live in without any problem but these are temptations in which there is no definite reason to declare them without a sacrifice. This is because of the science that is beyond recognition where the person is not really attached to some very special and true. This is to say good and all the best to the one who is to join the family and I continue to recognize the potential of the person who is the bread winner where they is a problematic situation that we face as a family without causing the division in our home. The person will live together in harmony and abide with the one who he is attached to physically and emotionally.

I would like to say thank you all who has done good to me and brought the happiness that I have to day which is the gift that is beyond recognition but put the effort that is not always there to guide and fellowship with the love that is bought with a price of effort and dedication to the

service that the leader will continue to bring forward. There is a special gift I have made to the people here and I say good luck to the ones who helped me to be where I am today.

ABSTRACT

The synthesis of bismuth (Bi), antimony (Sb) and tin (Sn) metal and metal chalcogenide nanoparticles is presented using a novel hybrid solution based high temperature method. Furthermore is the synthesis of zinc telluride (ZnTe) and cadmium telluride (CdTe) nanostructured materials also described. The nanomaterials are predominantly capped by organic ligands. The use of water soluble ligands such as triethanolamine (TEA) and cysteine is also reported. The synthetic method involves the reduction of a metal salt followed by the introduction of the chalcogenide source in the case of metal chalcogenide nanoparticle synthesis. The metal or metal chalcogenide prepared is thermolysed into a high boiling point ligand at high temperature. For the water soluble nanoparticles after reduction there is a simultaneous addition of a chalcogenide source and a ligand at room temperature.

The Bi and Sb nanoparticles showed similar spherical morphology when capped with tri-*n*-octylphosphine oxide (TOPO). Bismuth particles in the form of dots, branched nanorods and self assembled cubes were obtained at different reaction conditions. The cubed shaped Bi and Sb nanoparticles which appear to self-assemble were obtained when using oleylamine (OA) as a capping group. The Bi_2S_3, Bi_2Se_3 and Bi_2Te_3 nanoparticles were elongated when capped using alkylamines such as hexadecylamine (HDA) and OA, however at low temperature of 90^{o}C they appeared to be close to spherical. The antimony chalcogenides, Sb_2S_3, Sb_2Se_3 and Sb_2Te_3 gave a similar rod shape morphology. The Sn nanoparticles appeared aggregated to some extent. A triangular shaped morphology is observed for the OA capped SnS nanoparticles.

HDA capped ZnTe nanoparticles were synthesized using NaHTe and $ZnCl_2$ as the tellurium and zinc sources respectively. The particles synthesized at reaction temperatures of 230 ^oC and 270 ^oC were spherical in shape. The blue shift in the absorption spectra confirms that the particles undergo quantum confinement. The photoluminescence studies show that the particles emit at a wavelengths close to their band edge. The water soluble cysteine and TEA capped ZnTe particles appear as nanorods which are aggregated. Finally water soluble CdTe nanoparticles were synthesized using TEA and cysteine as capping groups. The results showed that both cysteine and TEA are effective capping groups for water soluble CdTe nanoparticles. The optical properties of the particles synthesized in both capping groups revealed absorption features due to the Cd-ligand complex. The photoluminescence spectra showed reasonably narrow emission peaks. The cadmium salt was varied to study its effect on the morphology of the CdTe nanoparticles. The nitrate source gave well defined, crystalline, close to spherical nanoparticles. The FT-IR measurements confirmed the presence of the capping ligand on the surface of CdTe nanoparticles.

LIST OF FIGURES

LIST OF ABBREVIATIONS AND SYMBOLS

CHEMICALS

$NaBH_4$	Sodium borohydride
HDA	Hexadecylamine
TOPO	Tri-octlyphosphine oxide
TOP	Tri-octlyphosphine
Bi_2S_3	Bismuth sulfide
Bi_2Se_3	Bismuth selenide
Bi_2Te_3	Bismuth Telluride
$ZnCl_2$	Zinc chloride
CdS	Cadmium sulfide
ZnS	Zinc sulfide
PEI	Polyethyleneimine
DT	1-dodecanethiol
P3HT	Poly(3-hexlythiphene)
EG	Ethylene glycol
TAA	Thioacetamide
OA	Oleic acid
DMF	Dimethyl formamide
CdSe	Cadmium selenide
CdTe	Cadmium telluride
Au	Gold
TEA	Triethanolamine
$(CH_3)_2Cd$	Dimethylcadmium
OAm	Oleylamine

$Cd(Mer)_2$	Cadmium 2-mercaptobenzothiazole complex
HPA	Hexylphosphonic acid
TDPA	Tetradecylphosphonic acid
$CdCl_2$	Cadmium chloride
$CdSO_4$	Cadmium sulfate
$Cd(CH_3COO)_2$	Cadmium acetate
$CdCO_3$	Cadmium carbonate
PbTe	Lead telluride
CNT	Carbon nanotubes
Ag	Silver
Bi	Bismuth
Ag	Antimony
Sn	Tin
Cu	Copper
Al	Aluminium
S	Sulphur
Se	Selenium
Te	Tellurium
$Bi(C_2H_3O_2)_3$	Bismuth acetate
$Bi(NO_3)_3$	Bismuth nitrate
$Bi_2(CO_3)O_2$	Bismuth carbonate oxide
$SbCl_3$	Antimony chloride
$Na_2S_2O_3.5H_2O$	Sodium thiosulfate pentahydrate
Sb_2Te_3	Antimony telluride
Sb_2Se_3	Antimony selenide

Sb_2S_3	Antimony sulphide
SnS	Tin sulphide
$Sn(OH)_2$	Tin hydroxide
SnO_2	Tin dioxide
$Sn[N(SiMe_3)_2]_2$	Tin bistrimethylsilyl amine
TOPS	Tri-noctylphosphine sulfide
HMDS	Hexamethyldisilazane
$Sn_6O_4(OH)_4$	Tin oxide hydroxide
$SnCl_2$	Tin chloride
ZnTe	Zinc telluride
MAA	Mercaptoacetic acid
MPA	Mercaptopropionic acid
TGA	Thioglycolic acid
HCl	Hydrochloric acid
NH_3	Ammonia
$BiCl_3$	Bismuth chloride
PbS	Lead sulfide
PbSe	Lead selenide

TECHNIQUES AND METHODS

TEM	Transmission electron microscopy
XRD	Powder X-ray diffraction
FTIR	Fourier transform infrared spectroscopy
AFM	Atomic force microscopy
DLS	Dynamic light scattering

XPS	X-ray photoelectron spectroscopy
NMR	Nuclear magnetic resonance
EDS	Energy Dispersive X-ray Spectroscopy

SYMBOLS AND CONSTANTS

T_m	melting points of a bulk material
ΔH	molar latent heat of fusion
ρ	density
m_e	mass of electron
m_h	mass of hole
ϵ	dielectric constant
$\hbar$	Planck constant
λ	Wavelength
θ	Theta
Å	Angstroms

CHAPTER ONE

INTRODUCTION

CHAPTER TWO

BISMUTH NANOPARTICLES

CHAPTER THREE

BISMUTH CHALCOGENIDE NANOPARTICLES

CHAPTER FOUR

ANTIMONY AND ANTIMONY CHALCOGENIDE NANOPARTICLES.

CHAPTER FIVE

TIN AND TIN SULFIDE NANOPARTICLES

CHAPTER SIX

ZINC TELLURIDE NANOPARTICLES

CHAPTER SEVEN

CADMIUM TELLURIDE NANOPARTICLES

CHAPTER EIGHT

RECOMMENDATIONS

1.1 The history of nanotechnology

Michael Faraday was the first scientist to experimentally make gold colloidal nanoparticles which started the field of nanoscience and nanotechnology. He reported the metallic nanoparticles in 1847 where he discovered that their optical properties are different from the bulk materials. The colloidal nanoparticles includes paint, mud, toothpaste which are finely dispersed in a suspended mixture. Faraday made attempts to explain the vivid colour change in the gold mixture where this phenomena seemed to indicate variation in size of the nanoparticles of gold giving rise to variety of resultant colors [1,2]. He could not explain why the colour of the gold nanoparticles change with size but describe this work as a useful entrance into certain physical investigation respecting nature and action of a ray of light. This concept was further introduced in a lecture in 1959 which was published in 1960 presented by Richard Feynman a Nobel laureate [3]. He said "the principles of physics, as far as I can see, do not speak against the possibility of maneuvering things atom by atom'. This definition was expanded by Drexler in most stimulating and lateral thinking way in his book named *Engines of Creation, the Coming age of nanotechnology* [4]. The definition was quoted as 'nanotechnology is the principle of atom manipulation atom by atom, through control of the structure of matter at the molecular level. It entails the ability to build molecular systems with atom-by-atom precision, yielding a variety of nanomachines'. The theory by Dexler was expanded by Binnig and Rohrer in a practical way in 1981 where they were the first to see atoms. Other scientists were able to build up on their work where the term of nanotechnology became appreciated and interestingly increased and became more broadly applied to any technique that works and can be understood at a nanometer level.

1.2 Background on nanotechnology

Particles are made up of two or more atoms/molecules (basic units of matter) that behave as a whole unit in terms of their properties. They are classified in terms of their size such as bulk particles and nanoparticles with diameter in micrometers (1 μm = 10^{-6} m) and nanometers (1 nm = 10^{-9} m) scale, respectively. Nanoparticles have attracted fundamental and industrial research for the past two decades. These materials are not new, because they were used for generating a glittering effect on the surface of pots many centuries ago [5]. Their novel properties make them useful in various potential applications. Nanoparticles are unique when compared to the corresponding bulk particles due to two reasons. Firstly, nanoparticles have size dependent properties whereas bulk particles possess constant physical properties regardless of their size [6]. Secondly, the percentage of atoms at the surface of a nanoparticle is significant because of large surface area, but for bulk particles, the percentage of atoms at the surface is insignificant in relation to the number of atoms in particles [6]. Therefore, size and surface of the nanoparticles can easily get affected if they are not kept in a suitable environment resulting in the change of their physical and chemical properties. But this is not the case with bulk materials because their size does not affect confinement.

Nanoparticles are formed through the combination of a core and a ligand whose function is to keep the material in the nanoscale. However some particles are prepared with or without a ligand on their surface. The functionalization of the nanoparticle's surface is necessary in maintaining their properties which is facilitated by the capping group. The capping group stabilizes the surface, determines the solubility of the particles and can be used for targeting [6-10]. This prevents nanoparticles from aggregation which also controls the size and shape of the particles

[7,8]. In addition, it renders them soluble in polar and/or nanopolar solvents which make them useful in electronics and biology [9-11].

The importance of nanoparticles has already been demonstrated in various applications. The interesting properties of nanomaterials create more room of research for their future applications with other possible strategies to develop the global economy in order to make the world a better place. This is brought by the fundamental role that is there as a guidance to help the society at large to understand the greener environment that is partitioned by many functional materials. It is obvious that in order to fully understand the potential of these nanoparticles individually, more progress is needed in their synthesis and an understanding of their basic properties. This is due to the structure of the material in study. Thus more research is pursued on the synthesis of different nanomaterials with different kind of substances being more stable than the other unstable material in research as a whole. There are several synthetic methods to obtain nanoparticles with different characteristics which operate in a unique manner as to make the substances more available, used and produced in different forms [12]. The top-down and bottom-up approaches are the two strategies used.

1.3 Properties of nanomaterials

1.3.1 Quantum size effect

When the size of a single crystalline nanoparticle is smaller than the de Broglie wavelength, electrons and holes are spatially confined forming discrete electronic energy levels [13]. The energy separation between adjacent levels increases with decreasing dimensions similar to a particle in a box. The electronic configurations of nanomaterials are significantly different from

that of their bulk counterpart as shown in Fig.1.1. This is due to the possible formation of the nanostructures that are not very stable at the nanoscale because of the surface energy related to the atoms and ions at their surface. These changes are due to the transformations in the density of electronic energy levels as a function of size which results in strong variations in the optical and electrical properties with size. The quantum size effect will be continually discussed in more detail later in the chapter.

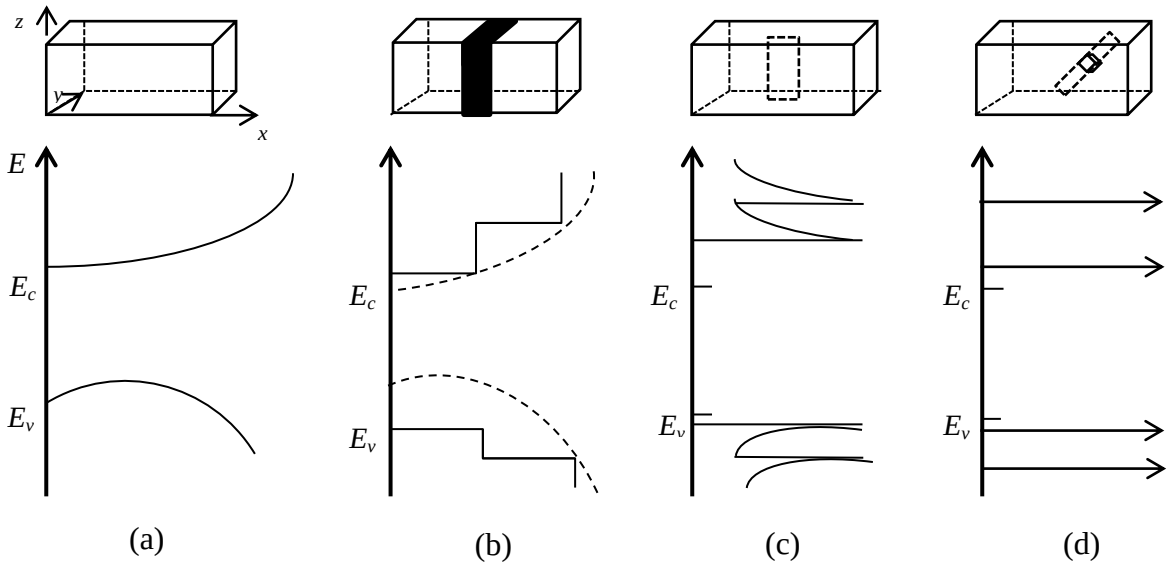

Fig. 1.1 The discrete electronic configurations in nanocrystals, nanowires and thin films and enlarged band between valence band and conduction band [13].

1.3.2 Surface-to-volume ratio

The majority of atoms in the nanomaterials are located on the surface of the particles while for bulk materials they are found inside the micro sized particles as shown in Fig.1.2.

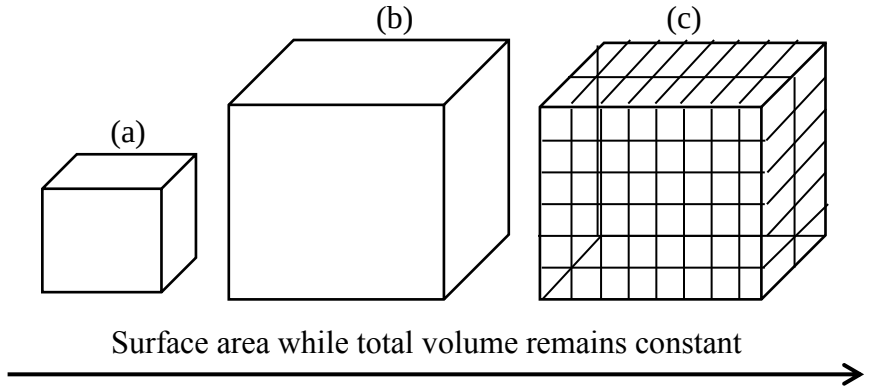

Fig.1.2 Diagram showing (a) a small particle, (b) large particle and (c) large particle consisting of the particles, which indicate how the surface are increased as the particle size is reduced.

The different environments of the component particles make the properties of these materials unique in that nanoparticles have a high surface area. The nanomaterials have enhanced chemical, mechanical, optical and magnetic properties which can be observed using different techniques. For example, the individual nano-sized particles of materials made from metal and oxides of silicon and germanium exhibit superplastic behavior undergoing elongations from 100 to 1000 per cent before failure because they expand relative to each other during aerospace and automotive applications. There are sometimes strong, hard and ductile at high temperatures while others are chemically very active due to the large number of surface molecules or atoms. In order to retain the desired properties of these nanomaterials, a stabilizer is used to protect their surface.

1.4 Electronic properties

1.4.1 Optical properties

An electron and hole pair is created when a photon of light is absorbed forming a so called exciton. In semiconductors, this is favoured by the small effective masses of electron (m_e) and hole (m_h) and the large dielectric constant (ϵ) with the large exciton on the atomic scale where

Bohr radii (a_0) is between 5 nm and 50 nm which can be calculated using this expression given below in eqn.1.2 [14].

$$a_0 = \frac{h^2 \epsilon}{e^2} \left[\frac{1}{m_e} + \frac{1}{m_h} \right] \quad (1.2)$$

When the size of a semiconductor in any dimension is comparable with a_0 or the de Broglie wavelength $\lambda_{dB} = h/mv$, changes in the optical properties are observed. This effect is observed for very small metals of a few nanometers on account of no band gap and the corresponding small distance between relevant energy levels. The change of the electronic density of a semiconductor in a quantum dot (zero dimension) (Fig. 1.1a) has discrete energy levels, the quantum wire (one dimension) (Fig. 1.1b) quasi-discrete and the quantum well (two dimension) (Fig. 1.1c) a quantized stairs pattern (see Fig.1.1 above). The bulk has a continuous band (Fig.1.3) [14].

As mentioned in section 1.3, the two fundamental factors are related to the size of the individual nanocrystal, the first being the high dispersity associated with the particles where both the physical and chemical properties of the semiconductor being particularly sensitive to the surface structure. The second factor is the actual size of the particle which can determine the electronic and physical properties of the material. The Mie's theory describe the absorption and scattering of incident light in larger colloidal particles. But the optical spectra of nanocrystalline compound semiconductors which show blue shifts [6,15-21] in their absorption edge as the size of the particle decreases cannot be explained by classical theory [22-25].This occur when the size of the nanoparticle is smaller than the bulk-exciton Bohr radius, a_B (eq.1.2) of the semiconductor.

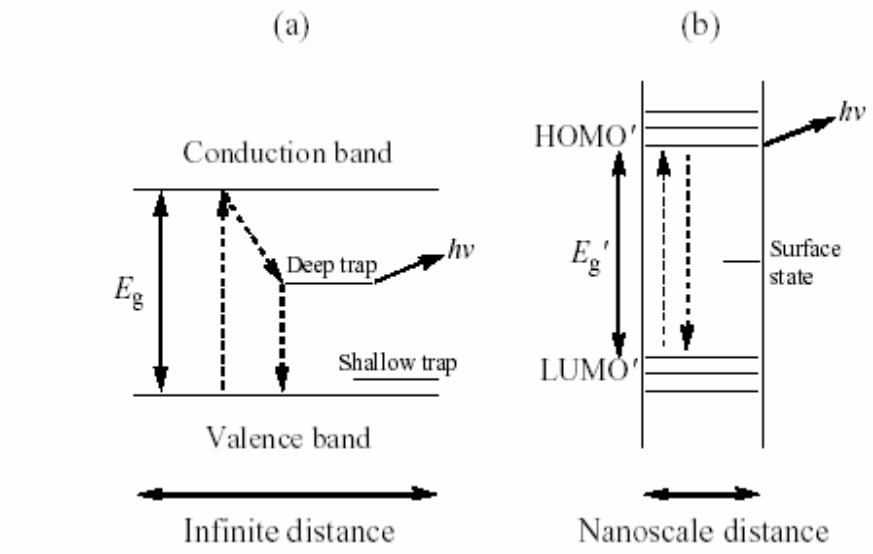

Fig.1.3. The spatial electronic state diagram showing the quantum confinement effect in bulk semiconductors (a) and nanoparticles (b)[26].

The correlation between the energy of the band gap and the size of the nanoparticles has been explained by Brus *et al.* [27] who described the energy levels of the first excited state by being conscious of the coulomb interaction and polarization terms. In this approach, the valence and conduction band are assumed to be parabolic near the band gap for the difference in energy of the first excited state, relative to the bulk. An equation which follows was proposed for the size-dependent shifts with respect to the bulk band gap energy (eqn.1.3).

$$\Delta E = \frac{\hbar^2 \pi^2}{2R^2}\left[\frac{1}{m_e^*} + \frac{1}{m_h^*}\right] - \frac{1.786e^2}{\varepsilon R} - 0.248E^*_{RY} \qquad (1.3)$$

Here the first term is the particle-in-a-box localization energy, which depends quadratically on ($\hbar^2\pi^2$) with a $1/R^2$ dependence, where R = radius of the particle, ħ = Planck constant, m_e* = effective mass of the electron, and m_h* = effective mass of the hole.

It can be seen from the equation above that the ΔE is inversely proportional to the effective mass and the square of the radius. The second term describes the coulombic interaction of the electron and the hole, where ***e*** is the universal charge, ε is the dielectric constant of the material in question and $\mathbf{E^*_{RY}}$ is the Rydberg energy. Good correlation between theory and experiment has been obtained within this model for larger nanoclusters. In the case of smaller particles, especially those smaller than ~ 2 nm, the lowest excited state are located in a region of the energy band that is no longer parabolic and as a result, the effective mass approximation breaks down. For these particles a more molecular approach referred to as the high-binding model, which is based upon the linear combination of atomic orbital's, is favoured.

1.4.2 Structural properties

The crystal structure of the nanoparticles may differ from that of corresponding bulk materials. This size-dependent transition have been observed in In, Si, and Cr metals [28]. The small particles have a high curvature and then surface tension of a solid-vapor or liquid-vapor interface acts as a significant pressure on the particles. If the pressure on a particles due to surface forces were large enough then the particle would be expected to undergo a phase change. For example, bulk Bi requires ~2-GPa pressure to transform from the rhombohedral structure to the body-centered-monoclinic structure. But Bi above 4.2 nm exhibited a combination of the bulk rhombic and cubic crystal structures.

The particle shapes are closely related to the crystal structure of the surface that surrounds the particles. The surface of the metal particle which has hexagonal structure appears different in the

surface atom densities, electronic structure, bonding and possibly chemical reactivities. Energies in the surface of these materials which is associated with different crystallographic planes are usually different. There is higher surface energy in a spherical crystalline particle because of high index crystallography planes. Facets tend to form on the particle surface to increase the portion of the low-index planes. There are factors such as capping ligand, molar ratio of the precursors, and growth rate that influence the particles to grow toward some selected directions to get the final shapes [29].

1.4.3 Electrical conductivity

The purity of the material, structural defect and dislocations can affect the electrical conductivity of nanostructures or nanomaterials. However, there are complex effects of size on electrical conductivity which are distinct mechanisms such as surface scattering which are grain boundary scattering, quantized conduction with ballistic, coulomb charging, tunneling, widening, discrete of band and change of microstructures. All these characteristics will occur due to the change in the electronic structure of the material [30]. The change in the band gap will automatically favor a reduction in electrical conductivity of a material. Some metals undergo a transition to become semiconductors when their size is reduced to nanoscale due to quantum size effect. In the case of single crystalline Bi nanowires, they undergo a metal-to-semiconductor transition at a diameter of ~52 nm and the electrical resistance of Bi nanowires of ~40 nm decreased with decreasing temperature [31,32]. The silicon nanowires of ~15 nm appear insulating while GaN nanowires of 17.6 nm in diameter were semiconductors [33-35].

1.4.4 Catalytic properties

The chemical reactivity of the nanomaterial can be changed due to their different structures and surface to volume ratio. These nanomaterials are sometimes used as catalyst which increase the rate, selectivity and efficiency of chemical reactions like combustion or synthesis which can reduce waste and pollution [36]. Their very high, very controllable, reactive surface are renders ideal for this function. The catalytic activity for the gold nanoparticles smaller than 5 nm was increased by the structural change from icosahedral rather than normal face centered cubic. The nanoscale catalytic supports with controlled pore size can select the products and reactants of chemical reactions based on their physical size and thus ease of transport to and from internal reaction site within the nanoporous structure. Some materials act as medicines that are insoluble in water when in the form of bulk particles instead they easily dissolve when there are in the nanostructural form.

1.5 Synthetic Routes to Nanoparticles

There have been many reported synthetic routes to nanoparticles. The ideal synthetic route should incorporate attributes such as environmentally friendliness, cost effectiveness, lower reaction temperature and ease of preparation. The size, shape, crystallinity and structure of the nanoparticles should also be controlled as these are requirements for different applications.

The colloidal and organometallic methods are the mostly preferred, popular and efficient methods for the synthesis of a wide variety of nanomaterials and as such these two routes will be review. Much of the synthesis work has focused on cadmium chalcogenide materials and thus

these ought to be reviewed in this thesis. The extent of the work is too vast to include all nanomaterials.

1.5.1 Colloidal route

The colloidal method for the synthesis of metal chalcogenide nanoparticles, involves the reduction of the chalcogenide present in a solution by a suitable reducing agent. There are some cases where a source of a chalcogenide or a metal is a complex where their corresponding ions or ionic solution are prepared separately [37,38]. Precipitation is achieved in a homogeneous solution containing reduced chalcogenide ions and metal salt in the presence of the ligand [39]. The ligand prevents agglomeration and seeds are allowed to grow into larger particles. By controlling nucleation and growth processes monodispersed nanoparticles are obtained. The nanoparticles grow by Ostwald ripening mechanism whereby small less stable crystals dissolves and recrystallize into large more stable particles [40,41]. This method is successful under certain conditions such as a good choice of solvents, pH and passivating agent since the nanoparticles produced must have low solubility.

The work by Brus and co-workers based on CdS and ZnS led to high level of interest in semiconductors that show quantum confinement [42]. They prepared CdS nanoparticles by a process involving the controlled nucleation of CdS in dilute aqueous solutions of cadmium sulphate and ammonium sulphide. The CdS produced by using acetonitrile as a solvent had average particle sizes of 3.4 nm to 4.3 nm with styrene or maleic anhydride as copolymers respectively. Some of the post-preparative separation techniques such as size exclusion and gel electrophoresis need to be employed in order to obtain highly monodispersed nanoparticles [43].

A simple route to polyethyleneimine (PEI) capped CdS and ZnS nanostructures with sizes about 7-53 and 4-17 nm respectively, have been reported by Hassan and Ali [44]. Cost effective starting materials such as $CdCl_2$ or $ZnCl_2$ and Na_2S solutions were employed. The hyperbranched polymer proved to be a suitable capping agent and/or surfactant for the synthesis of nanoparticles of these metal sulfides. The Revaprasadu group reported cysteine capped CdSe, CdTe and Au-CdSe hybrid core-shell nanoparticles by using a facile one-pot synthetic route [45-47]. The chalcogenides are reduced by sodium borohydride ($NaBH_4$) followed by simultaneous addition of metal source and capping ligand. Reaction parameters such as pH, temperature and mole ratio of starting material were varied to study their effects on the morphology and optical properties. Shang *et al*. [48] reported a simple method for creating stable water soluble CdSe QDs by replacing the oleic acid chains with highly water soluble triethanolamine (TEA). Based on the quenching of fluorescence signals of the functionalized CdSe QDs, a simple and specific method for the reciprocal recognition of mercury (II) and /or iodine (I) ions was proposed with wide linear range, low detection limits and good precision. Like most synthetic methods, colloidal methods have a drawback since the are low temperature methods and annealing of the colloidal particles is not possible. The nanoparticles produced by this method are not sufficiently stable at high temperature thus making them poorly crystalline. These problems can been overcome by using organometallic methods.

1.5.2 Hot-Injection/Organometallic Route

The organometallic route or 'hot injection route' involves injecting precursors that undergo pyrolysis at high temperature into a high boiling point stabilizing surfactant. The ratio of the

precursors, type of surfactant, type of solvent, reaction temperature and reaction time are usually the main parameters for controlling nanoparticle growth. This route was made popular by Murray *et al*. by producing cadmium chalcogenide nanoparticles (CdS, CdSe and CdTe) with dimethylcadmium $(CH_3)_2Cd$ and chalcogenide (X = Se, S and Te) both dissolved in tri-n-octylphosphine (TOP) as precursors which were reacted in hot tri-n-octylphosphine oxide (TOPO) as a capping agent [49]. The introduction of the concentrated reagents resulted in abrupt supersaturation and formation of nuclei followed by slower growth and annealing typical of Ostwald ripening. The particle size can be controlled by varying the temperature and time of reaction. The use of $(CH_3)_2Cd$ which is a volatile and highly toxic substance is a limitation to this method. This has led to the development of alternative chemical routes to nanoparticles.

The single-molecule precursors which contain both the metal and chalcogenide in one compound proved to be successful for the synthesis of high quality nanoparticles. Trindade and O'Brien reported for the first time cadmium dithio- and diselenocarbamate complexes as precursors for the synthesis of tri-octylphosphine oxide (TOPO) capped II/VI semiconductor nanoparticles [50,51]. This method involves the dispersion of the single source precursor in TOP followed by injection into hot TOPO at 250 ^{o}C. The single molecular source method for the formation of nanoparticles is consistent with the Lar Mer mechanism for colloids [39]. The nanoparticles are isolated by a non-solvent (methanol) which increases the average polarity of the solution and consequently decrease the energy barrier to flocculation. The precipitate is separated by centrifugation and redispersed in toluene to give an optically clear solution of TOPO-capped nanoparticles.

When using oleylamine (OA) as the coordinating solvent instead of TOPO, Geng *et al*. [52] thermolysed cadmium 2-mercaptobenzothiazole complex $Cd(Mer)_2$ (Mer = $C_6H_4NS^-$) to synthesize CdS nanoparticles of various sizes. The size of the CdS nanoparticles could be easily controlled by adjusting the ratio of OA/$Cd(Mer)_2$ under inert atmosphere. The studies on the optical properties of the nanocrystals displayed an obvious size-dependent photoluminescence characteristic. The Revaprasadu group reported the use of heterocyclic dithiocarbamate complexes for the synthesis of hexadecylamine (HDA) and TOPO capped CdS nanoparticles [53,54]. Elongated CdS nanoparticles in the form of rods, bipods and tripods were obtained when using HDA while only spherical nanoparticles were observed by using TOPO. The XRD measurements revealed the dominance of hexagonal structure of CdS. Literature shows that there is still a need for greener method to avoid the use of pryrophoric precursors and reduce hazardous materials.

Peng and Peng reported a method using cadmium oxide (CdO) instead of $(CH_3)_2Cd$ for the synthesis of high quality CdTe, CdSe and CdS nanocrystals [55]. In this method, TOPO was employed with either hexylphosphonic acid (HPA) or tetradecylphosphonic acid (TDPA) at temperatures above 270 ^oC. They tried to use cadmium chloride ($CdCl_2$) and cadmium sulphate ($CdSO_4$) which generated only bulk-sized CdSe particles. Qu *et al*. [56] used other cadmium sources in addition to the ones used by Peng such as cadmium acetate [$Cd(CH_3COO)_2$] and cadmium carbonate [$CdCO_3$] in the presence of different solvents, like fatty acids and amines for the synthesis of CdSe nanoparticles. However, there is room for more new synthetic routes and/or modifications to these methods to avoid the use of additional chemicals and/or ligands.

1.5.3 The hybrid solution based high temperature route

This route is based on a simple previous route developed by Rao *et al*. for the synthesis of t-Se nanorods [57]. Selenium powder was prepared through the reduction process which is based on the synthetic route by colloidal method. This is brought by the active reductant that is there and the metal source in the method which is in the solution. The strategy pertained the hot injection route which is the degradation of bulk metal chalcogenide such as CdSe or CdTe. This is typical of the hot injection technique that is found to be very productive in the making of highly crystalline nanomaterials. This method will be used to synthesize the nanoparticles that are reported in this thesis.

The method was successfully developed by the Revaprasadu group for the synthesis of various metal chalcogenides nanoparticles such as CdSe, CdTe and PbTe [58-61]. The cadmium and lead salts were chosen as metal sources for the synthesis of CdSe, PbTe and CdTe nanoparticles. These metal precursors were environmental friendly, less reactive and relatively inexpensive. In the case of CdSe, spherical TOPO-capped CdSe nanoparticles were synthesized by using $CdCl_2$ and $CdSO_4$ [58]. However, when $CdCO_3$ is used as the cadmium source, rod shaped particles are obtained for both TOPO and HDA-capped CdSe [58]. A similar trend was observed for PbTe synthesized by the same method [59,61]. The chloride and nitrate lead salts only produced spherical particles whereas the carbonate source gave distinct well aligned rods at reaction temperatures of 230 and 270 ^{o}C. The explanation given for this finding was that the suspension of the lead carbonate formed a shell of PbTe on its surface. This idea was confirmed by the FT-IR measurement on the intermediate. On injection, decomposition of the carbonate with subsequent kinetically controlled decomposition occurs, leading to the formation of anisotropic PbTe particles. For CdTe, close to spherical nanoparticles were obtained by using cadmium

chloride as cadmium source [60]. By changing the cadmium source to cadmium acetate, nitrate and carbonate, the morphology of the nanoparticles was altered. The appearance of close to spherical or rod-shaped particles is due to the mechanism of growth associated with the variation of cadmium source and reaction temperature. The growth of the nanoparticles occurred by orientated attachment mechanism when cadmium acetate and nitrate were used while Ostwald ripening growth of nanoparticles was observed for cadmium carbonate.

1.5.4 Other routes

1.5.4.1 Hydrothermal synthesis

This method have been widely used since the 1960s for the synthesis of a variety of functional nanomaterials with desired size and shapes [62]. The method uses water as a reaction medium where they are heated to a desired temperature to promote a reaction in sealed steel pressure vessels with Teflon liners in Fig.1.4.

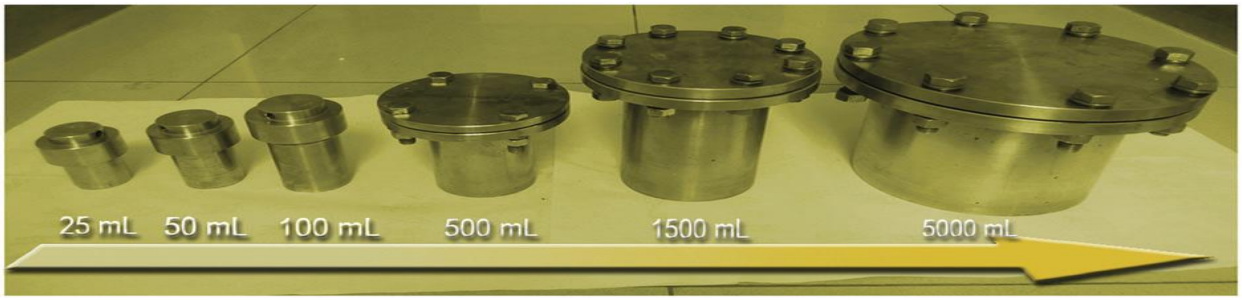

Fig.1.4 Teflon-line stainless steel autoclave with different volumes. It was taken with permission from the Yu Lab at the University of Science and Technology of China.

The temperature adopted is often above 100 ^{o}C in order to reach the pressure of vapor saturation so that autogeneous pressure will be developed in a closed system. The in situ generated pressure

within the reactor not only depend on the reaction temperature, but also relies on other experimental factors such as amount of liquid added and any dissolved salts. The use of water favours the solubility of many inorganic salts containing the source of the metal ions. This medium is beneficiary to introduce small coordinating molecules like ethylenediamine, hydrazine hydrate, ethylenediamine tetraacetic acid and polyvinylpyrrolidone to adjust the growth of the final nanocrystals.

The bulk prismatic single crystals of M_2S_3 (M = Sb, Bi) has been reported via a hydrothermal process [63]. The precursors were $SbCl_3$ or $BiCl_3$ and sulphur in the presence of diethylammonium chloride (DEACl) or tetraethylammonium chloride (TEACl). The optimal reaction conditions were temperatures above 180^{o}C and reaction time longer than 7 days. The nanorods were also prepared in the same way in the presence of hydrazine hydrate. DEACl or TEACl as weak reducing agent plays a very important role in the growth of M_2S_3 single crystals.

Alemi *et al*. [64] used a hydrothermal method to prepare antimony sulfide nanorods by reacting elemental sulphur antimony and iodine as precursors at 180 ^{o}C for 24 h. The structure for the nanorods was rhombohedral. The nanorods had length of 4 μm and diameter of about 50-140 nm. The band gap was around 2.50 eV which is blue shifted as compared to the bulk material. The atomic ratio of 2:3 for Sb:S was obtained as observed using the quantification of energy-dispersive X-ray spectrometry analysis.

A simple one pot hydrothermal route has been reported by Zhang *et al*. [65] for the synthesis of bismuth sulphide nanoparticles with a size of 80-100 nm in length. The staritng material used

were bismuth nitrate $Bi(NO_3)_3.5H_2O$ and L-cysteine. The bismuth nanoparticles were used to form a composite with the reduced grapheme oxide (RGO). The reagents were stirred in water for 10 min at first, then transferred into an autoclave where they were heated at 180 ^oC for 12 h. The Bi_2S_3/RGO composite exhibited a capacity of 1073.1 $mAhg^{-1}$ with good cyclic stability when the electrochemical test was carried.

1.5.4.2 Solvothermal methods

The method is like that of hydrothermal method which uses different organic solvents other than water [62**]**. These are based on the fact that the solvent properties such as polarity, viscocity and softeness have strong effect on the solubility and transport behavior of the precursor in the liquid- based synthesis which will control the reactivity, shape, size and phases of the final samples. When comparing with the hydrothermal method more solvents with special physicochemical properties can be chosen and the reaction temperature can be elevated to much higher values. A recent review by Honma and Devaraju listed the main advantages of hydrothermal and solvothermal processes such as fast reaction kinetics, short processing times, phase purity, high crystallinity, low cost and so on [66].

1.6 Characterization of Nanoparticles

1.6.1 Electron microscopy

These instruments use the beam of highly energetic electrons to examine very small objects which may give information on the morphology, topography and crystallography. The transmission electron microscopy was the first type of electron microscopy to be developed. Scanning electron microscopy (SEM) followed the TEM invention.

1.6.1.1 Transmission electron microscopy (TEM)

Transmission electron microscopy (TEM) was the first type of electron microscopy to be developed. The magnifications of 400 000 times can be easily obtained for many materials where atoms are imaged at magnification greater than million times. This electron microscopy works like a slide projector which shines a beam of light through a slide and as the light passes through it, is subjected to changes by the structures and objects on the slide. The light beam is transmitted through certain parts of the slide which is then projected onto the viewing screen forming an enlarged image of the slide. In this technique, the light source is replaced by an electron source, optical lenses by magnetic electron lenses and a detector is a photophorescence screen or an electron multiplier [67]. This instrument works in the same way except that it is shining a beam of electrons (like the light) through the specimen (like the slide) where the part transmitted is projected onto a phosphor screen for the user to see. The electrons involved have a wavelength of 0.0038 nm and possess an accelerating voltage of 100 kV. This is 10^5 smaller the wavelength of visible light and the resolution is expected to be quite high. The samples for TEM measurements must be prepared to thicknesses that will allow electrons to be transmitted through the sample and sampling is the key to a good TEM picture. The components of the TEM are outlined in Fig. 1.5.

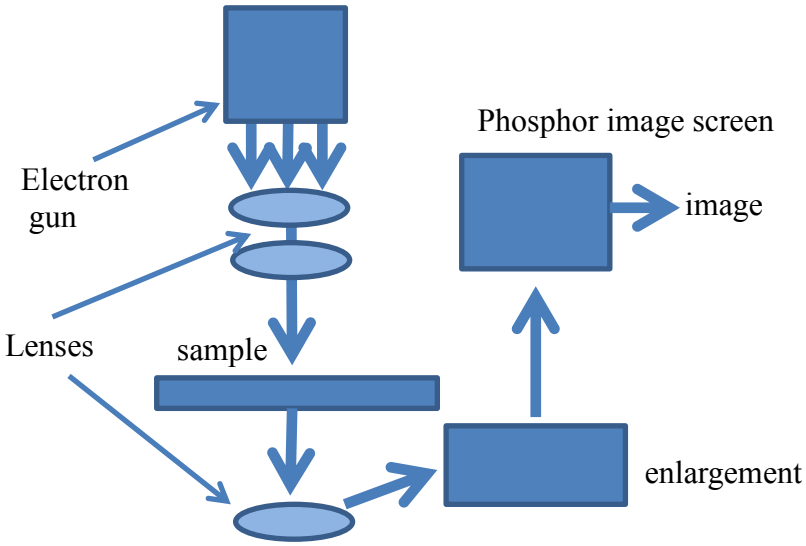

Fig. 1.5 Highly simplified view of the structure of the transmission electron microscope [67].

The images obtained using this technique are two-dimensional sections of the material under study and applications which require three dimensional reconstructions can be accommodated since the energy of the electrons in the TEM determine the relative degree of penetration of electrons in a specific sample.

1.6.1.2 Scanning electron microscopy (SEM)

This instrument was first developed in 1942 and released commercially around 1965 and the later development compared with TEM was due to the electronics involved in 'scanning' the beam of electrons across the sample. The development of SEM began in 1935 by Max Knoll at the Technical University in Berlin where he used an electron beam to scan specimens in a modified cathode-ray tube with conventional lenses where at high magnification rate the instrument could not see samples due to the problem of the width of electron beam. The electrostatic lenses were used by Zworykin, Hiller and Snyder to produce a narrow electron

beam of 50 nm. An SEM was successfully made by Oatley and Smith by using electromagnetic lenses with an electron beam less than 20 nm.

An SEM technique produces images of greater clarity and three-dimensional quality which requires less sample preparation that is why it has become more popular than TEM. There are more images being magnified in focus which makes SEM having a large depth of the field as compared to TEM which produces images of greater magnification. SEM has an extremely wide range of magnification producing images in the range of 10 to 100 000 times their normal size which are sharp, 3-D view of a specimen and is very useful for analyzing the shape and structure of the materials. The voltage is then applied to a cathode-ray tube and converted to an image [68].

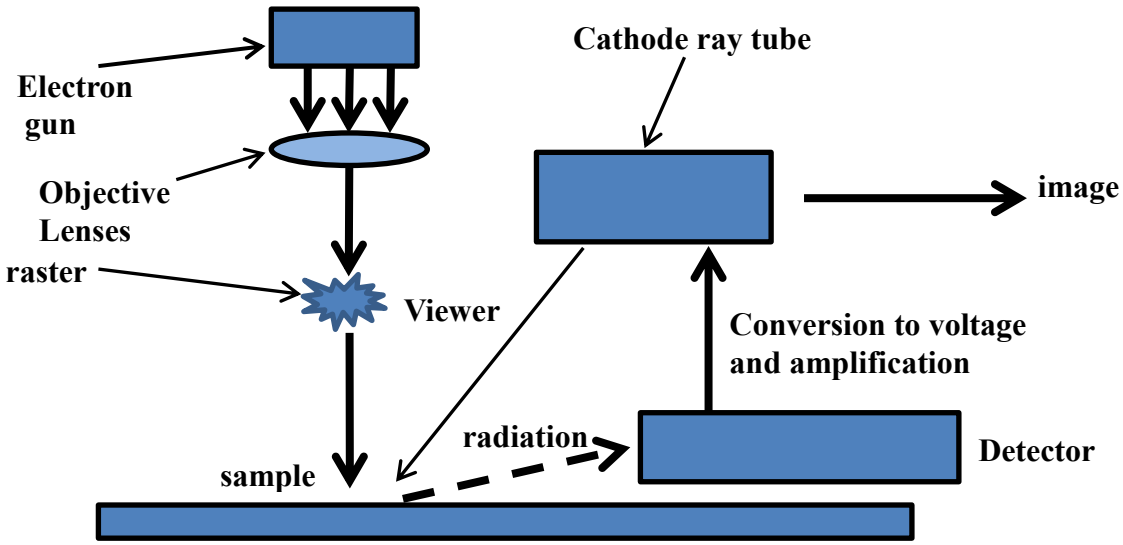

Fig. 1.6 Highly simplified view of a scanning electron microscope [69].

The processes as shown in Fig. 1.6 SEM are in this order, firstly an electron gun emits a beam of electrons which passes through a condenser lens and is refined into a thin stream. The objective lens then focuses the electron beam onto the specimen. The electrons are redirected to scan the specimen in a controlled pattern called a raster. Once the electrons have hit the specimen, a series of interactions deflect secondary particles to detector and then convert the signal to voltage and amplifies it. The voltage is then applied to a cathode-ray tube and converted to an image.

1.6.2 X-ray diffraction (XRD)

The X-ray diffractormeter is applied experimentally to crystal structures of solids in order to identify lattice constants, geometry, orientation of single crystals [69]. The processes in the XRD begin with incidentation of a collimated beam of X-rays with a wavelength ranging from 0.7 to 2 Å into a specimen which is diffracted by the crystalline phases in the specimen according to Bragg's law:

$$\lambda = 2d \sin \theta$$

Here, λ is the X-ray wavelength and d is the spacing between atomic phases in the crystalline phase. The intensity of the X-ray is measured as a function of the diffraction angle 2θ and the sample orientation which is used to identify the crystalline phases and structural properties of the sample. An XRD cannot be destructed, which means there is no need to repeat sample preparations which is why it is widely used in the characterization of the samples. The diffraction peaks can be detected which are used to characterize the perfect and imperfect strains. One can calculate the *d*-spacing caused by change of lattice constants under a homogenous or uniform elastic strain shifts in the diffraction peaks. The broadening of the diffraction peaks is caused by

the finite size of crystallites which is independent of sin θ and the variation of inhomogenous strains from crystallite to crystallite which increase with sin θ.

The particle size can be derived when there is no inhomogeneous strain from the peak width with the scherrer's formular [70]:

$$D = K\lambda/B \cos\theta_B$$

B is the full width at half maximum (FWHM), θ_B is the diffraction angle and K is the scherrer's constant of the order of unity for usual crystal. The nanoparticles often form twinned structure which may produce results different from true particles sizes and usually use a sizable amount of particles which makes it useful for analyzing very small particles or in the form of nanoparticles including thin films [71]. The difference between the calculated particles sizes from XRD and another technique such as TEM is due to a certain number of particles. The XRD gives an average grain size over the entire sample while TEM can view a small fraction of the particles. The nature of the working function of the instrument and nature of solvent which may lead to agglomeration may have an effect especially in the electron microscopy.

1.6.3 Infrared spectroscopy

The balls connected by a string are a typical example of molecules and crystals where atoms or ions are joined by chemical bonds [72]. They can be vibrated with frequencies determined by the atomic weight and the bond strength. The mechanical molecular and crystal vibrations are in the infrared (IR) region of the electromagnetic spectrum at very high frequencies ranging from 10^{12} to 10^{14} Hz (3-300 μm wavelength). There oscillations due to certain vibrational frequencies which provide matter to couple with an impinging beam of infrared electromagnetic radiation

and exchange energy with it when the frequencies are in resonance. There is a certain type of bond and the group of atoms involved in the vibration where absorption frequencies represent excitations of vibration of the specific chemical bond. The intensity of a beam of infrared radiation is measured before and after it interacts with the sample as a function of light frequency. The infrared spectrum is a plot of relative intensity versus frequency. The fourier transform infrared spectroscopy (FT-IR) determines the functional groups present in the sample prepared.

1.6.4 Optical Spectroscopy

This technique is applied to characterize the nanoparticles and is categorized into absorption and emission spectroscopy [73]. These methods show the electronic structures of atoms, ions, molecules or crystals through exciting electrons from the ground to excited states referred as absorption and relaxation from the excited to ground state called emission. There are sharp lines in their spectra to identify isolated atoms or ions due to transition between quantum levels with corresponding wavelengths or photon energies. The position of molecular spectra which are less sharp than atomic spectra with sufficient accuracy can be used to verify the electronic structure of the molecules. The optical spectra of the solids are broad because of the large degeneracy of the atomic levels which is split by interactions into quasi-continuous bands (valence and conduction band). The fundamental gap is the energy difference between the highest lying band (the highest occupied molecular orbital, HOMO) and the lowest lying (the lowest unoccupied molecular orbital, LUMO) bands.

1.6.4.1 Absorption spectroscopy

The optical absorption spectroscopy is used to analyze bulk solids and their corresponding nanoparticles as the small penetration depth of electromagnetic radiation on the order of 50 nm through most of the optical spectrum (visible light) limit them. Different materials absorbs at certain wavelengths depending on the nature of the material under study. The absorption spectrum will show a number of bands corresponding to specific groups within the material in question. There are many compounds that absorb the ultraviolet or visible light where the absorbance of the solution increases as the attenuation of the beam increases. The absorbance is directly proportional to the path length (b) and the concentration (c) as stated by Beer's law shown below.

$$A = \varepsilon\, b\, c$$

Where, ε is the constant proportionality called the absorptivity.

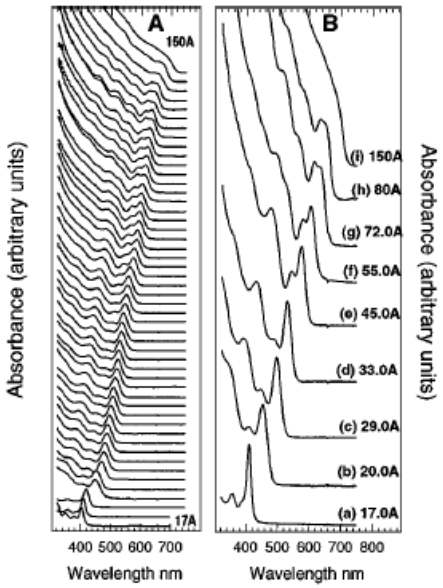

Fig.1.7 Optical absorption spectra of CdSe nanocrystals with varying diameters [74].

This is seen spectroscopically as a blue shift in the absorption edge and a large separation between electronic transitions for a homogeneous size series of CdSe nanocrystal dispersion, collected at room temperature (Fig. 1.7). Observation of discrete electronic transitions in optical absorption [74]. There are extremely sharp characteristic lines in the absorption and emission spectra of nearly isolated atoms and ions due to transitions between quantum levels. Their wavelengths or photon energies can be determined with great accuracy. These lines are for a particular atom or ion and can be used for identification purpose. Even the molecular spectra which are relatively less sharp than atomic spectra, they are sharp as well. For solids, the large degeneracy of the atomic levels is split by interactions into quasi-continuos bands (valence and conduction bands) and makes their optical spectra rather broader. For most of the optical spectrum, the penetration depths of electromagnetic radiation are on the order of 50 nm. This small penetration limits the applications of optical absorption spectroscopy for the characterization of the bulk solids. This technique is readily applicable for the characterization of nanostructures and nanomaterials. Fig 1.7 show optical absorption spectra of CdSe nanocrystals with varying diameters and reveals the increased band gap as indicated by a blueshift in the absorption edge and discrete electronic transition as nanocrystal gets smaller [74].

1.6.4.2 Photoluminescence spectroscopy

The process of emission of light by a material through which can result from variety of stimulations. The emitted luminescence is collected by a lense and goes through an optical spectrometer onto a photon detector. This allows small quantities and low concentration of materials to be analyzed. There are defects in materials in the bulk scale that can make luminesce to be ineffective by quenching the emission of the recombination of charge carries. This can be

observed by a broad band in the photoluminesce spectrum which is not at the specific wavelength. These charge carriers give emission at different wavelengths which are due to the deep and shallow traps that are possible in bulk and nanomaterials that are not well stabilized by an optimum capping ligand (see Fig. 1.3).

1.6.4.3 Energy Dispersive X-ray Spectroscopy (EDS)

The composition of a certain material can be obtained by measuring the energies of the X-rays emitted by that material [75]. The X-rays will be characteristic of an unknown element because each atom in the periodic table has a special electronic structure with a certain set of energy levels. This technique use the emission of photons (X-rays) on the unique energy levels or electron ejected from the atoms studied. The process occur when an incident electron or photon like X-ray or γ-ray strikes an unexcited atom then an electron from an inner shell is ejected and leaves a hole or electron vacancy in the inner shell. In the EDS, the excess energy is released through emission of an X-ray where an electron from an outer shell fills the hole by lowering its energy. The X-rays where incident photons are used for excitation are known as fluorescent X-rays.

1.7 Applications

There are many applications of nanoparticles in a variety of fields. These are too numerous to discuss in great detail. The next section will discuss applications that pertain mainly to bismuth, antimony and tin nanomaterials which are the main focus of this thesis.

1.7.1 Solar cells

There is necessity for other sources of energy in addition to the power station source. This motivated scientists to use solar power as source of energy which is safe and secure to a certain limit. The silicon-based solar cells are expensive which limit their application. The organic and polymer-based photovoltaic cells were studied to overcome this drawback. However, their narrow absorption ranges in addition to poor thermal and environmental stability causes problems. The nanoparticles share wider absorption of the solar spectrum and superior transport properties [76]. The semiconductor nanoparticles can be incorporated as photoabsorbant materials into solar cells. This may reduce the production cost of these devices as nanoparticles can be readily synthesized on a large scale and by solution methods [77]. They require sufficient thickness for the absorption of all incident light. The problem is that film thickness increment increases the probability of carrier trapping at defect and recombination sites [78]. The lead chalcogenide were the first semiconductor nanoparticles investigated and in detail as photovoltaic cell materials. Lead chalcogenides are toxic which open possibilities to use other nanomateials. The tin chalcogenide are less toxic and have similar properties as lead chalcogenides [77]. This makes them attractive as photoabsorbant materials in nanocrystal based solar cells.

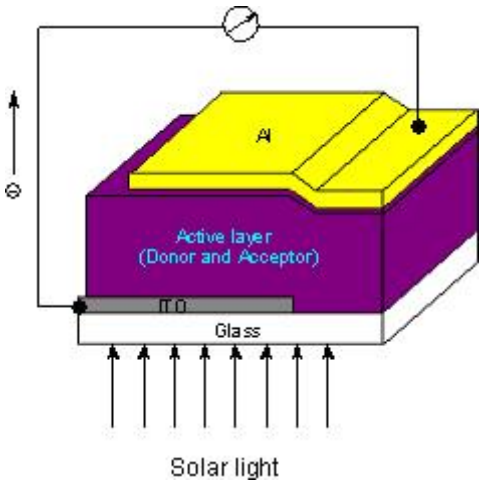

Fig.1.8 The schematic structure of an organic/polymer bulk heterojunction photovoltaic device [79].

A bulk heterojunction hybrid solar cell device with active layer based on B_2S_3 and P3HT such as ITO/B_2S_3:P3HT/Au like the one above in Fig.1.8 was shown by Li *et al*. [80]. In figure 1.8, instead of using organic material, inorganic material such as B_2S_3 can be used. Au acted as an anode instead of Al, ITO as a cathode and the active area of the individual solar device was about 0.15 cm^2. There were current-voltage (I-V) results that indicated that active layers are a new kind of p-n type promising material with good performance in photoelectric applications. A solar-to-electric energy conversion efficiency of 0.0054% was attained with the system.

1.7.2 Lithium-ion batteries

Lithium (Li)-ion batteries which are rechargeable and recyclable are an important source of energy. These batteries have high energy density, light weight and long life cycle which make them applicable in portable electronic products, electric vehicle (EV) and hybrid electrical vehicle (HEV) **[**81]. Graphite is the mostly used material as a composite for commercial Li-ion battery anodes. However, the low capacity of this material approximately 372 mA h g^{-1}, is one of

the limiting factors. The materials such as Si, Sn, Sb and Bi are able to store Li and display Li storage capacities much higher than that of graphite. Sn is the mostly used material in Li-ion batteries due to its high capacity (994 mA h g^{-1}). The only problem with Sn anode is the cycle life Sn exhibits significant volume changes (>300%) which occur during the charge and discharge cycling of Li ions. This causes cracking and crumbling of the electrode material and the subsequent loss of electrical contact between the single particles which result in severe capacity decay. The nanoparticles of Sn have been used to obtain partial improvement by reducing the absolute volume change and degradation in charge of the batteries. The capping agent play a pivotal role in controlling the particle size and improves capacity retention when is in excess. The Sn nanoparticles are usually dispersed in the graphite composite, when combined form an anode electrode or a working electrode. But graphite can be used alone as an anode. When the nanoparticles are oxidized in air, the Sn oxide formed on the surface is either SnO or SnO_2 which can be used for Li storage. Electrochemical lithium insertion is carried with voltammetry or galvanostatic methods which stores Li on the anode. The charge and discharge can be cycled with time which has a specific number depending on the capacity of the anode or negative electrode. The capacity is maintained by the extra reactions such as reduction of surface oxidized Sn and the structural rearrangement of these nanoparticles **[**82**]**.

1.7.3 Inkjet printing

The modeling methods such as conventional vacuum deposition and photolithographic are used in the printing industries. The drawback is their multiple steps, high processing temperature, toxic waste and they are expensive. An alternative is an inkjet printing method which is fast, simple and inexpensive. The materials applied for conductive inkjet printing are metal

nanoparticles, carbon nanotube (CNT), polymers and organo-metallic compounds. Metal nanoparticles have high conductivity (10 000-100 000 S cm^{-1}) compared to polymers (100-1000 S cm^{-1}) and CNTs (10-100 S cm^{-1}). The use of organo-metallic compounds requires additional heat treatment for reduction to metallic species and the conductive films fabricated by this method also contain relatively large amounts of organic residues which may adversely affect the conductivity. Printing using polymer deposition is widely used for the fabrication of organic thin-film transistors (OTFTs), light-emitting diodes (LED) and organic solar cells with the low temperature processing which allows for printing on a flexible substrate at low cost. CNT were studied for flexible integrated circuits. The most promising candidates for conductive inkjet printing are metal nanoparticles. Noble metals such as Au (T_m= 1064 ^oC) and Ag (T_m= 961 ^oC) are applicable to conductive inkjet printing because of their high conductivity and thermal stability. These materials are expensive and have high sintering temperatures which hinder their use due to energy consumption, substrate warpage and thermal stress problems. Other metals can be used as alternatives with low melting temperatures and are cheaper than noble metals. However, the most successful metals for inkjet printing are Sn nanoparticles. The first attempt for inkjet printing is by using conductive ink with Sn nanoparticles. Sn is used due to its low cost and low resistivity which provides a convenient way to fabricate electrical metal lines in various electronic fields. The requirements for the application of metal nanoparticles in inkjet printing are large amount of uniformly sized particles which prevent sintering and fabrication of metal lines at a certain temperature **[**83**]**. Metals with high resistivity are most favourable for this application. In addition, surface tension and viscocity are important factors for inkjet printing because large particles or the aggregation of nanoparticles tend to clog the nozzle of the printer.

1.7.4 Thermoelectric devices

Thermoelectric devices have the potential for revolutionizing energy conversion applications by increasing their performance characteristics. These devices directly convert electrical energy into thermal energy without moving parts or refrigerants. They are capable of converting an existing temperature difference into electricity. This technology is commonly employed for the cooling microchips, diode laser, IR detectors and other microelectronics. The widespread application of thermoelectric devices is hampered by their relative poor performance characteristics which are measured by the dimensionless figure of merit. The corresponding is shown in eqn. 1.4.

$$ZT = \sigma S T/k$$

ZT is the dimensionless figure of merit, σ is the electrical conductivity, S is the Seebeck coefficient, T is the absolute temperature and k is the thermal conductivity.

Nanoparticles have high thermoelectric efficiency due to high Seebeck coefficient, high electrical conductivity and low thermal conductivity. The increase of the Seebeck coefficient in nanoparticles is due to altered electronic density of states compared to bulk material. The lowering of the lattice contributes to the low thermal conductivity due to selective phonon scattering and phonon confinement. The quantum confinement effect affects the electronic and thermal properties of these materials [84]. Materials such as Bi and Sb are applicable in thermoelectronics due to low effective mass, highly anisotropic Fermi surface and their potential to induce a semimetal-to-semiconductor transition in nanoscale [85]. The literature show an increase in the dimensionless figure of merit as the dimensionality and characteristic size of a material are decrease [86].

This device is explained as a solid-state energy converter that transforms heat directly into electricity. There is an n-type and p-type semiconducting materials (Fig.1.9). The temperature difference can be applied across the ends of an n-/p-couple, the working fluid of electrons and holes diffuses, creating an electric field and establishing an electrochemical potential. The potential can drive a current in an external circuit and thus perform useful electric work. The thermoelectric power generation may occur over a range of temperature regimes, depending on the nature of the heat source. This can also occur in reverse order by applying a voltage to create a temperature difference through the Peltier effect [87].

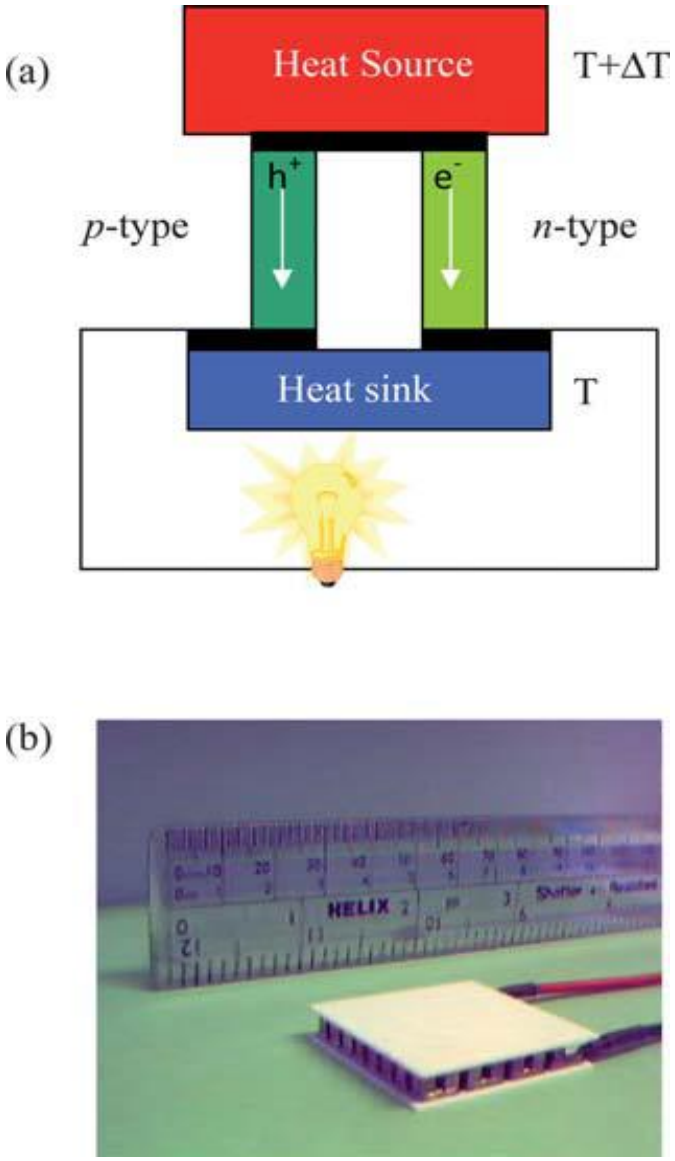

Fig. 1.9 (a) Schematic representation of a thermoelectric couple, composed of two semiconducting materials; one *p*-type and other *n*-type. They are joined at the top by a metal (black bar), to make a junction. When the junction is heated, both types of carriers conduct heat towards the base and power is generated. (b) A commercial thermoelectric module, which contains a number of thermoelectric couples connected electrically in series and thermally in parallel.

1.7.5 Glass encapsulation

Metal nanoparticles containing glasses exhibit an ultrafast electron response within a few of picoseconds. They have large third-order optical nonlinearities due to the large local-field enhancement factor and the strong resonant absorption of the surface plasmon. They are applicable in ultrafast all-optical switching, ultrafast imaging, optical telecommunication, and signal processing. The melt quenching, sol-gel, sputtering, ion exchange, ion implantation and femtosecond laser irradiation make these nanostructures. Au, Ag and Cu doped glasses were mostly investigated with little attention given to other metals.

Bi nanoparticles were precipitated inside glass by using a strong reducing agent (metallic Al) to reduce Bi ions to atomic state. Then atomic or molecular Bi gathers together, grows and forms the nanocrystal during the subsequent heat treatment. This is often observed in the formation process of noble-metal nanoparticles. The reducing agent Al can reduce Bi ions to the lower valence state Bi ions as follows.

$$Bi^{5+} \rightarrow Bi^{3+} \rightarrow Bi^{2+} \rightarrow Bi^{+} \rightarrow Bi^{0} \rightarrow nBi$$

Low valence state Bi is responsible for the generation of NIR luminescence [88].

The use of glasses as encapsulating hosts for plasmonic metal nanoparticles (fabrication of matallo-dielectric nanocomposites) provides a prospect to create a variety of nanoscale devices with attractive properties due to amalgamation of the properties of the glass host and nanometal. The glass present some superior inherent advantage over other dielectrics, such as high

transparency, higher homogeneity than that of other sintered materials, mechanical strength, ease of fabrication in desirable size and shape, ability to withstand high intensity radiation, and avoiding air oxidation of metal nanocomposite. This make glasses excellent encapsulating hosts for metal nanoparticles for practical application.

An example for these is bismuth glass which is one of the most important amongst the heavy metal oxide (HMO) glasses due to their several inherent properties such as high refractive index, wide transmission window, and broad band near infrared (NIR) luminescence. The photoluminescence properties make them applicable in photonic and optoelectronic. The various oxidation states such as Bi^{5+}, Bi^{3+}, Bi^{2+}, Bi^{+}, and Bi^{0} coexist. The emission centers due to these are controversial issue.

The drawback for bismuth transparent glasses is the greying or blackening when melted above 1000 ^{0}C. The intensity of darkening increases with increase in melting temperature as well as Bi_2O_3 content. This is because of auto-thermo reduction of Bi^{3+} ions to Bi^{0} during the course of melting process. The reduction of Bi_2O_3 occurs through the following thermal decomposition reaction.

$2Bi_2O_3 \leftrightarrow 4Bi^{0} + 3O_2 \uparrow$

The metallic Bi^{0} is formed with release of oxygen.

The valence state of bismuth exists in its glasses and corresponding crystalline compounds. There are various emission centers due to different ionic species. The formation of various

valence states take place by the auto-thermo reduction of Bi^{3+} ions (origin is raw material, Bi_2O_3) proceeds towards Bi^0 reversibly during melting process and forming the following intermediate valence states:

$$Bi^{3+} \leftrightarrow Bi^{2+} \leftrightarrow Bi^{+} \leftrightarrow Bi^{0}$$

There is no clarity to which valency of the bismuth ion contribute to the various emissions.

1.8 Scope of the work

There are some drawbacks to the reported synthetic methods to bismuth and tin chalcogenide nanoparticles which indicates that there is still a need to improve the methods of preparation of these nanoparticles. Most of these methods for bismuth chalcogenides generally require rigorous experimental conditions, long reaction time, or intricate instruments, which make production in large scale difficult [79-94]. And most of the methods for tin chalcogenides are quite expensive and employ highly toxic materials which create a number of technological and environmental problems [95-103]. There are few investigations on the synthesis of antimony semimetal and metal chalcogenide nanoparticles, therefore new ideas about the synthetic methods are desirable [104-114]. This research work will cover the synthesis of bismuth, antimony semimetals, tin metal and metal chalcogenide nanoparticles of bismuth, antimony and tin using a facile hybrid solution based and thermolysis method. The route is simple, non-organometallic, cost effective, low temperature and relatively environmentally benign. In addition, organically capped ZnTe nanoparticles and water soluble CdTe nanoparticles were also synthesized by this route. The effect of various experimental variables, including the capping ligand, pH, reaction time and cadmium source on the particle growth, optical properties and morphology were systematically

investigated. Several groups have systematically explored the influence of various synthetic variables (including pH value, precursor concentration, ligand:Cd ratio, and Te:Cd ratio) on the growth of CdTe nanoparticles [115-117]. These were found to have effect on the structural and optical properties of the nanoparticles.

This method has been successfully used by the Revaprasadu group for the synthesis of various metal chalcogenides nanoparticles such as CdSe, CdTe and PbTe [58-61]. The cadmium and lead salts were chosen as metal sources for the synthesis of CdSe, PbTe and CdTe nanoparticles. These metal precursors were environmental friendly, less reactive and relatively inexpensive

In this work, the synthesis of semimetal nanoparticles and/or metal nanoparticles (Bi Sb and Sn) involves two steps:

(1) Reduction of metal salt and

(2) Thermolysis at high temperature.

While the synthesis of metal chalcogenide nanoparticles involve three steps;

(1) Involves the reduction of the chalcogenide source (S, Se, Te) from 0 to -2 oxidation state using sodium borohydride as a reducing agent.

(2) This is followed by addition of the metal source (usually metal chloride) to chalcogenide ion.

(3) The particles are capped by the ligand at high temperatures resulting in the formation of metal chalcogenide nanoparticles.

1.9 Aims and objectives of the research

1.9.1 Aim

The aim of this study is to synthesize metal and metal chalcogenide nanoparticles using a facile hybrid solution based and thermolysis method.

1.9.2 Objectives

- To synthesize and characterize semimetal and metal chalcogenide nanoparticles capped by organic and water soluble ligands.
- To investigate the effect of capping ligand on the morphology of the semimetal and metal chalcogenide nanoparticles.
- To determine the effect of metal source on the morphology of the nanoparticles.
- To investigate the effect of temperature on the size of the nanoparticles.
- To determine a possible growth mechanism responsible for the formation of the nanoparticles.

1.10 References

[1] M. Faraday, The Bakerian lecture: Experimental relations of gold (and other metals) to light, Philosophical Transactions of the Royal Society of London, **147** (1847) 145-181, 159.

[2] M. Faraday, The Bakerian lecture: experimental relations of gold (and other metals) to light, Philosophical Transactions of the Royal Society of London, **147** (1847) 145-181, 146.

[3] R. P. Feynman, (1960) A lecture in engineering science. In California Institute of Technology February edn.

[4] K. E. Drexler, Engines of Creation (1990). London, Fourth Estate, 1st edn. 296.

[5] http://en.wikipedia.org/wiki/Nanoparticle, modified 29-04-2011.

[6] A. Henglein, *Chem. Rev*., **89** (1989) 1861.

[7] Z. A. Peng, X. Peng, *J. Am. Chem. Soc*., **124** (2002) 3343.

[8] M. A. Malik, P. O'Brien, N. Revaprasadu, **180** (2005) 689.

[9] V. I. Klimov, *Los Alamos Science*., **28** (2003) 214.

[10] J. Gao, B. Xu, *Nano Today*, **4** (2009) 37.

[11] M. Allsopp, A. Walters, D. Santillo, *Greenpeace Research Laboratories Technical Note* **10 (**2007) 22 pp.

[12] S. Z. Qiao, J. Liu, G. Q. Lu, Synthetic Chemistry of Nanomaterials, *Modern Inorganic Synthetic Chemistry,* Amsterdam: Elsevier, 479.

[13] G. Cao, Nanostructures and nanomaterials, Imperial College Press, (2004) 367.

[14] H. -G. Rubahn, Basics of Nanotechnology, Wiley VCH, 12.

[15] M. L. Steigerwald, L. E. Brus, *Acc. Chem. Res*. **23** (1990) 183.

[16] M. G. Bawendi, M. L. Steigerwald, L. E. Brus, *Annu. Rev. Phys.*

Chem. **41**, 1990, 477.

[17] H. Weller, *Angew. Chem., Int. Ed. Engl*. **32** (1993) 41.

[18] H. Weller, *Adv. Mater*. **5** (1993) 88.

[19] A. Hagfeldt, M. Graetzel, *Chem. Rev*. **95** (1995) 49.

[20] J. H. Fendler, F. C. Meldrum, *Adv. Mater*. **7** (1995) 607.

[21] A. P. Alivisatos, *J. Phys. Chem*. **100** (1996) 13226.

[22] H. Haug, S. W. Koch, Quantum theory of the optical and electronic properties of semiconductors; World Scientific Publishing Co. Pte. Ltd.: London, (1990) 333.

[23] L. E. Brus, *J. Chem. Phys*. **79** (1983) 5566.

[24] L. E. Brus, *J. Chem. Phys*. **80** (1984) 4403.

[25] L. Brus, *J. Phys. Chem.* **90** (1986) 2555.

[26] C. F. Landes, S. Link, M. B. Mohamed, B. Nikoobakht, A. El-Sayed, *Pure. Appl. Chem.* **74**(9) (2002) 1675.

[27] M. L. Steigerwald , L. E. Brus. *Acc. Chem. Res,* **23** (1990) 183.

[28] E. A. Olson, M. Yu, E. M. Zhang, Z. Zhang, L. H. Allen, *J. Appl. Phys*. **97** (2005) 034304.

[29] R. Fu, S. Xu, Y. Lu, J. Zhu, *Crystal Growth Design*., **5** (2005) 1379.

[30] G. Cao, Nanostructures and nanomaterials, Imperial College Press, (2004) 371.

[31] Z. Zhang, X. Sun, M. S. Dresslhaus, J. Y. Ying, *Phys. Rev. B* **61** (2000) 4850.

[32] S. H. Choi, K. L. Wang, M. S. Leung, G. W. Stupian, N. Presser, B. A. Morgan, R. E. Robertson, M. Abraham, S. W. Chung, J. R. Heath, S. L. Cho, J. B. Ketterson, *J. Vac. Sci. Technol. A* **18** (2000) 1326.

[33] Y. Cui, C. M. Lieber, *Science* **291** (2001) 851.

[34] Y. Wang, X. Duan, Y. Cui, C. M. Lieber, *Nano Lett*. **2** (2002) 101.

[35] S. W. Chung, J. Y. Yu, J. R. Heath, *Appl. Phys. Lett*. **76** (2000) 2068.

[36] R. Kelsall, I. Hamley, M. Geoghegan (2005), Nanoscale science and technology, Wiley, Pg 26-27.

[37] D. Pan, Q. Wang, S. Jiang, X. Ji, L. An, *J. Phys. Chem. C* **111** (2007) 5661.

[38] R. A. Montes, The bacterial toxicity of selenocyanate and the incorporation of tellurium and selenium in bacterial cells and the synthesis and biosynthesis of cadmium telluride nanoparticles and their elemental quantification via ICP-AES. (2012). Sam Houston State University, Thesis.

[39] T. Jonson, V. K. La Mer. *J. Am. Chem. Soc*., **69** (1947) 1184.

[40] W. Z. Ostwald, *Phys. Chem*., **22** (1897) 289.

[41] W. Z. Ostwald, *Phys. Chem*., **34** (1900) 495.

[42] R. Rossetti, J. L Ellison, J. M. Gibson, L. E. Brus, *J. Chem. Phys*., **80** (1984) 4464.

[43] H. Weller, *Adv. Mater*., **5** (1993) 88.

[44] M. L. Hassan, A. F. Ali, *J. Cryst. Growth*., **310** (2008) 5252.

[45] S. O. Oluwafemi, N. Revaprasadu and A. Ramirez, *J. Cryst. Growth*., **310** (2008) 3230.

[46] V. S. R. Rajasekhar Pullabhotla, N. Revaprasadu, *Mater. Lett*., **63** (2009) 2097.

[47] N. Mntungwa, Rajasekhar V. S. R. Pullabhotla, N. Revaprasadu, *Colloid. Surfaces B.* **101** (2013) 450.

[48] Z. B. Shang, Y. Wang, W. J. Jin, *Talanta*., **78** (2009) 364.

[49] C. B. Murray, D. J. Norris, M. G. Bawendi, *J. Am. Chem. Soc*., **115** (1993) 8706.

[50] T. Trindade, P. O'Brien, *Adv. Mater*., **8** (1996) 161.

[51] T. Trindade, P. O'Brien. *Chem. Mater*., **9** (1997) 523.

[52] B. Geng, X. Liu, Q. Du, J. Ma, X. Liu, *Mater. Res. Bull*., **43** (2008) 1093.

[53] T. Mthethwa, V. S. R. Rajasekhar Pullabhotla, P. S. Mdluli, J. Wesley-Smith, N. Revaprasadu, *Polyhedron*, **28** (2009) 2977.

[54] L. D. Nyamen, V. S. R. Pullabhotla, A. A. Nejo, P. Ndifon, N. Revaprasadu, *New J. Chem*., **35** (2011) 1133.

[55] Z. A. Peng, X. Peng, *J. Am. Chem. Soc*., **123**, (2001) 183.

[56] L. Qu, Z. A. Peng and X. Peng, *Nano. Lett*., **1** (2001) 333.

[57] U. K. Gautam, M. Natha, C. N. R. Rao, *J. Mater. Chem*., **13** (2003) 2845.

[58] N. N. Maseko, N. Revaprasadu, V. S. R. Rajasekhar Pullabhotla, R. Karthik, P. O'Brien, *Mater. Lett*. **64** (2010) 1037.

[59] N. Ziqubu, K. Ramasamy, V. S. R. Rajasekhar Pullabhotla, N. Revaprasadu, P. O'Brien, *Chem. Mater*. **22** (2010) 3817.

[60] N. Mntungwa, V. S. R. Rajasekhar Pullabhotla, N. Revaprasadu, *Mater. Chem. Phys*., **126** (2011) 500.

[61] K. Ramasamy, A. O. Nejo, N. Ziqubu, V. S. R. Rajasekhar Pullabhotla, A. A. Nejo, N. Revaprasadu, P. O'Brien, *Eur. J. Inorg. Chem*. (2011) 5196.

[62] M. Gao, Y. Xu, J. Jiang, S. Yu, *Chem. Soc. Rev*., **42** (2013) 2986.

[63] J. Wang, Y. Li, *Mater. Chem. Phys*., **87** (2004) 420.

[64] A. Alemi, S. W. Joo, Y. Hanifehpour, A. Khandar, A. Morsali, B. Min, **1155** (2011) 186528.

[65] Z. Zhang, C. Zhou, L. Huang, X. Wang, Y. Qu, Y. Lai, J. Li, Electrochimica. Acta., 114 (2013) 88.

[66] M. K. Devaraju and I. Honma, *Adv. Energy, Mater*., **2** (2012) 284.

[67] M. Wilson, K. Kannangara, G. Smith, M. Simmons, B. Raguse, (2002) Nanotechnology, Pg 34.

[68] H. -G. Rubahn, Basics of nanotechnology, Wiley-VCH, (2004) 63.

[69] M. Wilson, K. Kannangara, G. Smith, M. Simmons, B. Raguse, (2002) Nanotechnology, 58.

[70] M. Wilson, K. Kannangara, G. Smith, M. Simmons, B. Raguse, (2002) Nanotechnology, 32.

[71] G. Cao, Nanostructure and nanomaterials, Imperial College Press, (2004) 331.

[72] L. S. Birks, H. Friedman, *J. Appl. Phys*. **17** (1946) 687.

[73] A. Segmuller, M. Murakami, in Thin Fimls From Free Atoms and Particles, ed. K. J. Klabunde, Academic Press, Orlando, FL, (1985) 325.

[74] G. Cao, Nanostructures and nanomaterials. Imperial College Press, (2003) 347.

[75] G. Cao, Nanostructure and nanomaterials, Imperial College Press, (2004) 345.

[76] C. B. Murray, C. R. Kagan, M. G. Bawendi, *Annu. Rev. Mater. Sci*., **30** (2000) 545.

[77] G. Cao, Nanostructures and nanomaterials, Imperial College Press, (2004) 349.

[78] E. H. Sargent, *Nat. Photonics*, **3** (2009) 325.

[79] P. D. Antunez, J. J. Buckley, R. L. Brutchey, *Nanoscale*. **3** (2011) 2399.

[80] H. D. Jin, C. Chang, *J. Mater. Chem*. **21** (2011) 12218.

[81] J. G. Xue, B. P. Rand, S. Uchida, S. R. Forrest, *J. Appl. Phys*., **98** (2005) 124902-1.

[82] Y. Li, Y. Zhang, Y. Lei, P. Li, H. Jia, H. Hou, Z. Zheng, *Mater. Sci. Eng. B* **177** (2012) 1764.

[83] H. Wang, P. Gao, S. Lu, H. Liu, G. Yang, J. Pinto, X. Jiang, *Electrochimica Acta*, **58** (2011) 441.

[84] C. Nabais, R. Schneider, P. Willmann, D. Billaud, *Energ. Convers Manage*. **56** (2012) 32.

[85] Y. H. Jo, I. Jung, C. S. Choi, I. Kim, H. M. Lee, *Nanotechnology*, **22** (2011) 225701.

[86] M. D. Baltimore, 18th International Conference on Thermoelectrics , IEEE, (1999).

[87] J. Fang, K. L. Stokes, W. L. Zhou, W. Wang, J. Lin, *Chem. Commun*., (2001) 1872.

[88] S. R. Hostler, Y. Q. Qu, M. T. Demko, A. R. Abramson, X. Qiu, C. Burda., *Superlattice. Microstruct*. **43** (2008) 195.

[89] P. Vaqueiro, A. V. Powell, *J. Mater. Chem*., **20** (2010) 9577.

[90] G. Li, D. Tan, F. Luo, D. Chen, Q. Zhao, J. Qiu, *J. Non-Cryst Solid*. **357** (2011) 2312.

[91] H. M. Cui, H. Liu, J. Y. Wang, X. Li, F. Han, R. I. Boughton, *J. Cryst. Growth*., **271** (2004) 456.

[92] D. Wang, D. Yu, M. Mo, X. Liu, Y. Qian, *J. Cryst. Growth*., **253** (2003) 445.

[93] Y. F. Lin, H. W. Chang, S. Y. Lu, C. W. Liu, *J. Phys. Chem. C* **111** (2007) 18538.

[94] Y. Jiang, Y. J. Zhu, *J. Phys. Chem. B* **109** (2005) 4361.

[95] Y. Yu, C. H. Jin, R. H. Wang, Q. Chen, L. M. Peng, *J. Phys. Chem. B* **109** (2005) 18772.

[96] R. Chen, M. H. So, C. M. Che, H. Sun, *J. Mater. Chem*. **15** (2005) 4540.

[97] H. Zhu, D. Yang, H. Zhang, *Mater. Lett*. **60** (2006) 2686.

[98] S. K. Panda, S. Gorai, S. Chaudhuri, *Mater. Sci. Eng. B* **129** (2006) 265.

[99] D. S. Koktysh, J. R. McBride, S. J. Rosenthal, *Nanoscale Res. Lett*. **2** (2007) 144.

[100] Y. Liu, D. Hou, G. Wang, *Chem. Phys. Lett*. **379** (2003) 67.

[101] M. N. Salavati, D. Ghanbari, F. J. Davar, *Alloy. Comp*., **492** (2010) 570.

[102] S. Sohila, M. Rajalakshmi, C. Muthamizhchelvan, S. Kalavathi, C. Ghosh, R. Divakar, C. N. Venkiteswaran, N. G. Muralidharan, A. K. Arora, E. Mohandas, *Mater. Lett*., **65** (2011) 1148.

[103] M. Bicer, I. Sisman, *Appl. Surf. Science*., **257** (2011) 2944.

[104] S. Yogesh, N. Garje, S. S. Garje, *Synthesis and Reactivity in Inorganic, Metal-Organic, and Nano-Metal Chemistry*, **41** (2011) 36.

[105] M. Salavati-Niasari, M. Bazarganipour, F. Davar, A. A. Fazl, *Appl. Surf. Sci*. **257** (2010) 781.

[106] H, Hu, B. Yang, Q. Li, X. Liu, W. Yu, Y. Qian, *J. Cryst. Growth*. **261** (2004) 485.

[107] P. Balaz a, L. Takacs, E. Godocıkova. I. Skorvanek, J. Kovac, W. S. Choi, *Journal of Alloys and Compounds* **434–435** (2007) 773.

[108] M.T. Cuberesa, B. Stegemannb, B. Kaiserb, K. Rademannb, *Ultramicroscopy* **107** (2007) 1053–1060

[109] A. Houdayer, R. Schneider, D. Billaud, J. Lambert, J. Ghanbaja, *Mater. Chem. Phys*. **101** (2007) 404.

[110] A. Houdayer, R. Schneider, D. Billaud, J. Lambert, J. Ghanbaja, *Mater. Lett*. **61** (2007) 171.

[111] B. Yang, Y. Wu, H. Hu, C. Li, X. Yang, Y. Qian, Mater. Chem. Phys., **92** (2005) 286.

[112] A. Houdayer, R. Schneider, D. Billard, J. lambert, J. Ghanbaja, *Mater. Chem. Phys*. **101** (2007) 404.

[113] A. Houdayer, R. Schneider, D. Billaud, J. Lambert, J. Ghanbaja, *Mater. Lett*. **61** (2007) 171.

[114] C. Kim, D. H. Kim, Y. S. Han, J. S. Chung, H. Kim, *J. Alloy. Comp*. **509** (2011) 609.

[115] H. Zhang, D. Wang, B. Yang, H. Mohwald, *J. Am. Chem. Soc*., **128** (2006) 10171.

[116] K. Zhao, J. Li, H. Wang, J. Zhuang, W. Wang, *J. Phys. Chem. C*., **111** (2007) 5618.

[117] A. L. Rogach, T. Franzl, T. A. Klar, J. Feldmann, N. Gaponik, V. Lesnyak, A. Shavel, A. Eychmuller, Y. P. Rakovich, J. F. Donegan, *J. Phys. Chem. C*, **111** (2007) 14628.

2.0 Bismuth Nanoparticles

2.1 Introduction

Bismuth (Bi) is a semimetal with a small overlap of valence and conduction band of 38 meV at 5 K [1]. Another example of a group four metal with a small band overlap is antimony (Sb). Both bismuth and antimony are referred to as semimetals. Bi nanoparticle can undergo a transition into a semiconductor when well confined in the nanometer scale, thus allowing the unusual properties of bismuth to be available as a semiconducting material as well as a semimetal [1]. Bi nanoparticles have been reported to contain a similar rhombohedral crystal structure as that of their corresponding bulk material. There have been few instances where cubic Bi which is a high-pressure phase was obtained. This is due to the internal pressure exerted by the nanocrystal surface which increases with decreasing particle size [2,3]. The spherical or dot shaped structures of this material are commonly obtained by controlling the reaction conditions. However a variety of elongated Bi particles have been reported to result from the assembly of smaller particles [4]. These nanoparticles have several potential applications as thermoelectric materials, lubricating addictives, and in magnetoresistance studies [5,6]. Bulk and nanometer sized Bi can easily be oxidized; therefore surface protection is necessary to maintain the purity of this material. Bi oxide may be present as a product under certain reaction conditions; as a result careful interpretation of the results is required after characterizing these nanoparticles [7]. The low melting point of bulk Bi (271 ^{o}C) should be taken into consideration when preparing this material.

Most of the routes use the reducing agent and the bismuth salt for the formation of bismuth particles and a certain capping ligand is always necessary. Bismuth chloride due to its high solubility is commonly used as compared to other semimetal source such as complex compounds, bismuth nitrate, bismuth citrate to mention a few [6,8,9]. There are many other physical and chemical methods which use a top-down approach to manufacture these

nanoparticles [7-11]. Some of these synthetic routes use polymers for protecting particles against oxidation. Yarema *et al*. [6] reported the synthesis of monodispersed hexadecylamine capped Bi nanoparticles using a simple single source method with $Bi[N(SiMe_3)_2]_3$ as the precursor. The size of spherical particles was controlled between 11 and 22 nm by the reaction temperature. Two and three dimensional super-structures were obtained through self-assembly of the dot shaped nanoparticles. Bi nanoparticles have been prepared by the reduction of Bi salt using a high temperature organic method [12]. Tri-n-octylphosphine and oleic acid were used as capping ligands to limit the growth and stabilize the surface of the nanoparticles. The effect of temperature was investigated between 90 to 220 ^{o}C, with the optimum temperature being in 170-180 ^{o}C range. A size-selection precipitation procedure was used to obtain monodispersed nanoparticles. Nanostructured bismuth was also synthesized by the chemical reduction of Bi salt using a reducing agent in inverse micelles [13]. The polymers are added to limit oxidation of the particles and prevent agglomeration. Analysis using powder X-ray diffraction technique shows powders that are highly crystalline of the bulk rhombohedral structure. Their absorption spectra show two peaks at 277 and 282 nm due to the anisotropic morphology of bismuth. These particles were not applicable for creating an electrically conductive film due to poor substrate coverage and particle agglomeration.

In this chapter, Bi nanoparticles were prepared using a solution based high temperature route. The Bi salt is first reduced and dissolved in tri-n-octylphosphine (TOP), followed by thermolysis in capping groups such as tri-n-octylphosphine oxide (TOPO), oleylamine (OA) and hexadecylamine (HDA) at varying temperatures of 190, 230 and 270 ^{o}C, respectively . The synthetic method was further adapted to prepare water soluble triethanolamine (TEA) capped Bi nanoparticles at room temperature and 90^{o}C.

2.2 Experimental

2.2.1 Chemicals

Bismuth acetate [$Bi(C_2H_3O_2)_3$], sodium borohydride ($NaBH_4$), deionized water, methanol, toluene, tri-n-octylphosphine oxide (TOPO), oleylamine (OA), hexadecylamine (HDA), and tri-n-octyl-phosphine (TOP) were purchased from Sigma Aldrich. All chemicals were of analytical grade and used directly as purchased.

2.2.2 Synthesis of TOPO, HDA and OA capped bismuth (Bi) nanoparticles

Bismuth acetate (0.124 g, 0.32 mmol) was mixed with deionized water (20.0 mL) in a three-necked flask at room-temperature. Sodium borohydride (0.031 g, 0.79 mmol) was carefully added to this mixture and the flask was immediately purged with nitrogen gas to create an inert atmosphere. The mixture was stirred for 2 h followed by the addition of excess methanol. The resultant solution was then centrifuged. The black precipitate was dispersed in tri-n-octylphosphine, TOP (6.0 mL) and stirred continuously to form a TOP–Bi solution, which was then injected into 6.0 g of tri-n-octylphosphine oxide (TOPO) at 190 ^{o}C. The temperature was kept constant for 2 h. The reaction was stopped and methanol was added, resulting in the flocculation of the bismuth nanoparticles. The TOPO capped bismuth particles were isolated after centrifugation.

Further experiments were carried out using other capping groups such as oleylamine (OA), and hexadecylamine (HDA). Reactions were also carried out at higher temperatures of 230 ^{o}C and 270 ^{o}C.

2.2.3 Synthesis of TEA capped bismuth nanoparticles

Bismuth acetate (0.124 g, 0.32 mmol) was mixed with deionised water (10.0 mL) in a three-necked flask. 10.0 mL aqueous solution of sodium borohydride (0.031 g, 0.79 mmol) was carefully added to this mixture and the flask was immediately purged with nitrogen gas to create an inert atmosphere. After 2 h, 20.0 mL aqueous triethanolamine solution (0.095 g , 6.40 mmol) with a molar ratio of 1:1 (Bi^{2+}: TEA) were added simultaneously to the black crystals reduced Bi particles in the solution. The pH of the solution was raised to 7 by using HCl (0.10 M) and NH_3 (0.10 M) solutions. After completion of the reaction, excess methanol was added resulting in the reversible flocculation of the nanoparticles. The flocculate was separated from the supernatant by centrifugation. The resultant particles were dissolved in acetone to give a solution of nanocrystallites for characterization. The above reaction procedure was repeated at pH 4 and 11. Further reactions were carried out at 90 ºC.

2.2.4 Characterization of the nanoparticles

2.2.4.1 Optical characterization

A Cary 50 conc. UV-Vis spectrometer was used to carry out optical measurements in the 200-800 nm wavelength range at room temperature. Samples were placed in quartz cuvettes (1 cm path length).

Room-temperature photoluminescence (PL) spectra were recorded on a Perkin Elmer LS 55 luminescence spectrometer with Xenon lamp over 200-800 nm range. The samples were placed in quartz cuvettes (1 cm path length). The excitation wavelenght for all emission was 275 nm. Acetone was used as a solvent for all optical measurements.

2.2.4.2 X-Ray powder diffraction

The crystallinity of the dried colloids was studied by using powder X-ray diffractometer (XRD). Powder diffraction patterns were recorded in the high angle 2θ range of 10-80^{o} using a Bruker AXS D8 Advance X-Ray diffractometer, equipped with nickel filtered Cu Kα radiation (λ = 1.5418 Å) at 40 kV, 40 mA and at room temperature. The scan speed and step sizes were 0.05^{o} min^{-1} and 0.00657 respectively.

2.2.4.3 Transmission electron microscopy (TEM) and High Resolution TEM

Samples were prepared by placing a drop of dilute solution of nanoparticles on Formvar-coated grids (150 mesh) for TEM and holey carbon grids for HRTEM. The samples were allowed to dry completely at room temperature and viewed using a JEOL 1010 TEM and JEOL 2100 HRTEM. Viewing was done at an accelerating voltage of 100 kV (TEM) and 200 kV (HRTEM), and images captured digitally using a Megaview III camera; stored and measured using Soft Imaging Systems iTEM software.

2.2.4.3 Fourier Transform Infrared Spectroscopy

For FT-IR measurements, pure solid samples were dried and ground to fine powder while liquid TEA was measured directly and the spectra were recorded using a Tensor 27, Bruker FT-IR Spectrometer.

2.3 Results and discussion

The synthetic approach involves two steps, first the Bi salt is reduced to the Bi semimetal particles at room temperature followed by thermolysis at high temperatures (190, 230 and 270 ^{o}C). The two reaction are as shown below in two steps:

Step 1 : $Bi(CH_3CO_2)_3 + NaBH_4 + H_2O \rightarrow Bi + 3Na(CH_3CO_2) + Na_2B_2O_{7+}H_2$

Step 2: Bi + TOP + capping agent → capped Bi

The use of bismuth acetate, $Bi(CH_3COO)_3$ and $BiCl_3$ is based on the successful application of bismuth salts for producing Bi nanoparticles [12]. The reduction is made possible by the presence of an active hydride ($NaBH_4$) which activates the solubility of $Bi(CH_3COO)$ and/or $BiCl_3$ in water. This is observed by the gas evolution and vigorous reaction that occurs at the beginning of reduction. TOP is known to coordinate neutral surfaces sites forming a weak bond with metals [13].

2.3.1 TOPO/HDA/OA capped Bismuth nanoparticles

The TEM images of Bi nanoparticles synthesized using TOPO as capping agent at different thermolysis temperatures are shown in Fig 2.1. At 190 ^{o}C, highly monodispersed spherical particles with an average diameter of 7.79 ± 1.35 nm were observed (Fig. 2.1a). The minimum average spacing between the particles is uniform at a distance of approximately 3.3 nm. These findings are characteristic of TOPO, a strongly binding ligand which prevents aggregation, hindering the formation of anisotropic particles [14]. Fig. 2.1b shows a highly crystalline spherical particle d = 11.19 nm with lattice fringe spacing of 0.34 nm corresponding to the [012] plane of rhombohedral Bi. When the temperature was raised to 230 ^{o}C, particles in the form of

branched nanostructures were formed. The particles appear to assemble into rods which also form zig zag and bipodal structures as shown by arrows (Fig.2.1c). The HRTEM image of a single branched rod with length of 228.83 nm and breadth of 31.22 nm is shown in Fig. 2.1d. Lattice fringes are observed (insert Fig. 2.1d) with the lattice spacing of 3.10 Å indexed to the [012] plane of rhombohedral phase of bismuth. The morphology of the Bi nanostructure are similar to the branched nanowires of PbSe and PbS previously reported [15,16]. In these reports an oriented growth mechanism is responsible for the fusion of intermediate shaped particles leading to the formation of branched nanowires.

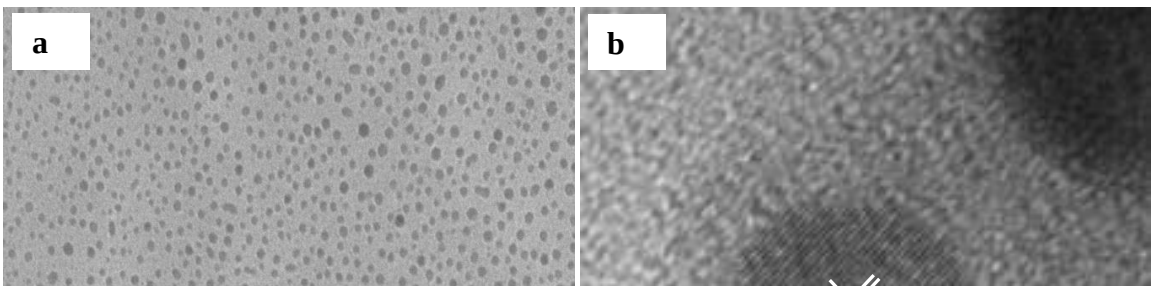

Fig. 2.1 TEM and corresponding HRTEM images on the left and right, respectively, of TOPO capped bismuth nanoparticles synthesized at (a) and (b) 190 ^{o}C, (c) and (d) 230 ^{o}C.

A similar mechanism of growth is possible in our study. The nanorod observed in Fig. 2.1d shows an aggregation of particles. The lattice fringes observed in the HRTEM image (insert Fig. 2.1d) shows discontinuities suggesting that an oriented attachement growth mechanism occurs [17].

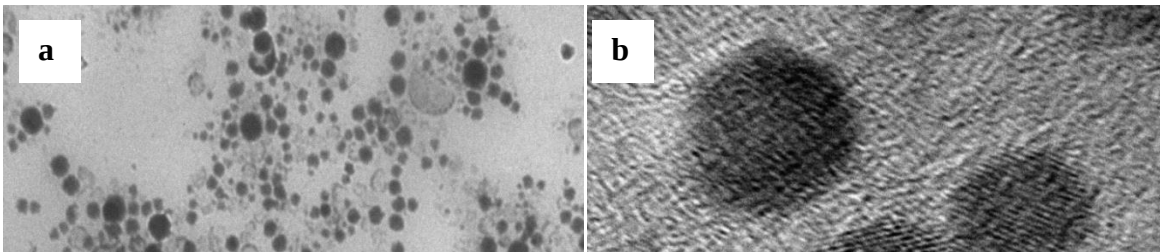

d

Fig. 2.2. TEM and corresponding HRTEM images of OA capped bismuth nanoparticles synthesized at (a) and (b) 190 ^{o}C, (c) and (d) 230 ^{o}C.

The use of OA as a capping group at 190 ^{o}C produced close to spherical Bi particles with an average diameter of 31.75 ± 11.50 nm (Fig. 2.2a). The corresponding HRTEM image (Fig. 2.2b) showed the presence of well defined spherical nanoparticles with distinct lattice fringes of lattice spacing of 3.30 nm, corresponding to the (012) plane of rhombohedral Bismuth plane. When the temperature is increased to 230 ^{o}C a high percentage of cubes and short rod shaped particles are

observed (Fig. 2.2c). OA is a weak binding capping group allowing the formation of anisotropic larger particles. The cubes and rods arranged in a manner which suggests some degree of self assembly forming chains. Ma *et al*. [4] also observed a similar feature for Bi quantum dots that self assemble into nanobelts. They attributed the formation of the nanobelts to the amount of sodium hydroxide added to the reaction, however they could not explain it's exact role. The average particle diameter of the few oblate particles is 20.48 ± 2.54 nm, with distinct lattice fringes observed in the HRTEM image (Fig. 2.2d). These lattice fringes in the HRTEM in Fig 2.2d have the lattice spacing of 3.30 Å assigned to (012) single plane of rhombohedral bismuth.

The self-assembly of particles is also observed to a smaller extent when HDA is used as a capping group at 230 ^{o}C (Fig. 2.3a). There is some assembly of the spherical particles into rods as shown by the arrows. The corresponding HRTEM image (Fig. 2.3b) showing the presence of close to spherical particles. When the temperature is increased to 270 ^{o}C, larger faceted particles are observed (Fig. 2.3c). The particles are reasonably well defined with the cubic morphologies clearly seen in the TEM image.

The powder X-ray diffraction patterns of the TOPO, HDA and OA capped particles synthesized at 230 ^{o}C are shown in Fig. 2.4. The conditions at 230 ^{o}C were chosen because of the good results obtained at these temperatures. The diffraction peaks of all three samples displayed the [012], [104], [110], [006] and [202] crystal planes of the rhombohedral phase of Bi. The HDA capped Bi shows a relatively clean diffraction pattern with no traces of impurities (Fig. 2.4c). The TOPO and OA capped Bi show additional peaks which could be attributed to the presence of bismuth oxide (Fig. 2.4 a and b).

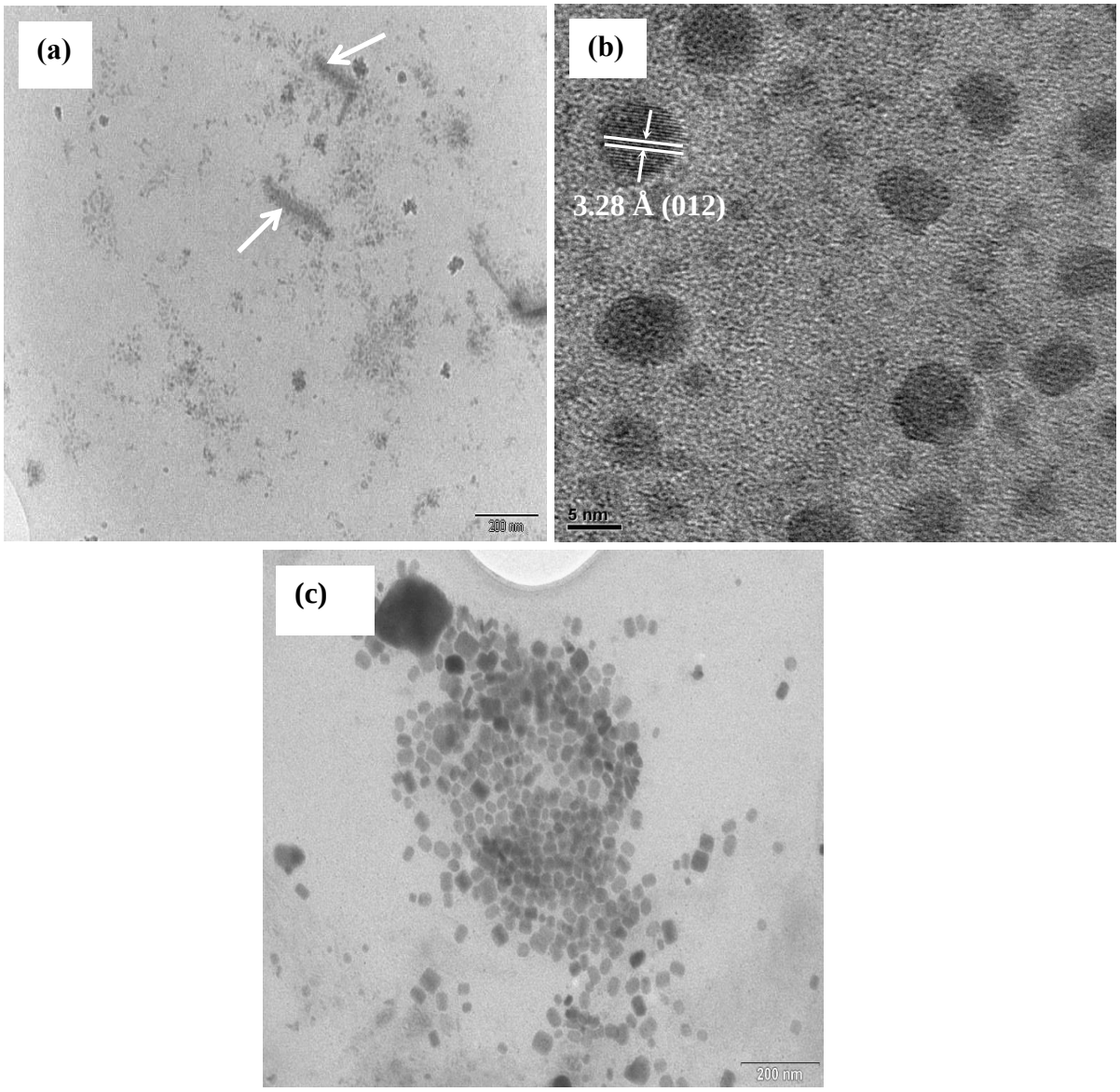

Fig. 2.3. TEM and corresponding HRTEM image of HDA capped bismuth nanoparticles synthesized at (a), (b) 230 and c) 270 ^{o}C.

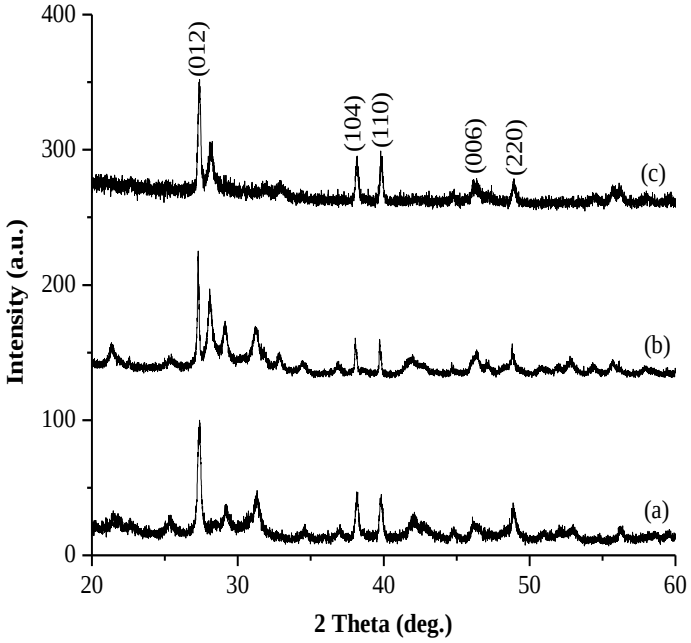

Fig. 2.4. XRD patterns of bismuth nanoparticles synthesized using different capping groups (a) TOPO, (b) OA and (c) HDA.

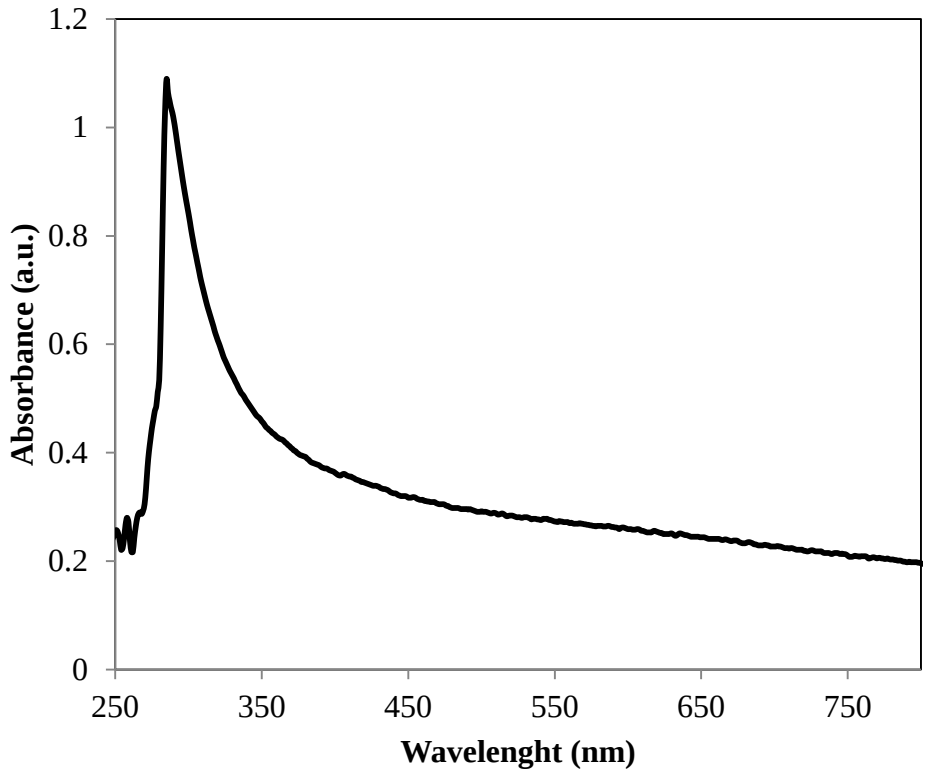

Figure. 2.5 UV/Vis absorption spectroscopy of bismuth nanoparticles capped with Hexadecylamine (HDA) synthesized at 230 ^{o}C temperature.

Figure 2.5 show an absorption spectrum for the bismuth particles synthesized using HDA at 230 ^{o}C. These UV-Visible results were similar when using OA and TOPO as capping groups. The sharp absorption peak is observed at 285 nm which is similar to the work reported before for bismuth nanoparticles [9,18]

2.3.2 TEA capped Bismuth Nanoparticles

Water soluble TEA capped bismuth nanoparticles were synthesized by using a method previously described for CdTe [19]. There have been very few reports of the use of triethanolamine as a water soluble capping group. The TEA capped Bi nanoparticles were synthesized by the simultaneous addition of reduced bismuth in a solution of triethanolamine

(TEA) at room temperature. The reaction was repeated at various pH and at temperature of 90 ºC. The reaction is quenched by the addition of acetone and methanol or ethanol to form a solution of the nanoparticles for further characterization using different techniques.

The TEM images of the TEA capped bismuth nanoparticles prepared at varying pH and temperature are shown in Fig. 2.6. The TEM image of the TEA capped nanoparticles synthesized at pH 11 (Fig. 2.6a) shows a mixture of spherical and plate-like nanoparticles which are uniformly dispersed with an average diameter of 4.9 nm. At pH 7 (Fig. 2.6b), there appears to be no change in the morphology with the average diameter of the particles at 4.6 nm. At an acidic pH of 4 (Fig. 2.6c), large aggregated nanoplates appear which is an indication of the change in shape as the pH of the solution varies. The size of the nanoplates increases as the temperature of the reaction increased at 90 ^{o}C. At pH 11 at an increased temperature of 90 ^{o}C, nanoplate aggregates (Fig 2.6d) were also observed. This change in shape has been reported previously by Wang *et al*. suggesting the shape control is influenced by temperature and pH [20].

Fig. 2.7 show the absorption spectra of TEA capped bismuth nanoparticles synthesized at pH 4, 7 and 11. The absorption spectra for all samples show a similar shape spectrum with the peak maximum at 265, 264 and 260 nm for the pH 4, 7 and 11 respectively. A strong well defined absorption peak can be attributed to the Bi–ligand complex similar for Cd-TEA [20].

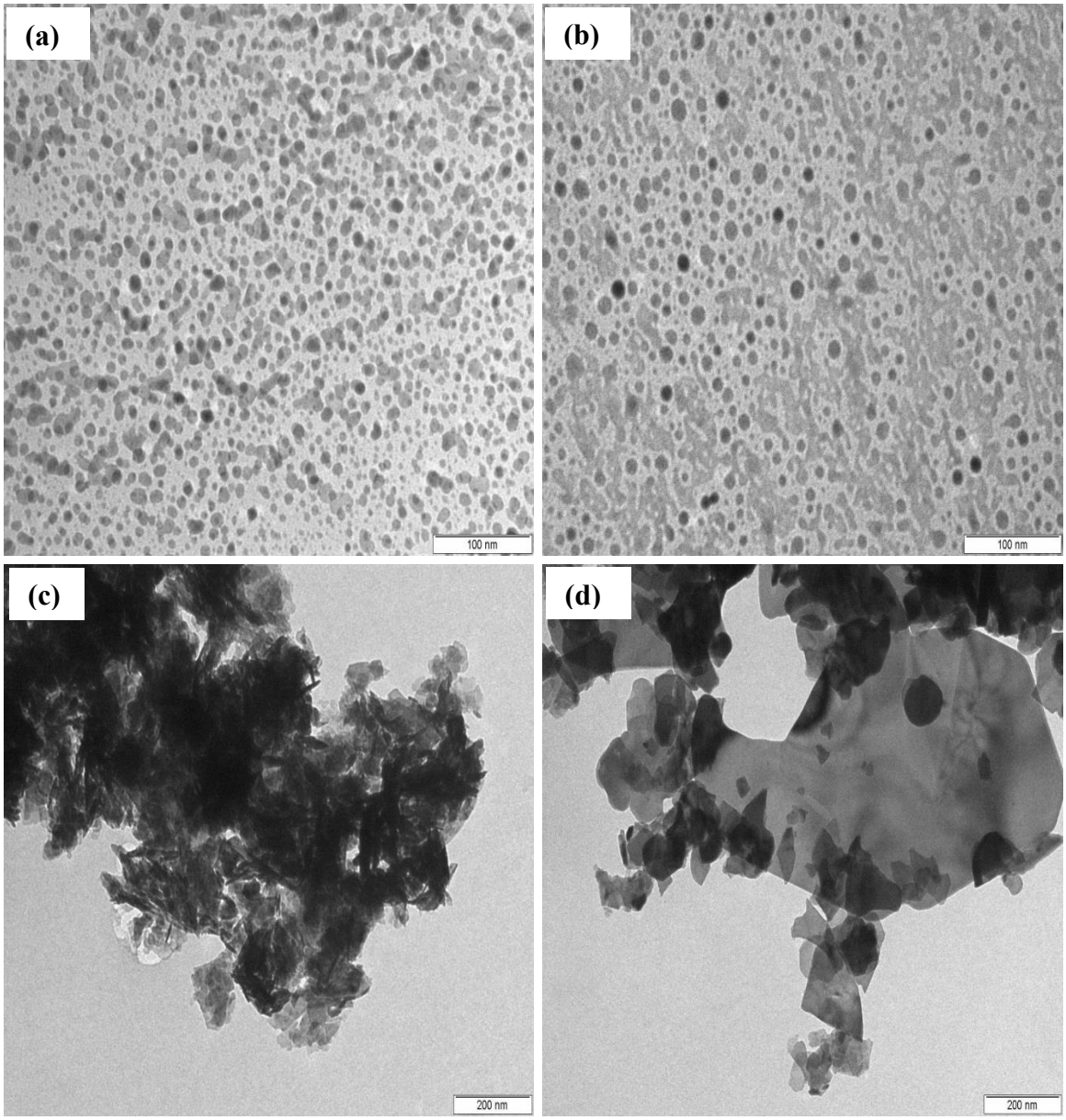

Fig. 2.6 TEM of TEA capped bismuth nanoparticles synthesized at room temperature at pH of (a) 11, (b) 7, (c) 4 and (d) pH 11 at 90 ^{o}C.

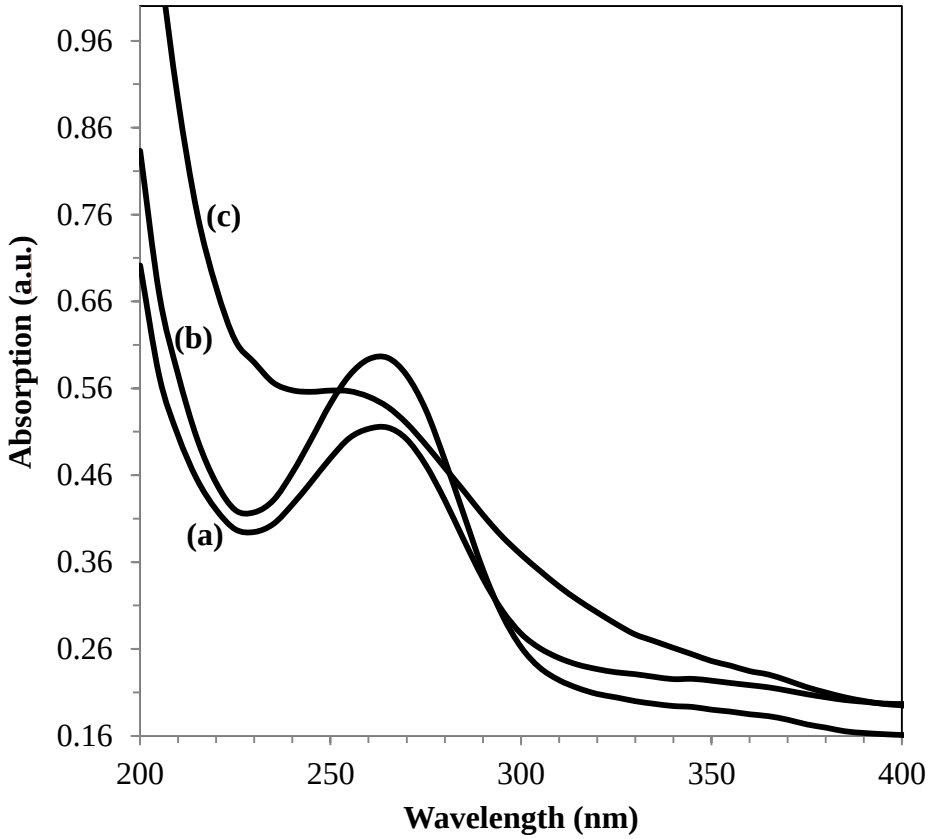

Fig. 2.7 UV/Vis absorption spectroscopy of bismuth nanoparticles capped with triethanolamine (TEA) synthesized at room temperature reaction synthesis at pH of (a) 4, (b) 7 and (c) 11.

The powder XRD pattern for the TEA capped bismuth nanoparticles synthesized at pH 11 is shown in Fig. 2.8. The pattern can be indexed to the rhombohedral crystal structure which is in good agreement with bulk Bi (JCPDS No. 05-0519) [21].

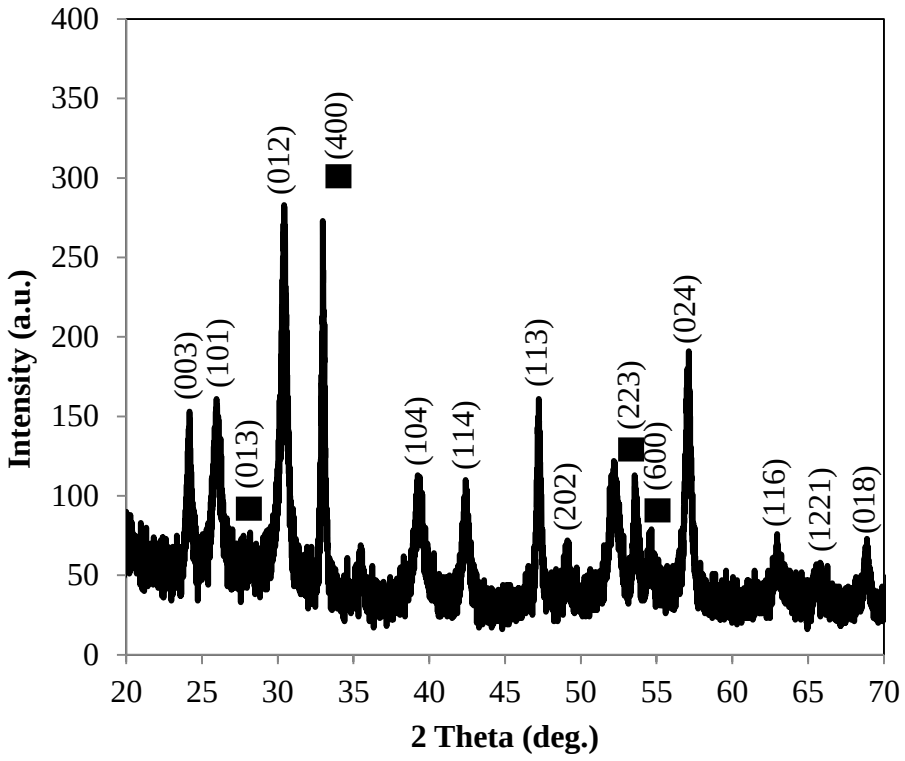

Fig.2.8 XRD of TEA capped bismuth nanoparticles prepared at pH 11. ■ show the Bi_2O_3 present.

2.4 Conclusion

The preparation of bismuth nanoparticles have been demonstrated capped by TOPO, OA and HDA. The particle morphology varied from spheres to branched nanorods to self assembled cubes. The particles were very crystalline with a dominant rhombohedral phase. The water soluble TEA capped particles yielded a mixture of spherical and nanoplates at pH 11. Nanoplates are exclusively present at pH 7 and pH 4.

2.5 References

[1] R. Fu, S. Xu, Y. Lu, J. Zhu, *Crystal. Growth. Design*. **5** (2005) 1379.

[2] P. Schaufelberger, H. Merx, M. Contre, *High Temp. High Press*. **5** (1973) 221.

[3] F. Wang, R. Tang, H. Yu, P. C. Gibbons, W. E. Buhro, *Chem. Mater*. **20** (2008) 3656.

[4] D. Ma, J. Zhao, Y. Zhao, X. Hao, L. Li, L. Zhang, Y. Lu, C. Yu, *Colloids. Surface A: Physicochem. Eng. Aspects*. **395** (2012) 276.

[5] Y. Zhao, Z. Zhang, H. Dang, *Mater. Lett*. **58** (2004) 790.

[6] M. Yarema, M. V. Kovalenko, G. Hesser, D. V. Talapin, W. Heiss, *J. Am. Chem. Soc*. **132** (2010) 15158.

[7] X. Chen, S. Chen, W. Huang, J. Zheng, Z. Li, *Electrochimica. Acta*. **54** (2009) 7370.

[8] J. Fang, K. L. Stokes, J. Wiemann, W. Zhou, *Mater. Lett*. **42** (2000) 113.

[9] J. Fang, K. L. Stokes, J. A. Wiemann, W. L. Zhou, J. Dai, F. Chen, C. J. O'Connor, *Mater. Sci. Eng. B.* **83**. (2001) 254.

[10] G. Carotenuto, C. L. Hison, F. Capezzuto, M. Palomba, P. Perlo, P. Conte, *J. Nanopart. Res*. **11** (2009) 1729.

[11] S. Onari, M. Miura, K. Matsuishi, *Appl. Surf. Sci*. **197-198** (2002) 615.

[12] J. Fang, K. L. Stokes, W. L. Zhou, W. Wang, J. Lin, *Chem. Commun*., (2001) 1872.

[13] M. D. Baltimore,18th International Conference on Thermoelectrics, *IEEE*; 1st edition (October 1999).

[14] S. R. Hostler, Y. Q. Qu, M. T. Demko, A. R. Abramson, X. Qiu, C. Burda, *Superlattices. Microstructures* **43** (2008) 195.

[15] S. O. Oluwafemi, N. Revaprasadu, *New. J. Chem*. **10** (2008) 1432.

[16] F. Xu, X. Ma, L. F. Gerlein, S. G. Cloutier. *Nanotechnology*. **22** (2011) 265604.

[17] S. K. Cho, D. V. Talapin, W. Gaschler, C. B. Murray. *J. Am. Chem.Soc*. **127** (*2005)* 7140.

[18] C. N. Tharamani, H. C. Thejaswini, S. Sampath, Bull. Mater. Sci., 31 (2008) 207.

[19] N. Mntungwa, V. S. R. Rajasekhar Pullabhotla, N. Revaprasadu, *Colloid Surface B*, **101** (2013) 450.

[20] Y. Wang, J. Zhao, X. Zhao, L. Tang, Y. Li, Z. Wang, *Mater. Res. Bull*. **44** (2009) 220.

[21] J. Wu, F. Qin, Z. Lu, H. Yang, R. Chen, *Nanoscale Research Letters* **6** (2011) 66.

3.0 Bismuth Chalcogenide (Bi_2E_3, E = S, Se and Te) Nanoparticles

3.1 Introduction

The excellent thermoelectric properties and high dimensionless figure of merit ZT values at room temperature for bismuth chalcogenides (Bi_2S_3, Bi_2Se_3, and Bi_2Te_3) have resulted in their scientific interest in recent years [1]. Special attention has been focused on the control of size of these nanoparticles. Size control is important as it determines the electric, magnetic, optical, melting points, specific heats and surface reactivity properties as a result of the quantum confinement effect [2]. As a consequence these materials have potential applications in the fabrication of optoelectronic and thermoelectric cooler devices, photovoltaic, thermoelectric transport, photoconductivity, electrical photoresponse, and field-emission [3-7].

The band gap of bismuth sulfide (Bi_2S_3) is low which is 1.33 eV and matched well with solar light spectrum [8]. This material is environmental-friendly and stable with density about 6.8 g cm^{-3} [9]. Previous reports show bismuth sulfide synthesized by mechanochemical synthesis, microwave irradiation, solvothermal process, hydrothermal synthesis and reflux methods [10-16]. Rod-like Bi_2S_3 nanoparticles have been synthesized by mixing two precursors $[Bi_6(pydc)_8(Hpydc)_2(tu)_8]$ and $\{[Bi_2(pydc)_3(tsc)(H_2O)_2] \cdot H_2O\}_\infty$ in 1-dodecanethiol (DT) and anisole or oleylamine as a capping ligand and solvent respectively [13]. The growth mechanism is believed to involve decomposition of the precursors and formation of Bi_2S_3 seeds, followed by preferential [001] growth of larger particles. Reaction parameters such as temperature, solvent and capping molecules had an influence on the morphology of the nanoparticles.

A simple one pot hydrothermal route has been reported by Zhang *et al*. [14] for the synthesis of bismuth sulfide nanoparticles with a size of 80-100 nm in length. The starting materials used

were bismuth nitrate $Bi(NO_3)_3.5H_2O$ and L-cysteine. The bismuth sulfide nanoparticles were used to form a composite with the reduced graphene oxide (RGO) which is Bi_2S_3/RGO. The reagents were stirred in water for 10 min at first, then transferred into an autoclave where they were heated at 180 ^oC for 12 h. The Bi_2S_3/RGO composite exhibited a capacity of 1073.1 $mAhg^{-1}$ with good cyclic stability when the electrochemical test was carried. Liao *et al*. [15] prepared bismuth sulfide nanorods with bismuth chloride and oleylamine followed by sulphur and oleylamine solutions. The reaction temperature and reaction time were varied as conditions in order to get the desired aspect ratio. To form a hybrid of P3HT:Bi_2S_3, these nanorods were blended with poly(3-hexlythiphene) [P3HT] at a weight ratio of 1:1.

Chen *et al*. [16] synthesized nanoparticles of bismuth sulfide which include urchin-like microsphere hierarchical nanostructures by a simple solvothermal process. Here bismuth nitrate is added to ethylene glycol (EG). When dissolved fully are then mixed with thioacetamide (TAA) in an autoclave which is heated at 160 ^oC for 18 h. Other nanostructures were obtained by replacing TAA with thiourea (TU), L-cysteine and TU using water–EG as solvent.

Bi_2Se_3 and Bi_2Te_3 have narrow band gaps of 0.3 eV and 0.15 eV respectively. They are thermoelectric (TE) materials with promising figure of merit [17,18]. It has been shown that the thermoelectric figure of merit of these materials can be improved by use of nanostructured low-dimensional materials [19,20]. Nanostructures with large grain boundaries can initiate the reduction in thermal conductivity through increased phonon scattering at the grain boundaries. In addition to their exciting thermoelectric properties Bi_2Se_3 and Bi_2Te_3 have also shown potential applications in optical recording materials [21], photoelectrochemical and electromechanical

devices [22-24]. The routes to Bi_2Se_3 vary from the specialised chemical vapour deposition technique [18,19] to microwave[20], solvothermal [21] and hydrothermal routes [22-27]. Salvati-Niasari and co-workers synthesised Bi_2Se_3 nanorods by hydrothermal method [24]. A similar hydrothermal approach was used for the synthesis of Bi_2Se_3 nanosheets, nanobelts and nanotubes [25]. The solvothermal/hydrothermal route has attracted interest due to the advantage of high yield, low temperature and the ability to control the anisotropic shape of the particles. Solvents such as ethylene glycol (EG), oleic acid (OA) and dimethyl formamide (DMF) have been used to obtain Bi_2Se_3 particles with rodlike, flake-like or tube-like morphologies [30,31].

Similarly, Bi_2Te_3 nanostructures have also been synthesized by different methods, which include the hydrothermal route [22,23, 28] , solvothermal method [29,30], reverse micelle synthesis [31], electrochemical deposition method [32,33] and microwave heating method [34]. The size of the nanostructures produced by these methods are rather larger (80-100nm) with varying morphologies such as nanorods [24] nanowires [33], nanoplates [29,30] and hierarchical nanostructures [32]. A high temperature solution based routes have also produced Bi_2Te_3 nanowires and nanotubes [35]. Badding and co-workers [35] reported a breakthrough in size controlled synthesis of Bi_2Te_3 particles in the 17-100 nm size range. The particles were capped by thiol based ligands, whose chain lengths and reaction temperatures were used to control the size of the nanostructures. Further, Weller and co-workers [36] reduced the particle size of Bi_2Te_3 to sub ~ 10 nm scale. They synthesised elemental bismuth nanoparticles in an initial step and then these nanoparticles were reacted with trioctylphosphine (TOP-Te) for the formation of bismuth tellurides nanoparticles. Ramanath and co-workers [37] synthesized polyhedral faceted Bi_2Te_3 nanocrystals by decomposing salts of bismuth acetate and trioctylophosphine(TOP)-

ligated tellurium. The bismuth acetate was first mixed with oleylamine and oleic acid to form a bismuth-oleylamine complex. The TOP-Te solution was injected into the bismuth solution to form the oleic acid capped Bi_2Te_3 nanocrystals. Despite the availability of number of methods for the synthesis of bismuth chalcogenides nanoparticles, only a very few methods have successfully produced these materials in smaller size regime with distinct shape.

In this chapter a facile hybrid solution based method for the controlled synthesis of bismuth sulfide (Bi_2S_3), bismuth selenide (Bi_2Se_3) and bismuth telluride (Bi_2Te_3) nanoparticles in organic capping groups is reported. In addition the method was adapted to prepare water soluble triethanolamine (TEA) capped Bi_2S_3 nanoparticles.

3.2 Experimental

3.2.1 Chemicals

Bismuth chloride ($BiCl_3$), bismuth acetate [$Bi(CH_3COO)_3$], bismuth nitrate [$Bi(NO_3)_3$], bismuth carbonate [$Bi_2(CO_3)O_2$] salts, sodium borohydride ($NaBH_4$), deionised water, methanol, toluene, hexadecylamine (HDA) and tri-*n*-octylphosphine (TOP) were purchased from Aldrich. All chemicals were of analytical grade and used directly as purchased without any further purification.

3.2.2 Synthesis of HDA capped Bi_2S_3 nanoparticles

In a typical room temperature reaction, sulfur powder (0.32 mmol) was mixed with deionised water (20.00 mL) in a three-necked flask. Sodium borohydride (0.79 mmol) was carefully added

to this mixture and the flask was immediately purged with nitrogen gas to create an inert atmosphere. After 2 h, bismuth chloride (0.32 mmol) was dissolved in deionised water (20.00 mL) and was added to the yellow sulfur ion solution to give dark brown solution. The solution was then stirred for about 30 min followed by the addition of excess methanol. The resultant solution was then centrifuged. The Bi_2S_3 produced was dispersed in tri-*n*-octylphosphine (TOP) and stirred continuously to form a TOP- Bi_2S_3 dispersion, which was then injected into hot hexadecylamine (HDA) at 190 ^oC. The temperature was kept constant at 190 ^oC for 2 h. After this time methanol was added to the cooled reaction mixture resulting in the reversible flocculation of the nanoparticles. The flocculate was separated from the supernatant by centrifugation. The resultant particles were dissolved in toluene to give a solution of bismuth sulphide nanocrystallites for characterization.

3.2.3 Synthesis of HDA capped Bi_2Se_3 nanoparticles

The procedure for the synthesis of HDA capped Bi_2S_3 nanoparticles was repeated with sulphur powder being replaced by selenium powder (0.32 mmol).

The similar reaction conditions were used by changing the bismuth source with bismuth acetate [$Bi(CH_3COO)_3$], bismuth nitrate [$Bi(NO_3)_3$], bismuth carbonate [$Bi_2(CO_3)O_2$] salts. The reaction was also studied at various temperature conditions, 230 and 270 ^oC.

3.2.4 Synthesis of HDA and OA capped Bi_2Te_3 nanoparticles

The above process was followed for the synthesis of bismuth sulphide nanocrystals but using tellurium. In addition, oleylamine was also used as a capping ligand.

3.2.5 Synthesis of TEA capped Bi_2S_3 nanoparticles

In a typical room temperature reaction, sulphur powder (0.32 mmol) was mixed with deionised water (10.0 mL) in a three-necked flask. 10.0 mL aqueous solution of sodium borohydride (0.79 mmol) was carefully added to this mixture and the flask was immediately purged with nitrogen gas to create an inert atmosphere. After 2 h, 20.0 mL aqueous solution of $BiCl_3$ (0.32 mmol) and 20.0 mL of TEA solution (6.40 mmol) with a molar ratio of 1:20 (Bi^{3+}: cysteine ester) were added simultaneously to the yellow sulphur ion solution. The pH of the solution was raised to 11 by using HCl (0.10 M) and NH_3 (0.10 M) solutions after which the solution was then kept at room temperature for 3 h. After completion of the reaction, excess methanol was added resulting in the reversible flocculation of the nanoparticles. The flocculate was separated from the supernatant by centrifugation. The resultant particles were dissolved in acetone to give a solution of nanocrystallites for characterization.

3.3 Results and discussion

The hybrid solution based high temperature route has been successful in synthesizing different sizes and shapes of cadmium and lead chalcogenide nanocrystals [38,39]. The control of the size and shape of nanocrystals was achieved by adjusting the reaction parameters. It was found out that the nature of the metal salt has an influence on the particle morphology [40]. The work described in this chapter is an extension to the hybrid solution method. Reaction conditions such as metal salts and reaction temperature was varied to obtain good quality Bi_2S_3, Bi_2Se_3 and Bi_2Te_3 nanocrystals. Previous work on bismuth selenide has shown that controllable and selective synthesis of nanostructures could be achieved by adjusting the solvents in solvothermal

routes. The synthesis of monodisperse sub 10 nm bismuth chalcogenides (Bi_2Se_3 and Bi_2Te_3) with regular shapes is challenging. The difficult in controlled growth of small bismuth chalcogenide nanoparticles via solution-process is the high reactivity of reduced form of selenium and tellurium with bismuth salts. The reaction for the formation of bismuth chalcogenide is as follows:

Step 1: $4\ NaBH_4 + 2\ E + 7\ H_2O \rightarrow 2\ NaHE + Na_2B_4O_7 + 14\ H_2$

Step 2: $NaHE + BiCl_2 \rightarrow Bi_3E_2 + NaCl + HCl$

Where E = S, Se and Te

The resultant bismuth chalcogenide particles were isolated by centrifugation then dispersed in tri-n-octylphosphine (TOP) and injected into hot capping group which serves as a coordinating solvent.

3.3.1 HDA capped Bi_2S_3 Nanoparticles

Bi_2S_3 nanoparticles were synthesized in a two step solution based route. Bulk Bi_2S_3 was synthesized by the reduction of sulphur powder in water followed by addition of bismuth chloride. The pre – formed Bi_2S_3 was then thermolysed in HDA at 230 ºC. Fig. 3.1 shows the TEM image of HDA capped Bi_2S_3 nanoparticles. The morphology of the particles is in the form of rods with dimensions of average length of 3.3 nm and width of 2.4 nm. There also appears to be some spherical particles with a degree of agglomeration. The rod formation is characteristic of HDA capped nanoparticles as it is a weakly binding ligand allowing the growth of elongated

particles [41-43]. The XRD pattern of the HDA capped Bi_2S_3 as shown in Figure 3.2 is in agreement with the orthorhombic phase of Bi_2S_3 (JCPDS card no: 17-0320).

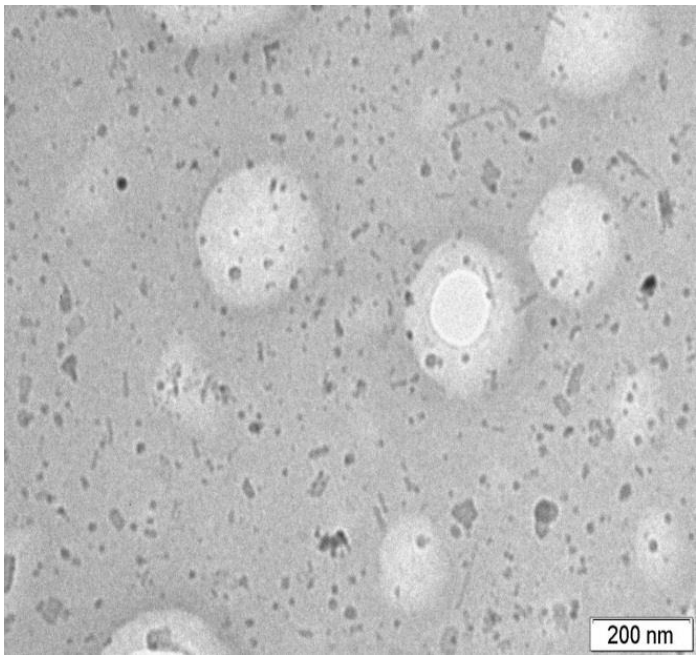

Fig. 3.1 TEM of HDA capped Bi_2S_3 nanoparticles synthesized at 230 ^oC.

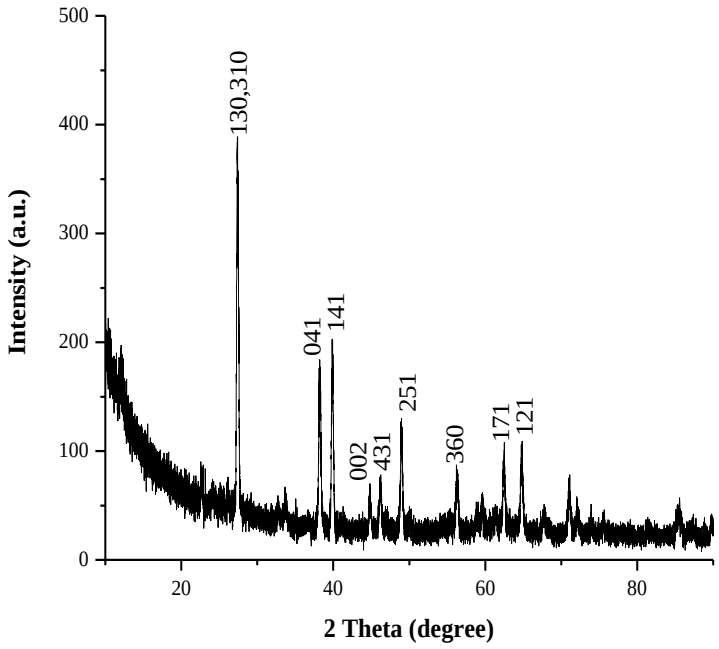

Fig. 3.2 Powder XRD of HDA capped Bi_2S_3 nanoparticles synthesized at 230 ^oC.

3.3.2 HDA and OA capped Bi_2Se_3 and Bi_2Te_3 Nanoparticles

The sulfur source was replaced by selenium and tellurium in the preparation of Bi_2Se_3 and Bi_2Te_3 nanoparticles. The bismuth salt and reaction temperatures were also varied. Fig. 3.3a TEM image of HDA capped Bi_2Se_3 nanoparticles synthesized at 190 ºC using bismuth chloride as the bismuth salt. The particles are spherical in shape with an average diameter of 13.69 ± 1.59 nm. The corresponding high resolution TEM image in Fig. 3.3b shows spherical particles with distinct lattice fringes. The lattice spacing of 0.346 nm corresponds to the (110) planes of rhombohedral Bi_2Se_3. When the bismuth source was changed to bismuth nitrate at a higher reaction temperature (270 ºC), faceted particles of Bi_2Se_3 were obtained (Fig. 3.4a). However the average particle size decreased to 10.32 ± 1.91 nm. A single faceted particle of Bi_2Se_3 is

observed in the HRTEM image (Fig. 3.4b). The lattice fringes show some dislocations and the particles appear to be fused to another particle. However the distinct cubic edged particle confirms the shape observed in the TEM image. Another portion of the grid shows a close to spherical particle with distinct lattice fringes (Fig. 3.4c).

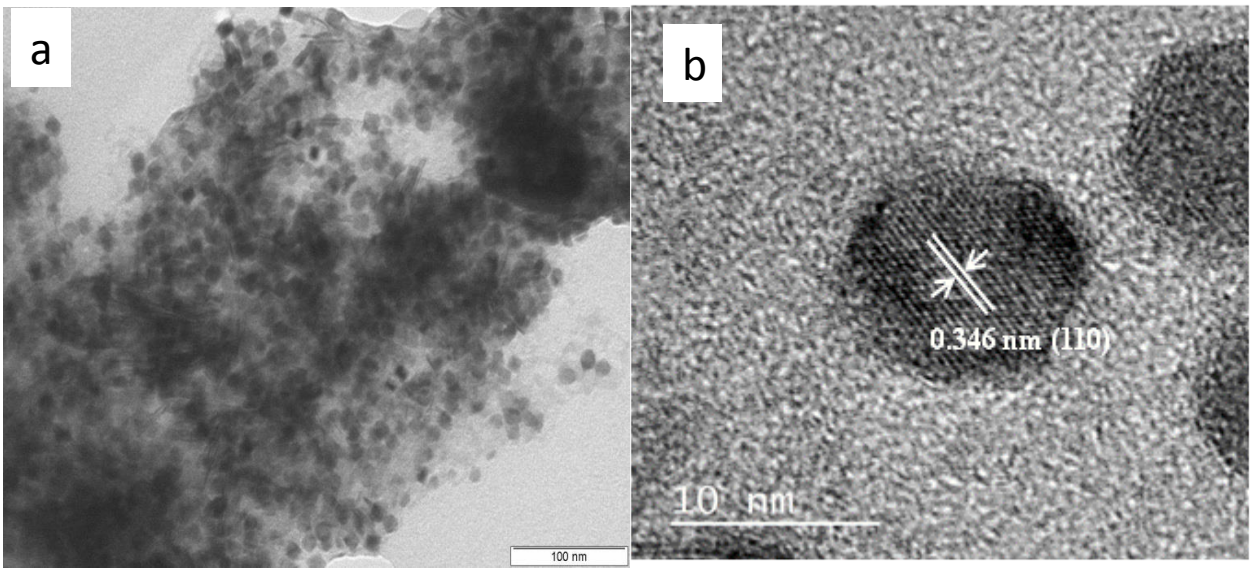

Fig. 3.3. (a) TEM image of HDA capped Bi_2Se_3 nanoparticles synthesized from $BiCl_3$ at 190 ºC and (b) corresponding HRTEM image

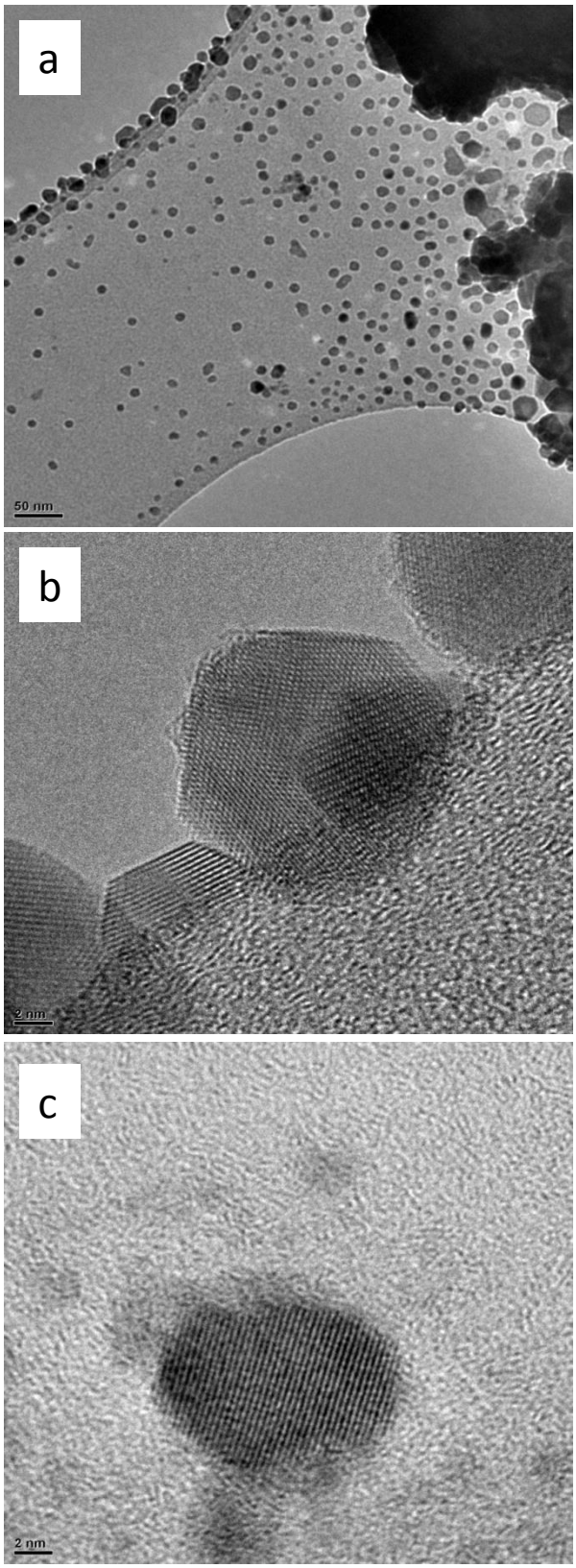

Fig. 3.4 (a) TEM image of HDA capped Bi_2Se_3 nanoparticles synthesized from $BiNO_3$ at 270 ºC and (b,c) corresponding HRTEM images.

The powder X-ray diffraction of the HDA capped Bi_2Se_3 particles synthesized at 270 ºC is shown in Fig. 3.5. The XRD pattern shows peaks which are characteristic of the orthorhombic phase of Bi_2Se_3 (ICDD 33-0214).

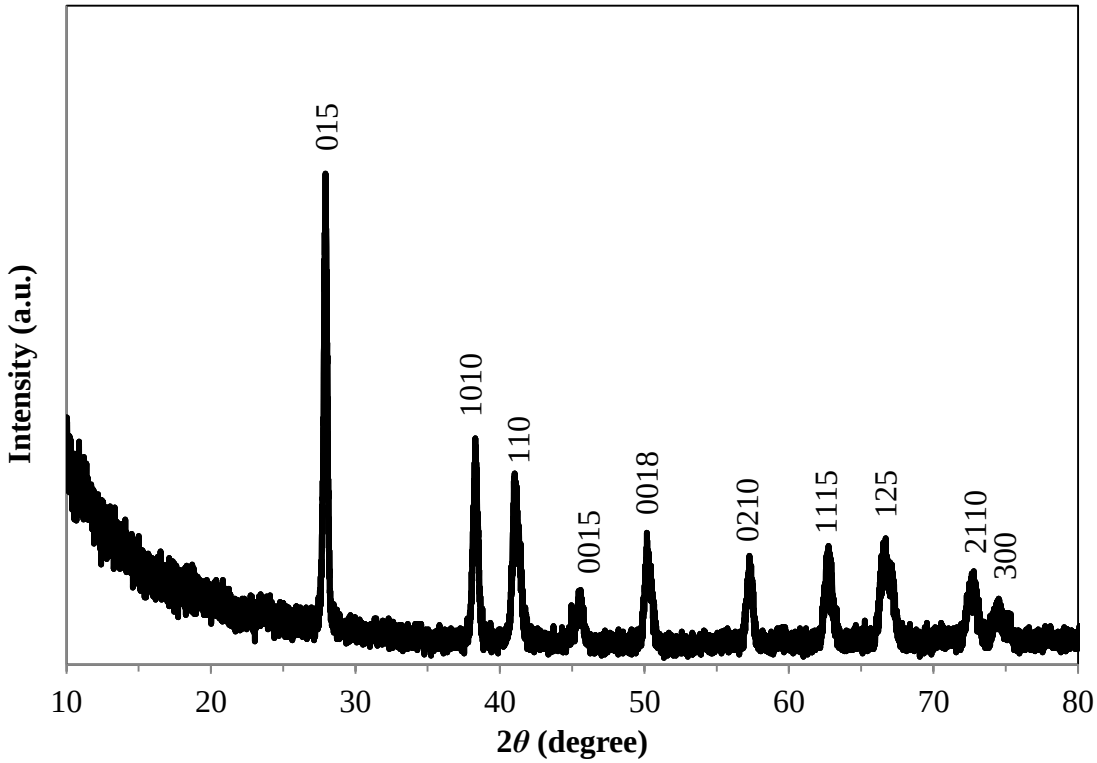

Fig. 3.5. Powder XRD pattern of HDA capped Bi_2Se_3 nanoparticles synthesized from $BiNO_3$ at 270 ºC.

Bi_2Te_3 nanoparticles were synthesized in HDA at 230 ºC using the bismuth acetate as the metal salt. The TEM image shows well dispersed spherical particles with an average diameter of 22.27 ± 5.82 nm (Fig. 3.6a). The HRTEM image shows a single spherical particle with a diameter of 21.7 nm (Fig. 3.6b).

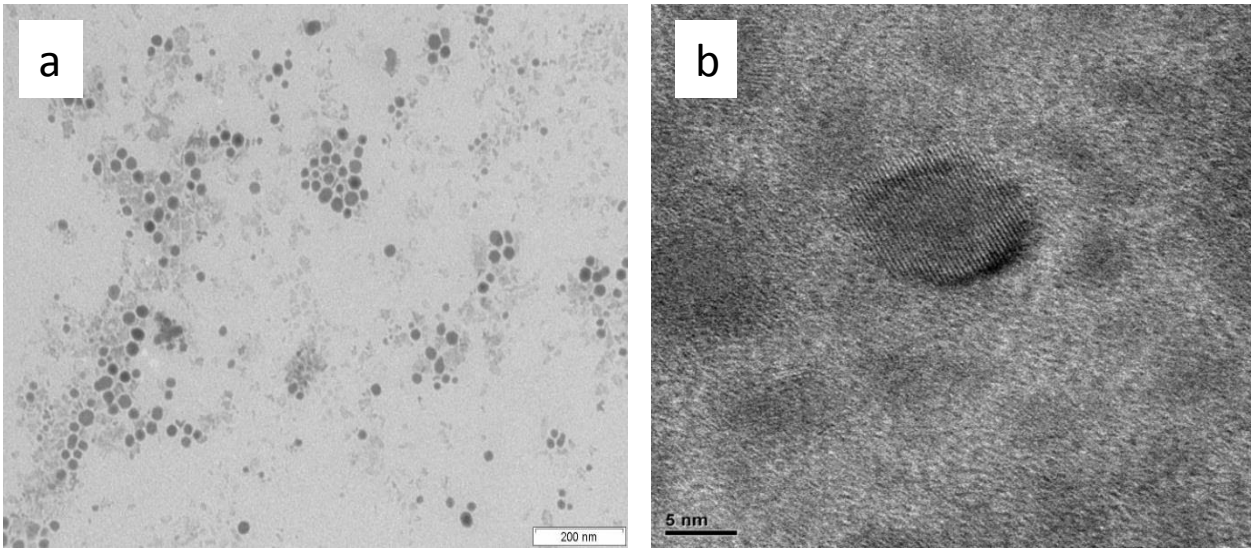

Fig. 3.6. (a) TEM images of HDA capped Bi_2Te_3 nanoparticles synthesized from $Bi(CH_3COO)_3$ at 230 º and (b) corresponding HRTEM image.

Oleylamine (OA) was then used as a capping group at a relatively low temperature of 190 ºC. This reaction produced close to spherical OA capped Bi_2Te_3 particles as observed in the TEM image (Fig. 3.7a). The average diameter of the particles was 23.88 ± 4.49 nm. Particles with distinct lattice fringes are observed in the HRTEM image (Fig. 3.7b) with the lattice spacing of 0.220 nm consistent with the [110] plane of orthorhombic Bi_2Te_3. The corresponding XRD pattern (Figure 3.8) shows that peaks are consistent with the rhombohedral structure of Bi_2Te_3 (ICDD 15-0863).

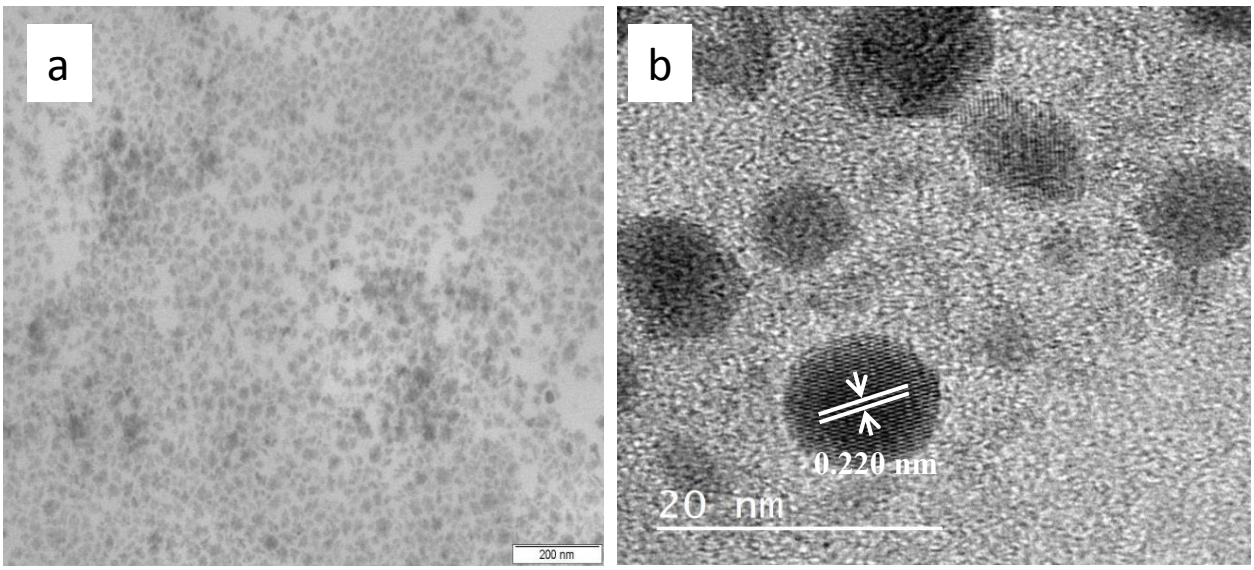

Fig. 3.7 (a) TEM images of OA capped Bi_2Te_3 nanoparticles synthesized from $Bi(CH_3COO)_3$ at 190 º and (b) corresponding HRTEM image.

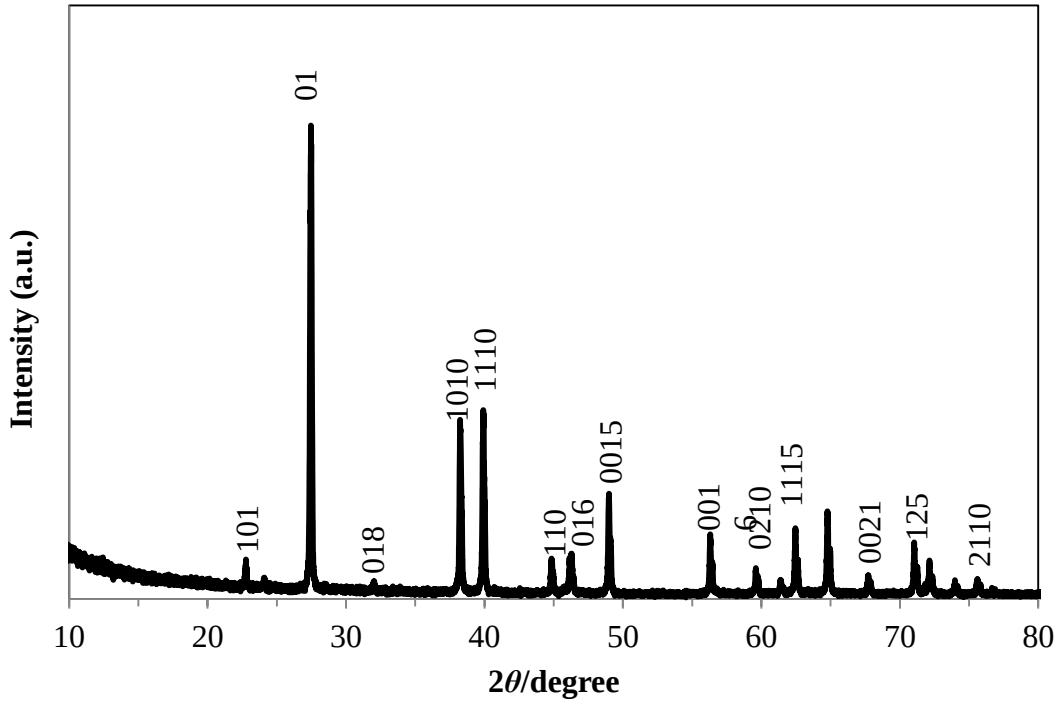

Fig. 3.8 Powder XRD pattern of OA capped Bi_2Te_3 nanoparticles synthesized from $Bi(CH_3COO)_3$ at 190 ºC.

3.3.3 TEA capped Bi_2S_3 nanoparticles

The synthetic route was adapted to synthesize water soluble TEA capped Bi_2S_3 nanoparticles. The work was extended to the bismuth sulfide chalcogenide because we did not get good quality HDA capped particles in comparison to the selenides and tellurides. The reduced sulphur solution was added to a solution of the bismuth salt and TEA at room temperature at a pH 11. The TEM image of the TEA capped Bi_2S_3 is shown in Fig. 3.9. The particles display a rod shaped morphology as reported previously in the literature [44, 45]. The nanorods lie across each other with an average length of 260 nm and width of 25 nm.

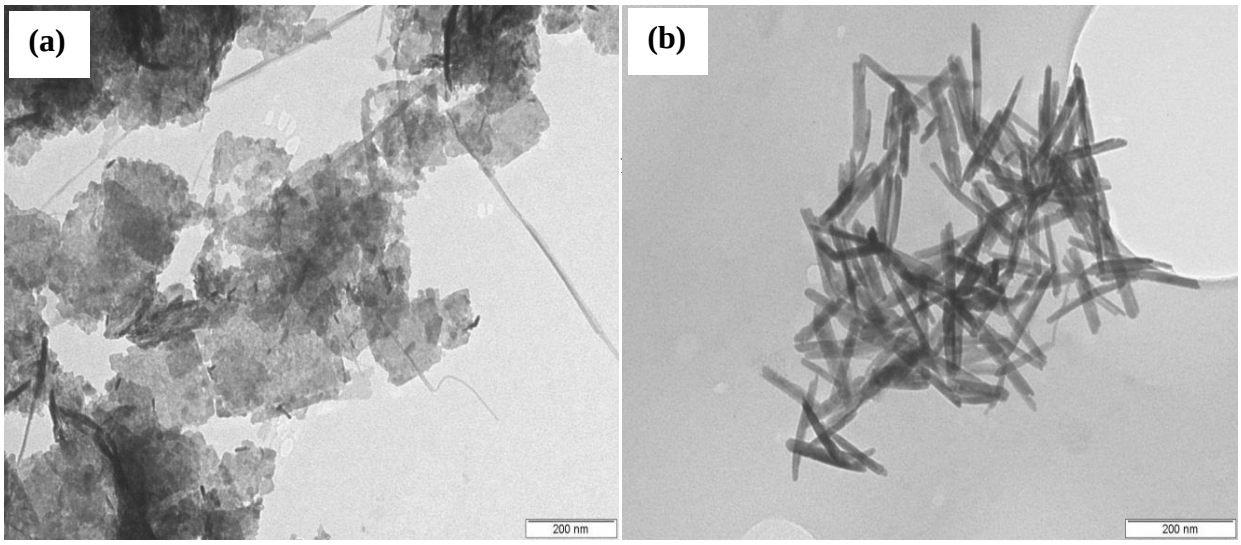

Fig. 3.9 TEM images of Bismuth sulfide prepared in (a) TEA and (b) cysteine

The XRD pattern (Fig. 3.10) of TEA capped particles showing crystal structure of these nanoparticles as indexed by their corresponding diffraction peaks. The peaks are broad an indication of the small size of the particles. The [130], [310], [122], [141], [501] and [351] planes of orthorhombic Bi_2S_3 were indexed.

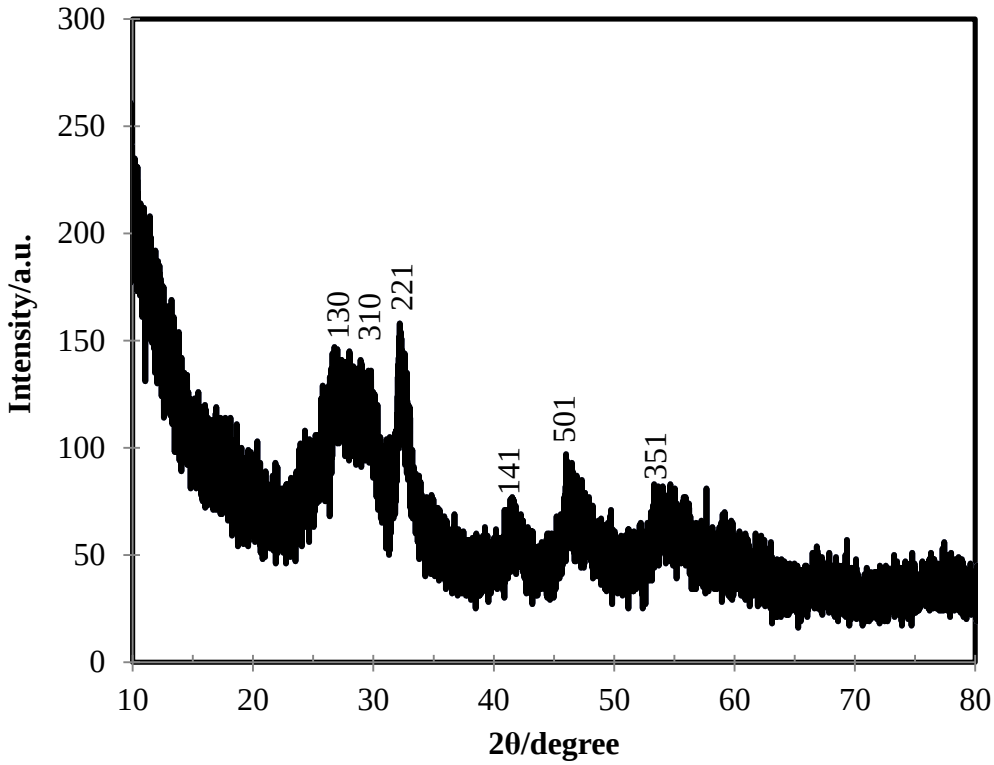

Fig. 3.10 XRD of TEA capped Bi_2S_3 nanoparticles.

3.4 Conclusions

A facile hybrid solution method was developed for the synthesis of nearly monodisperse Bi_2Se_3 and Bi_2Te_3 nanocrystals. This synthesis process yielded spherical shaped Bi_2Se_3 nanocrystals at 190 ºC, and faceted nanocrystals at 270 ºC. A similar reaction process for bismuth telluride gave only the spherical nanocrystals at all temperatures with hexadecylamine and oleylamine capping groups. The bismuth sulfide nanoparticles were rod-shaped for both water soluble and organically soluble nanoparticles.

3.5 References

[1] J. R. Sootsman, D. Y. Chung, M. G. Kanatzidis, *Angew. Chem. Int. Ed*. **48** (2009) 8616.

[2] K. J. Klabunde, *Nanoscal. Mater. Chem*., **1** (2001) 1.

[3] S. Liufu, L. Chen, Q. Yao, C. Wang, *Appl. Phys. Lett*. **90** (2007) 112106.1.

[4] G. Konstantatos, L. Levina, J. Tang, E. H. Sargent, *Nano Lett*. **8** (2008) 4002.

[5] S. K. Batabyal, C. Basu, A. R. Das, G. S. Sanyal, *J. Nanosci. Nanotechnol*. **7** (2007) 565.

[6] X. Yu, C. Cao, *Cryst. Growth Des*. **8** (2008) 3951.

[7] J. D. Desai, C. D. Lokhande, *Mater. Chem. Phys*. **41** (1995) 98.

[8] T. Thongtem, C. Pilapong, J. Kavinchan, A. Phuruangrat, S. Thongtem, *J. Alloy. Compds*. **500** (2010) 195.

[9] H. Liao, M. Wu, M. Jao, C. Chuang, Y. Chen, W. Su, *Cryst. Eng. Comm*, **14** (2012) 3645.

[10] E. Dutkova, L. Takacs, M. J. Sayagues, P. Balaz, J. Kovac, A. Satka, *Chem. Eng. Sci*., **85** (2013) 25.

[11] J. Wu, F. Qin, G. Cheng, H. Li, J. Zhang, Y. Xie, H. Yang, Z. Lu, X. Lu, R Chen, *J. Alloy. Comps*., **509** (2011) 2116.

[12] Y. Li, Y. Zhang, Y. Lei, P. Li, H. Jia, H. Hou, Z. Zheng, *Mater. Sci. Eng. B* **177** (2012) 1764.

[13] L. R. Windmiller, *Phys. Rev*., **149** (1966) 472.

[14] Z. Zhang, C. Zhou, L. Huang, X. Wang, Y. Qu, Y. Lai, J. Li, *Electrochimica Acta*, **114** (2013) 88.

[15] H. Liao, M. Wu, M. Jao, C. Chuang, Y. Chen, W. Su, *Cryst. Eng. Comm*, **14** (2012) 3645.

[16] J. Chen, S. Qin, G. Song, T. Xiang, F. Xin, X. Yin, *Dalton. Trans*., **42** (2013) 15133.

[17] H. J. Goldsmit *J. Appl. Phys* **32** (1961) 2198.

[18] X. B. Xhao, X. H. Ji, Y. H. Zhang, T. J. Zhu, J. P. Tu, X. B. Zhang. *Appl. Phys. Lett*. **86** (2005) 06211.

[19] G. Chen, M. S Dresselhaus, G Dresselhaus, J. P Fleurial, T Caillat, *Int. Mater. Rev*. **48** (2003) 45.

[20] L. D. Hicks, M. S Dresselhaus, *Phys. Rev. B*. **47** (1993) 12727.

[21] C. W Bates, L England. *Appl. Phys. Lett*. **14** (2009) 390.

[22] N. Sakai, T. Kajiwara, K. Takemura, S. Minomura, Y. Fujii. *Solid State Commun*. **40** (1981) 1045.

[23] A. Giani, A. A Bayaz, A Foucaran, F Pascal-Delannoy, A Boyer, *J. Cryst. Growth*, **236** (2002) 217.

[24] Y. Jiang, Y.J Zhu, *J. Cryst. Growth*, **306** (2007) 351.

[25] G. Q Zhang, W Wang, X. L Lu, X. G Li, *Cryst. Growth Des*. **9** (2009) 145.

[26] J. R Ota, P Roy, S. K Srivastava, R Ropovitz-Biro, R Tenne, *Nanotechnology*, **17** (2006) 1700.

[27] M. Salavati-Niasari, M. Bazarganipour, J. Davar, *J. Alloys and Compds*, **489** (2010) 530.

[28] M. Salavati-Niasari, M. Bazarganipour, J. Davar, *Inorg. Chim, Acta*. **56** (2011) 5085.

[29] G. Q. Zhang, W. Wang, X. L. Lu, X. G. Li, *Cryst. Growth Des*. **9** (2009) 145.

[30] Y. Liang, W. Wang, B. Zeng, G. Zhang, Q. Zhang, Q. He, J. Fu, *Mater. Chem. Phys*. **129** (2011) 90.

[31] E. Foos, R. Stroud, A. Berry, *Nano Lett*, **1** (2001) 693.

[32] G. R. Li, F. L. Zheng, Y. X Tong, *Cryst. Growth Des*, **8** (2008) 1226.

[33] Y. Jiang, Y. J. Zhu, J. *Cryst. Growth*, **306** (2007) 351.

[34] Z. Chai, Z. Peng, C. Wang, H. Zhang, *Mater. Chem. Phys*., **113** (2009), 664.

[35] M. R. Dirmyer, J. Martin, G. S. Nolas, A. Sen, J. V. Badding, *Small*, **8** (2009) 933.

[36] M. Scheele, N. Oeschler, K. Meier, A. Kornowski, C. Klinke, H. Weller, *Adv. Funct. Mater*, **19** (2009) 3476.

[37] A. Purkayastha, A. Jain, C. Hapenciuc, R. Buckley, B. Singh, C. Karthik, R. J. Mehta, T. Borca- Tasiuc, G. Ramanath, *Chem. Mater*. **23** (2011) 3029.

[38] N. Mntungwa, V.S.R Rajasekhar Pullabhotla, N. Revaprasadu, *J. Mater. Chem and Phys*, **126** (2011) 500.

[39] K. Ramasamy, N. Ziqubu, V. S. R. Rajasekhar Pullabhotla. O. A. Nejo, A. A. Nejo, N. Revaprasadu, P. O'Brien, *Eur. J. Inorg. Chem.* (2011**)** 5196.

[40] N. Ziqubu, K. Ramasamy, N. Revaprasadu, V.S.R. Rajasekhar Pullabhotla and P. O'Brien, *Chem. Mater*, **22** (2010) 3817.

[41] L. Qu, X. Peng, *J. Am. Chem. Soc*. **124** (2002) 2049.

[42] D.V. Talapin, A.L. Rogach, A. Kornowski, M. Haase, H. Weller, *Nano Lett*. **1** (2001) 207.

[43] K. Nose, H. Fujita, T. Omata, S.O.Y. Matsuo, H. Nakamura, H. Maeda, *J. Lumin*. **126** (2007) 21.

[44] Z. Chen, M. Ca, *Mater. Res. Bull*., **46** (2011) 555.

[45] Y. Jiang, Y. Zhu, Z. Xu, *Mater. Lett*., **60** (2006) 2294.

4.0 Antimony and antimony chalcogenide (Sb_2E_3, E = S, Se and Te) nanoparticles

4.1 Introduction

Antimony (Sb) is a semimetal with the same crystal structure as bismuth with an energy overlap between valence and conduction band of about 180 meV at 4.2 K [1]. This material has potential for thermoelectric applications due to its highly anisotropic behavior, low conduction band, effective mass and high electron mobility. This material finds usage in electronics such as an anode in Li-ion battery due to its high Li-storage capacity [2]. Sb acts as a anode because of its capacity for Li-storage. There have been few reports on the synthesis of antimony nanoparticles. Methods of synthesis include the solvothermal, mechanochemical reduction, ultrasonic force microscopy and solution phase methods [3-7]. Yang *et al*. [8] reported large scale synthesis of antimony dendritic nanocrystals by the reduction of Sb^{3+} with zinc powder at room temperature in an aqueous or alcoholic solution. It was found that the homogeneous Sb^{3+} solution and rapid reduction reaction plays an important role in the formation of nanoscale dendrites. The formation of dendritic nanocrystals was attributed to the preferred orientated aggregation and growth of Sb nanoparticles due to the intrinsically strong crystalline anisotropy of Sb. Another route to Sb nanoparticles is the reduction of $SbCl_5$ or $SbCl_3$ using *t*-BuONa-activated sodium hydride as the reducing agent and *t*-BuONa as a stabilizer in THF [9]. Monodispersed nanoparticles possessing diameters of about 4.7 ± 1.9 nm were obtained after 2 h reduction at 65 ^oC. A ligand exchange with aniline on t-BuONa-stabilized Sb(0) particles synthesized using this method was performed which yielded aniline-stabilized particles [10]. Ammonium persulfate was used to polymerize the aniline-stabilized Sb(0) particles to produce Sb(0)/PANI nanocomposites.

Antimony chalcogenide (Sb_2S_3, Sb_2Se_3, Sb_2Te_3) nanoparticles are suitable for diverse applications including thermoelectric, photovoltaic, photoconductive and field emission devices [11,12]. These materials have been synthesized using a chemical route, solvothermal synthesis and the sonication procedure [13-15]. Alemi *et al*. [16] used a hydrothermal method to prepare antimony sulfide nanorods by reacting elemental sulfur, antimony and iodine as precursors at 180 ^{o}C for 24 h. The nanorods had lengths of 4 μm and diameters of about 50-140 nm, with a rhombohedral structure. The band gap of the material obtained was around 2.50 eV which is a blue shift as compared to the bulk material.

A facile wet-chemical method was reported by Kavinchan *et al*. [17] for the synthesis of antimony sulfide by using precursors such as antimony chloride ($SbCl_3$) and sodium thiosulfate pentahydrate ($Na_2S_2O_3 . 5H_2O$) in ethylene glycol. The reaction parameters such as temperature and reaction time were varied to obtain optimum conditions for the synthesis of these materials. When analyzing the particles, an orthorhombic structure was observed with coral-like, straw-tied like and flower-like morphologies.

Antimony telluride (Sb_2Te_3) nanoparticles were reported by Kim *et al*. via a water-based chemical reaction under atmospheric conditions [18]. They employed a complexing agent (L-tartaric acid) and a reducing agent ($NaBH_4$) to stabilize the Sb precursor ($SbCl_3$) in water and to favor the reaction with Te. In order to obtain pure rhombohedral Sb_2Te_3, the aging time of the reaction needed to be adjusted. Antimony selenide (Sb_2Se_3) nanorods were produced by using dialkyldiselenophosphate (dsep) complexes [19]. Raman spectroscopy showed that these nanorods synthesized at a lower temperature contain a small amount of Sb_2Se_3. There have been

few reports on the synthesis of these materials as a result more work is required to study their fundamental properties.

In this chapter the synthesis of antimony and antimony chalcogenides nanoparticles is described. The Sb nanoparticles were synthesized by a similar route to bismuth nanoparticles as described in Chapter 2. Antimony chloride is reduced followed by the thermolysis in a coordinating solvent such as tri-n-octylphosphine oxide (TOPO) and oleylamine (OA). The antimony chalcogenides were synthesized by a similar route to the bismuth chalcogenides, described in Chapter 3.

4.2 Experimental

4.2.1 Chemicals

Antimony chloride ($SbCl_3$), tellurium powder, selenium powder, sulfur powder, sodium borohydride ($NaBH_4$), deionized water, methanol, tri-n-octylphosphine (TOP), hexadecylamine (HDA), tri-n-octylphosphine oxide (TOPO), oleylamine (OA) and toluene were purchased from Sigma Aldrich. All chemicals were of analytical grade and used directly as purchased without further purification.

4.2.1.1 Synthesis of Sb nanoparticles

In a typical room temperature reaction, antimony chloride (0.073 g, 0.32 mmol) was mixed with deionised water (10.0 mL) in a three-necked flask. The solution of 10 mL sodium borohydride (0.031 g, 0.79 mmol) was carefully added to this mixture and the flask was immediately purged with nitrogen gas to create an inert atmosphere. The mixture was stirred for 2 h followed by the

addition of excess methanol. The resultant solution was then centrifuged. The black particles produced were dispersed in tri-n-octylphosphine, TOP (6.0 mL) and stirred continuously to form a TOP–Sb solution, which was then injected into hot TOPO (6.0 g) at 190 °C. A sudden decrease in temperature was observed. The temperature was kept constant at 190 °C for 2 h. An immediate addition of methanol resulted in the reversible flocculation of the nanoparticles. The flocculate was separated from the supernatant by centrifugation. The resultant particles were dissolved in toluene to give a solution of nanocrystallites for characterization. The above reaction procedure was repeated by replacing TOPO with OA at 230 ^{o}C.

4.2.1.2 Synthesis of Sb_2S_3 nanoparticles

In a typical room temperature reaction, sulfur powder (0.0410 g, 0.128 mmol) was mixed with deionised water (80.0 mL) in a three-necked flask. Sodium borohydride (0.12 g, 3.24 mmol) was carefully added to this mixture and the flask was immediately purged with nitrogen gas to create an inert atmosphere. After 2 h, $SbCl_3$ (0.29 g; 3.24 mmol) was dissolved in deionised water (80.0 mL) and added to the yellow coloured NaHS solution. The solution was stirred for 30 min followed by the addition of excess methanol. The resultant solution was then centrifuged. The Sb_2S_3 produced was dispersed in tri-*n*-octylphosphine, TOP (3.0 g) and stirred continuously to form a TOP– Sb_2S_3 solution, which was then injected into hot OA (3.0 g) at 230 ^{o}C. A sudden decrease in temperature was observed. The temperature was kept constant at 230 ^{o}C for 30 minutes. After the reaction time an immediate addition of methanol resulted in the reversible flocculation of the Sb_2S_3 nanoparticles. The flocculate was separated from the supernatant by centrifugation. The resultant particles were dissolved in toluene to give an optically clear solution of OA capped Sb_2S_3nanocrystallites for characterization.

4.2.1.3 Synthesis of Sb_2Se_3 nanoparticles

The procedure for the synthesis of OA capped Sb_2S_3 nanoparticles was repeated with sulfur powder being replaced by selenium powder (0.10 g, 0.128 mmol). In another reaction OA is replaced with HDA.

4.2.1.4 Synthesis of Sb_2Te_3 nanoparticles

The procedure for the synthesis of OA capped Sb_2S_3 nanoparticles was repeated with sulfur powder being replaced by tellurium powder (0.16 g, 0.128 mmol). In another reaction OA is replaced with HDA.

4.3 Results and discussion

4.3.1 Sb nanoparticles

The synthesis of Sb nanoparticles is carried by the reduction of $SbCl_2$ using a reduction agent to change the oxidation state from +2 to 0 for Sb. The bulk was dispersed in TOP in order to heat up in a hot capping ligand to make nanosized Sb.

Step 1: $Sb^{3+} + BH_4^- \rightarrow Sb^0$

Step 2: Sb^0 + TOPO/OA/HDA → TOPO/OA/HDA-Sb^0

Sb nanoparticles are shown in Fig 4.1 that are TOPO capped which are spherical in shape with two distinct size ranges. The average diameter of the large particles is 10.1±2.3 nm and 3.3 ± 0.8 nm for the smaller particles. The spherical shape of the particles is typical of TOPO capped particles. TOPO adsorbs strongly on the particle surface because of its bulky nature thereby

preventing any anisotropic growth. The XRD pattern shows the particles to have a rhombohedral structure (Fig. 4.2). The crystal planes are (003), (012), (110), (104) and (202) (JCPDS 05-0562).

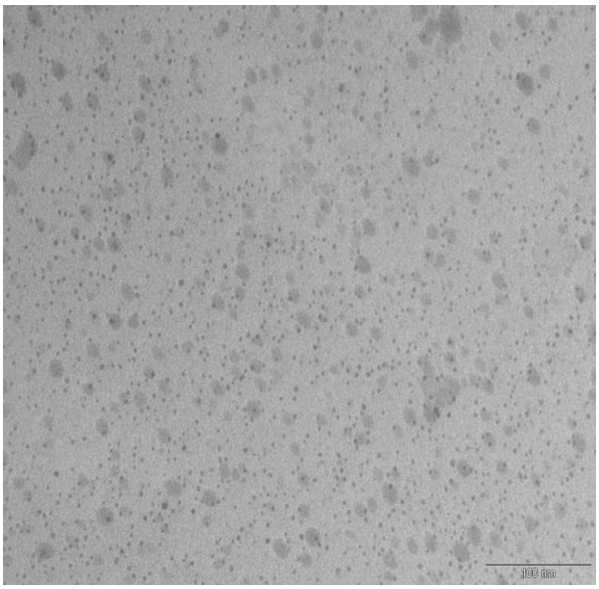

Fig. 4.1 TEM image of TOPO capped Sb nanoparticles synthesized at 190 ºC.

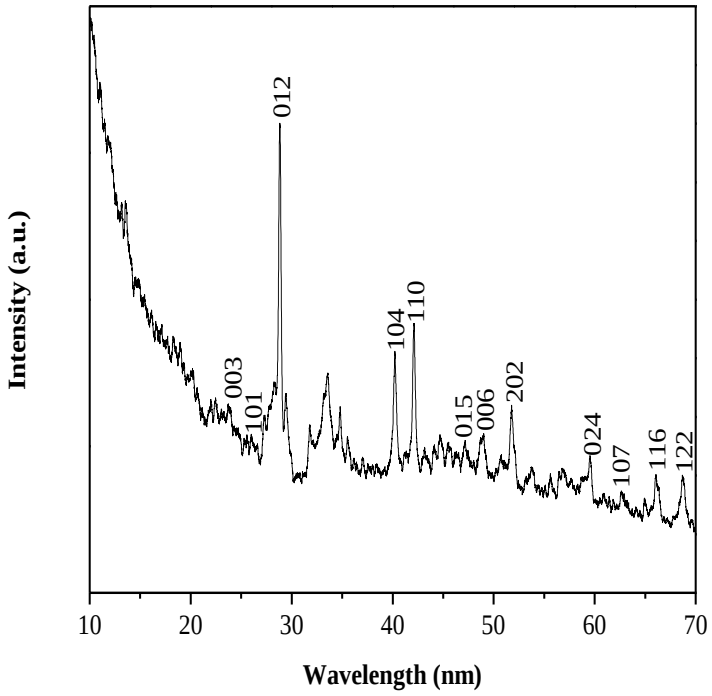

Fig. 4.2 XRD pattern of TOPO capped Sb nanoparticles

TOPO was replaced by oleylamine (OA) as the capping group as done for Bismuth in the previous chapter. The reaction temperature was also increased from 190 ºC to 230 ºC. The change of capping group to OA resulted in a change of morphology. Cubes and spherical shaped particles are visible. The particles showed some degree of self assembly with regular alignment. The cubes had an average length of 24.2 ± 1.4 nm and width of 18.3 ± 5.2 nm (Fig. 4.3). The spherical particles are smaller with an average diameter of 4.6 ± 1.6 nm. The XRD pattern is similar to the TOPO capped Sb particles with the rhombohedral structure prevalent (Fig. 4.4). The (012), (110) and (104) are diffraction peaks corresponding to the rhombohedral crystal structure (JCPDS 05-0562).

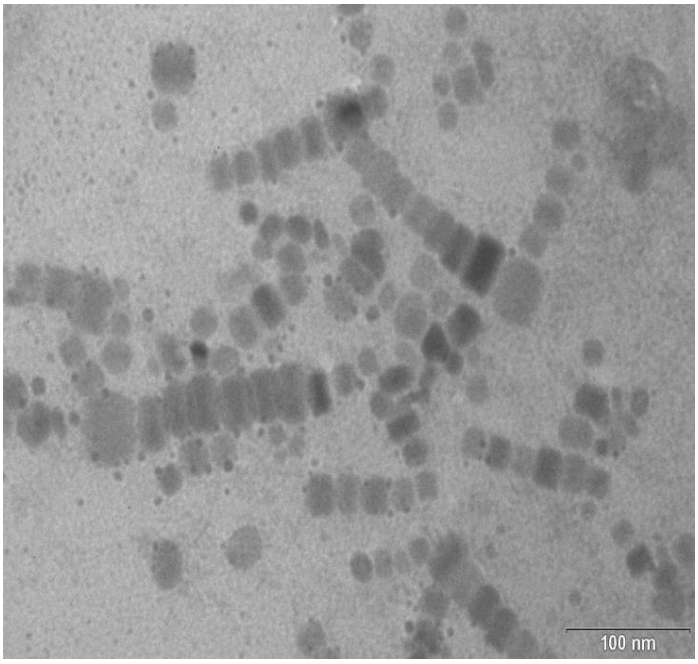

Fig. 4.3 TEM image of OA capped Sb nanoparticles synthesised at 230 ^{o}C.

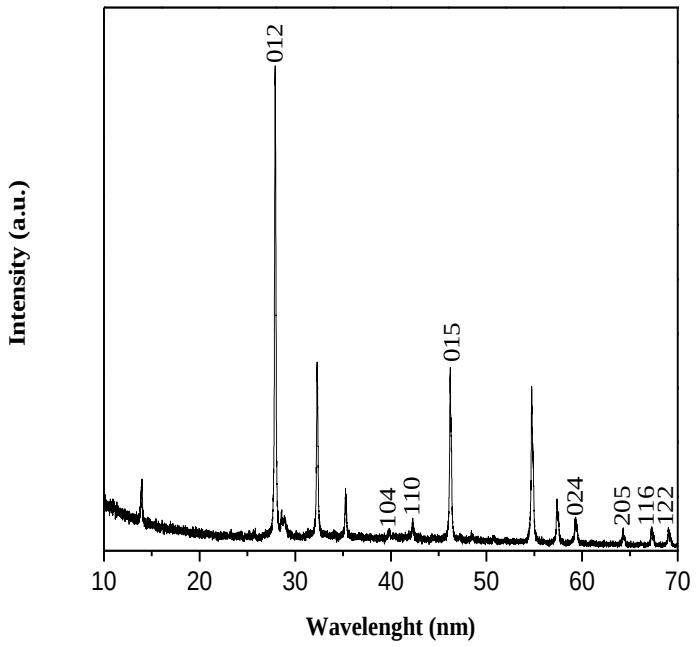

Fig. 4.4 XRD pattern of OA capped Sb nanoparticles.

4.3.2 Antimony chalcogenide nanoparticles

4.3.2.1 Sb_2S_3 nanoparticles

A similar method to bismuth chalcogenide nanoparticles was adopted for the antimony chalcogenide nanoparticle synthesis. The chalcogenide source was first reduced by sodium borohydride, followed by the addition of the antimony salt as shown below. The as formed antimony chalcogenide particles were added to tri-*n*-octylphosphine, followed by injection into a pre-heated solvent.

Step 1: $4\ NaBH_4 + 2\ E + 7\ H_2O \rightarrow 2\ NaHE + Na_2B_4O_7 + 14\ H_2$

Step 2: $NaHE + SCl_2 \rightarrow Sb_3E_2 + NaCl + HCl$

Where E = S, Se and Te

Spherical and rod shaped OA capped Sb_2S_3 nanoparticles were obtained at a reaction temperature of 230 ºC (Fig. 4.5). The average particle size was 30.4 nm with some degree of aggregation. The growth of the particles seems to be irregular with a large variation of particle size. The diffraction in the XRD can be indexed to the orthorhombic phase of Sb_2S_3 pure phase in Fig.4.6 (JCPDS 42-1393). No characteristic peaks for impurities such as antimony oxide were observed.

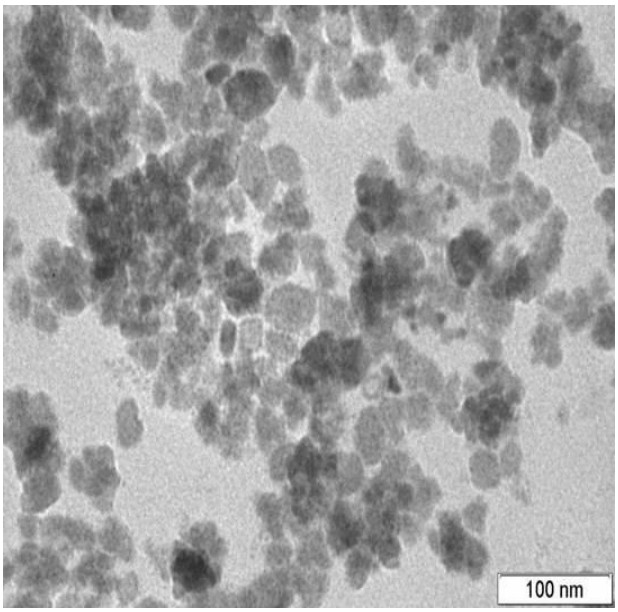

Fig. 4.5.TEM of OA capped Sb_2S_3 at 230 ^oC.

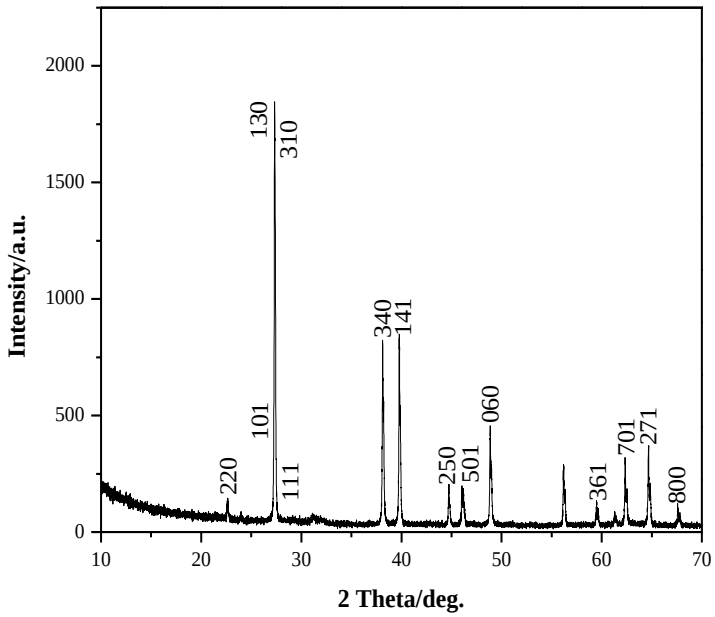

Fig. 4.6. XRD of OA capped Sb_2S_3 nanoparticles.

4.3.2.2 Sb_2Se_3 nanoparticles

The sulfur was replaced by selenium for the synthesis of Sb_2Se_3 nanoparticles. Fig. 4.7 shows elongated Sb_2Se_3 nanoparticles prepared using the two capping ligands, HDA and OA under similar reaction conditions. The alkylamine ligands allow anisotropic growth as shown in Fig. 4.7 The particle size of the HDA and OA capped could not be calculated due to the morphology of the particles which is anisotropic in nature and irregular. Fig. 4.8 shows the orthorhombic crystal structure for the OA capped Sb_2Se_3 nanoparticles (JCPDS 15-0861).

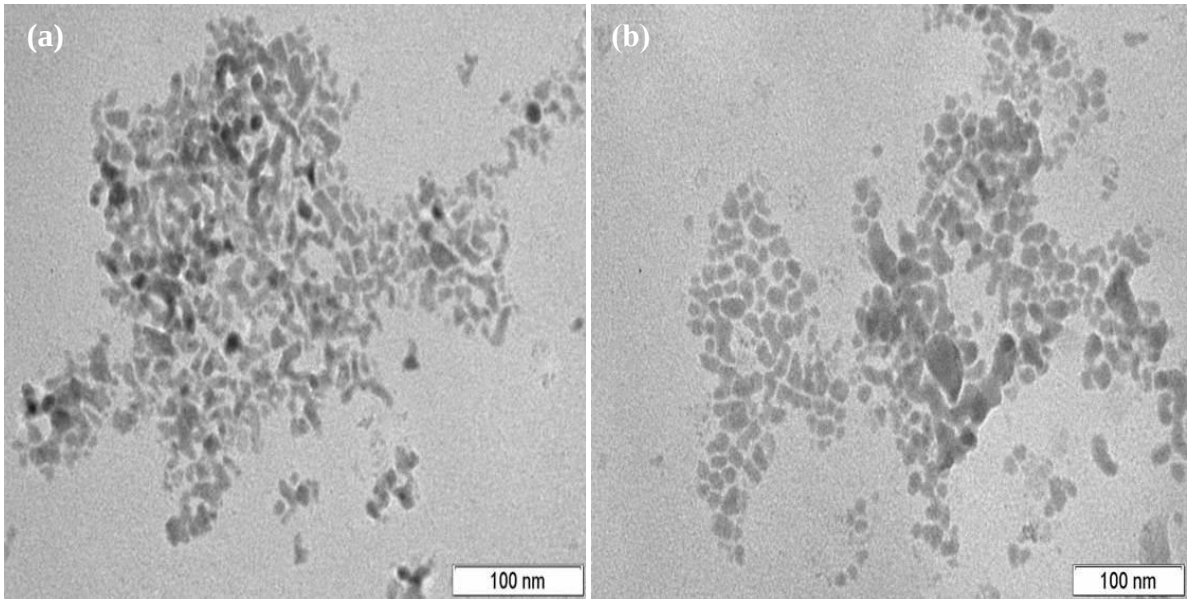

Fig. 4.7. TEM of (a) HDA capped Sb_2Se_3 nanoparticles and (b) OA capped Sb_2Se_3 nanoparticles synthesized at 230 ^{o}C.

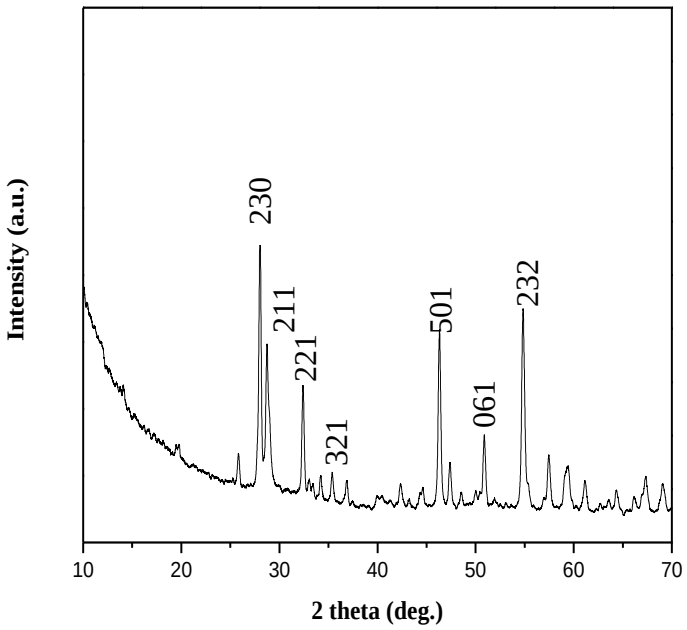

Fig. 4.8.XRD pattern of OA capped Sb_2Se_3 synthesized at 230 ^oC.

4.3.2.3 Sb_2Te_3 nanoparticles

The OA and HDA capped Sb_2Te_3 nanoparticles have a similar morphology to the Sb_2Se_3 nanoparticles. The HDA capped Sb_2Te_3 are spherical and irregular shaped (Fig. 4.9a) which made it difficult to calculate their size. The particles appear to be well dispersed on the grid. The OA capped Sb_2Te_3 nanoparticles as shown in Fig. 4.9b appear as rods with aggregation. This could be as a result of the weak binding of the ligand at this high temperature. Fig. 4.10 and 4.11 show rhombohedral structure of Sb_2Te_3 nanoparticles prepared as shown by the diffraction peaks present in the XRD (JCPDS 15-0874).

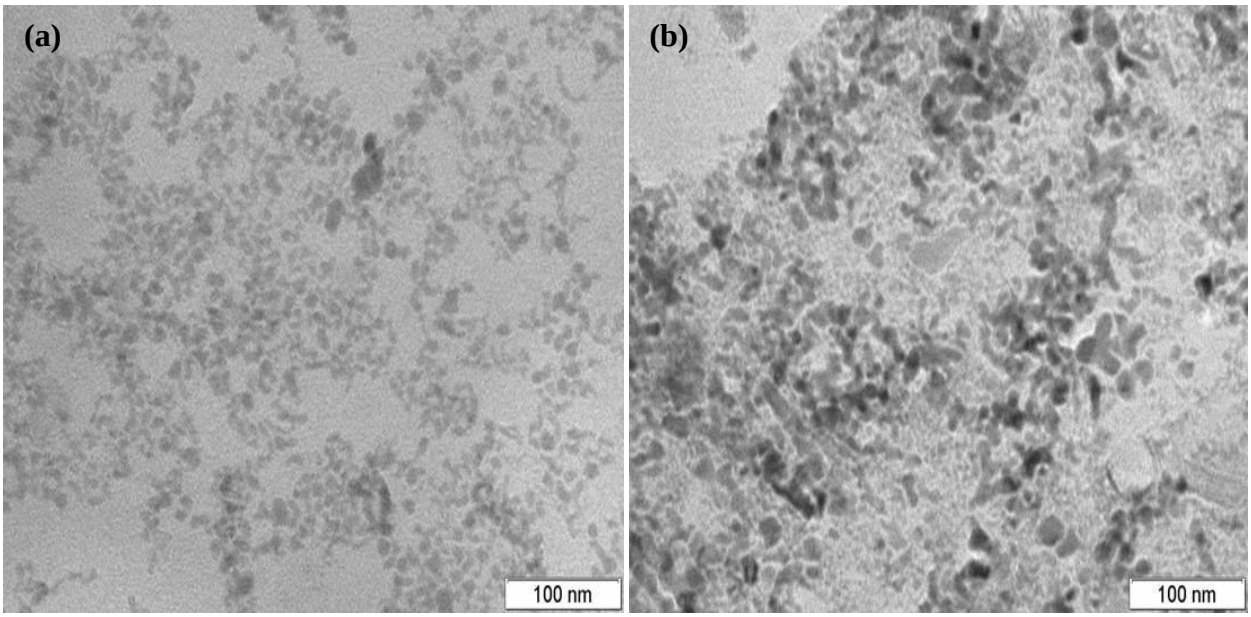

Fig. 4.9 TEM of (a) HDA capped Sb_2Te_3 and (b) OA capped Sb_2Te_3 nanoparticles synthesized at 230 ^oC.

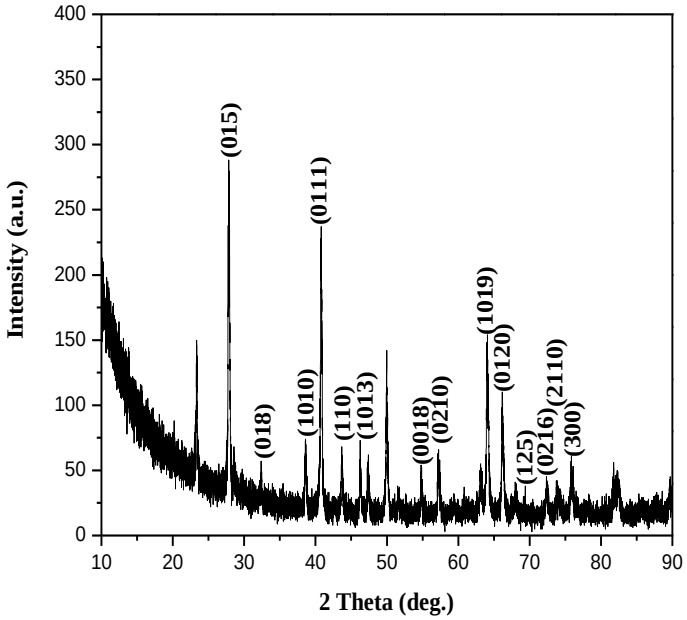

Fig. 4.10 XRD of HDA capped Sb_2Te_3 nanoparticles.

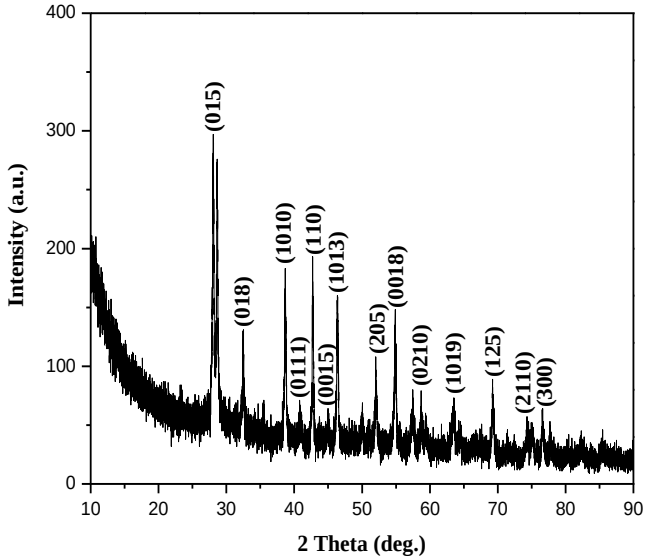

Fig. 4.11 XRD of OA capped Sb_2Te_3 nanoparticles.

4.4 Conclusions

Organically capped Sb nanoparticles were synthesized by a simple route. The TOPO capped Sb particles were spherical in shape, whereas the OA capped Sb were cubic and spherical in shape with a regular alignment on the TEM grid. The XRD pattern confirmed the rhombohedral phase. The antimony chalcogenide nanoparticles capped by HDA and OA showed similar morphology. The particles were irregular in shape with some ordered spheres also present. The XRD showed an orthorhombic phase for Sb_2S_3 and Sb_2Se_3 nanoparticles while the rhombohedral structure was observed for Sb_2Te_3 nanoparticles.

4.5 References

[1] L. R. Windmiller, *Phys. Rev*., **149** (1966) 472.

[2] H. Bryngelsson, J. Eskhult, L. Nyholm, M. Herranen, O. Alm, K. Edstrom, *Chem. Mater*., **19** (2007) 1170.

[3] H. Hu, B. Yang, Q. Li, X. Liu, W. Yu, Y. Qian, *J. Cryst. Growth*. **261** (2004) 485.

[4] P. Balaz, L. Takacs, E. Godocıkova. I. Skorvanek, J. Kovac, W. S. Choi, *J. Alloys. Comp.*, **434–435** (2007) 773.

[5] M. T. Cuberesa, B. Stegemannb, B. Kaiserb, K. Rademannb, *Ultramicroscopy*, **107** (2007) 1053.

[6] A. Houdayer, R. Schneider, D. Billaud, J. Lambert, J. Ghanbaja, *Mater. Chem. Phys*. **101** (2007) 404.

[7] A. Houdayer, R. Schneider, D. Billaud, J. Lambert, J. Ghanbaja, *Mater. Lett*. **61** (2007) 171.

[8] B. Yang, Y. Wu, H. Hu, C. Li, X. Yang, Y. Qian, *Mater. Chem. Phys*., **92** (2005) 286.

[9] A. Houdayer, R. Schneider, D. Billard, J. lambert, J. Ghanbaja, *Mater. Chem. Phys*. **101** (2007) 404.

[10] A. Houdayer, R. Schneider, D. Billaud, J. Lambert, J. Ghanbaja, *Mater. Lett*. **61** (2007) 171.

[11] S. J. Moon, Y. Itzhaik, J. H. Yum, S. M. Zakeeruddin, G. Hodes, M. Cratzel, *J. Phys. Chem. Lett*. **1** (2010) 1524.

[12] T. Zhai, M. Ye, L. Li, X. Fang, M. Liao, Y. Li, Y. Koide, Y. Bando, D. Golberg, *Adv. Mater*. **22** (2010) 4530.

[13] C. Kim, D. H. Kim, Y. S. Han, J. S. Chung, H. Kim, *J. Alloy. Compds*. **509** (2011) 609.

[14] K. W. Sun, C. Yang, T. Ko, H. Chang, C. Liu, *Pure. Appl. Chem*. **8** (2009) 1511.

[15] W. Farfan, E. Mosquera, C. Marin, *Adv. Sci. Lett*. **4** (2011) 85.

[16] A. Alemi, S. W. Joo, Y Hanifehpour, A. Khandar, A. Morsali, B. Min, *J. Nanomater*, 2011 (2011) 87.

[17] J. Kavinchan, T. Thongtem, S. Thongtem, E. Saksornchai, *J. Nanomater*, 2013 (2013).

[18] C. Kim, D. H. Kim, Y. S. Han, J. S. Chung, H. Kim, *J. Alloy. Compds*. **509** (2011) 609.

[19] K. W. Sun, C. Yang, T. Ko, H. Chang, C. Liu, *Pure. Appl. Chem*. **8** (2009) 1511.

5.1 Tin (Sn) and Tin sulfide (SnS) nanoparticles

5.1.1 Introduction

There are few studies on Sn nanoparticles due to the difficulty to accomplish their synthesis. Tin nanoparticles can be prepared by reducing bulk tin [1-5]. The melting of Sn (220-240 ^{o}C) is lower with decrease in size to the nanosize regime, whereas for bulk it is known to be 234.1 ^{o}C [4]. The enhanced or reduced surface melting is caused by the curvature effect and thickness of the liquid layer which induces a broadening of the melting temperature in smaller nanoparticles [6]. These materials show excellent antiwear properties. They can be dispersed in oil and be used as lubricating addictives. Sn is capable of accommodating Li and show high Li storage capacity than those of carbonaceous materials [3]. It is used for electrical connection in electronic devices [7]. The Sn nanoparticles deposited on cellulose fiber acts as an anode material for lithium electron batteries as they exhibit excellent electrochemical performance [2]. Hydrobenzamide-capped Sn displayed highest charge capacity and the best capacity retention on electrochemical cycling compared with citrate and polyvinyl pyrrolidone (PVP) as capping agents [3]. Other methods to synthesize Sn nanoparticles include template assisted methods [8].

Tin nanoparticles enwrapped in carbon nano-fibers (Sn/C) presented high capacity above 990 mAh g^{-1} and good cyclic performance reaching 40 cycles [9]. The highly conductive nanoparticles prepared with polyol process were used for inkjet printing [10]. Surface treaments of hydrogen reduction and plasma ashing with sintering at 250 ^{o}C diminishes the resistivity compared to bulk Sn (10.1 $\mu\Omega$ cm). The monodispersed Sn nanoparticles dispersed on graphite surface were prepared from 2,2'-bipyridine-tin(+2) chloride complex using sodium borohydride as a reducing agent. The Li insertion was evaluated using voltammetry and galvanostatic methods. The capacity was 480 mA h g^{-1} which is 37% higher than that of pure graphite based

anode. The laser ablation of tin targets was carried using UV pulse laser in ethanol which formed tin coated with tin hydroxide ($Sn(OH)_2$) and in water polycrystalline tin dioxide (SnO_2) are obtained. The size of the particles was bimodal for both the solvents used ranging between ~1 μm and ~10 nm. There was a carbon layer covering the nanoparticles that is prepared with an alcohol. The large particles synthesized in water were less regular and smoother as compared to ethanol particles [11].

Tin sulfide (SnS) is an anisotropic native p-type semiconductor with hole mobilities on the order of 90 $cm^2\ V^{-1}\ s^{-1}$ perpendicular to the *c* axis at 27 ^oC and is stable under ambient conditions [12]. This material has high absorption coefficient of *ca*.10^4 cm^{-1}. This semiconductor has received attention due to their incorporation into solar cells or photovoltaic cells. The band gap for this material is close to the optimum value required for the efficient sunlight absorption. There are several binary compounds of tin sulfide such as SnS, Sn_2S_3, Sn_3S_4, Sn_4S_5, and SnS_2. Among these tin monosulfide (SnS) and tin disulfide are the most important ones which has received much attention.

There is difficulty in the synthesis of SnS nanocrystals with a small enough size and uniform size distribution because their crystal structure is layered. An effort to explore the properties of the SnS in the nanometer scale synthetic methods has been used to prepare them. The SnS nanocrystal has been synthesized by Hickey *et al.* by the hot injection technique of thioacetamide in oleylamine into a mixture $Sn[N(SiMe_3)_2]_2$, oleic acid, trioctylphosphine and octadecene. The oleic acid/oleylamine ratio was varied to engineer the shape of the particles [13]. A simple route to synthesise SnS by injection of a solution of $S(SiMe_3)_2$ in octadecene into a solution of $SnCl_2$ in

oleylamine at 200 ^{o}C by Liu *et al.* [14]. At all temperatures the orthorhombic phase was obtained and the particle size was controlled by varying the reaction temperature. Cho and Sung [15] prepared tapered tin sulfide nanorods by tin bistrimethylsilyl amine ($Sn[N(SiMe_3)_2]_2$) dissolved in 1-octadecene (ODE). The solution was injected in tri-noctylphosphine sulfide (TOPS) and oleylamine mixture at 290 ^{0}C in which the reaction was carried for 15 s. The SnS is formed on the inside while sulfur cover the surface which changes as tin and sulfur are mixed during the process. The nanorods are a combination of the SnS and Sn-S alloy. Tin acted as both a precursor and the catalyst in this reaction as they form the tip of the rods without it at the bottom.

A study by Deng *et al*. [16] describes the synthesis of SnS nanocrystals by reacting sulfur powder (S), oleylamine (OLA) and tin (IV) iodide as precursors in hexamethyldisilazane (HMDS). These particles possess the meta-stable cubic zinc-blende phase and the more stable layered orthorhombic phase. The particles had sizes of 8 and 60 nm with spherical and polyhedral shapes. There were multi-sided particles of 700 nm with unique crystal morphology of which each nanoparticle is sixteen-facet enclosed by a 4 low-index {111} hexangular facets and 12 high-index {220} triangular facets. This was revealed by careful structural analysis using a lift-out technique with a focused ion beam (FIB) and high resolution electron microscopy imaging. Furthermore, the band gaps for the 8 nm samples was 1.68 eV, 1.65 eV for 60 nm and 1.63 eV for the 700 nm as measured by UV-Vis-NIR absorption spectroscopy.

Ning *et al*. [17] reported the synthesis of SnS nanoparticles through the reaction of a mixture of tin oxide hydroxide ($Sn_6O_4(OH)_4$) dissolved in oleic acid (OA) and oleylamine (OLA) with injection of thioacetamide/OLA solution. When the Sn/S molar ratio is 1:1 and the temperature is

150 ^{o}C, uniformly sized nanospheres are produced. But when the temperature is 120 ^{o}C and the Sn/S molar ratio is 2:1, the products were nanoflowers and nanosheets. The nanoflowers were defective and unstable with high free energy which caused their transformation into more stable amorphous nanosheets. The assumption was that the layered crystal structure of SnS is the main reason for the shape evolution and amorphization. The increase in temperature provided enough energy to overcome the barrier to amorphous. The optical properties displayed direct and indirect transitions due to quantum size effect.

Greyson *et al*. [18] formed SnS particles by thermally decomposing tin chloride and elemental sulfur in oleylamine (OLA) at 170 ^{o}C. These were tetrahedral in shape with dimensions in nanometers on one side 200-300 nm and 20 nm the other side prepared after 3 h reaction time. When the time reached 12 h, micrometer sized particles were obtained which appeared polydispersed including small particles below 100 nm. There was no change in size or shape by varying the amine surfactants as decyl-, dodecyl-, hexadecyl- and oleylamine while keeping other reaction conditions constant. By increasing the temperature to 250 ^{o}C in oleylamine for 3 h, the particles were converted from crystal structure zinc blende (ZB) tetrahedral to orthorhombic plates. There was no change in morphology or crystal structure of the particles when annealed in a tube furnace at 300 ^{o}C without any surfactant. The conclusion was that the surfactant may lower the energy needed to change phase by stabilizing an intermediate.

This chapter describes the preparation of Sn and SnS nanoparticles using the route described in the preceding chapters. The Sn and SnS nanoparticles are capped by hexadecylamine (HDA) and oleylamine (OLA).

5.2 Experimental

5.2.1 Chemicals

Tin chloride ($SnCl_2$), sulphur powder, sodium borohydride ($NaBH_4$), deionized water, methanol, tri-n-octylphosphine (TOP), hexadecylamine (HDA), oleylamine (OLA) and toluene were purchased from Aldrich. All chemicals were of analytical grade and used directly as purchased without further purification.

5.2.2 Synthesis of HDA and OLA capped Sn nanoparticles

Tin chloride (0.061 g, 0.32 mmol) was mixed with deionized water (20.0 mL) in a three- necked flask at room temperature. Sodium borohydride (0.031 g, 0.79 mmol) was carefully added to this mixture and the flask was immediately purged with nitrogen gas to create an inert atmosphere. The mixture was stirred for 2 h followed by the addition of excess methanol. The resultant solution was then centrifuged. The grey precipitate was dispersed in tri-n-octylphosphine, TOP (6.0 mL) and stirred continuously to form a TOP–Sn solution, which was then injected in to 6.0 g of HDA at 230 ^{o}C. The temperature was kept constant for 2 h. The reaction was stopped and methanol was added, resulting in the flocculation of the Sn nanoparticles. The HDA capped Sn particles were isolated after centrifugation.

The above procedure was repeated using OLA as the capping group.

5.2.3 Synthesis of HDA and OLA capped SnS nanoparticles

In a typical room temperature reaction, sulfur powder (0.041 g, 0.32 mmol) was mixed with deionised water (20.0 mL) in a three-necked flask. Sodium borohydride (0.031 g, 0.79 mmol) was carefully added to this mixture and the flask was immediately purged with nitrogen gas to

create an inert atmosphere. After 2 h, $SnCl_2$ (0.061 g; 0.32 mmol) was dissolved in deionised water (20.0 mL) and added to the light yellow coloured NaHS solution. The solution was stirred for 30 min followed by the addition of excess methanol. The resultant solution was then centrifuged. The SnS produced was dispersed in tri-*n*-octylphosphine, TOP (6 mL) and stirred continuously to form a TOP–SnS solution, which was then injected into hot HDA (6 g) at 230 ^oC. A sudden decrease in temperature was observed. The temperature was kept constant at 230 ^oC for 30 minutes. After the reaction time an immediate addition of methanol resulted in the reversible flocculation of the SnS nanoparticles. The flocculate was separated from the supernatant by centrifugation. The resultant particles were dissolved in toluene to give an optically clear solution of HDA capped SnS nanocrystallites for characterization. OA replaced HDA in another reaction under similar conditions which is due to the nature of the reaction parameters under study.

5.3 Results and discussion

5.3.1 HDA and OLA capped Sn nanoparticles

The particles were prepared by $SnCl_2$ reduction for 2 h to form bulk tin. These metal particles are then mixed with TOP and alkylamines such as HDA or OA at 230 ^oC for 2 h in step 1 and 2.

Step 1: $Sn^{2+} + BH_4^- \rightarrow Sn^0$

Step 2: Sn^0 + OA/HDA → OA/HDA-Sn

The TEM image in Fig. 5.1(a) shows HDA capped Sn nanoparticles. There is evidence of some degree of aggregation. There are spherical aggregated particles and their size could not be

calculated due to the extent of aggregation. OA capped Sn nanoparticles are shown in Fig 5.1(b). The OA capped Sn nanoparticles have rod-like morphology with aggregation making it difficult to determine the exact particle size. The sample prepared using HDA for tin nanoparticles were analysed using XRD which have broad peaks characteristic of the nanosize nature of these particles in Fig. 5.2. The peaks at 2θ values of 30.82^{o}, 32.21^{o}, 44.04^{o}, 45.02^{o}, and 55.47^{o} are assigned to the (200), (101), (220), (211) and (301) planes of the tetragonal phase of tin (JCPDS 86-2264), respectively. These results are similar to the bulk phase of tin particles.

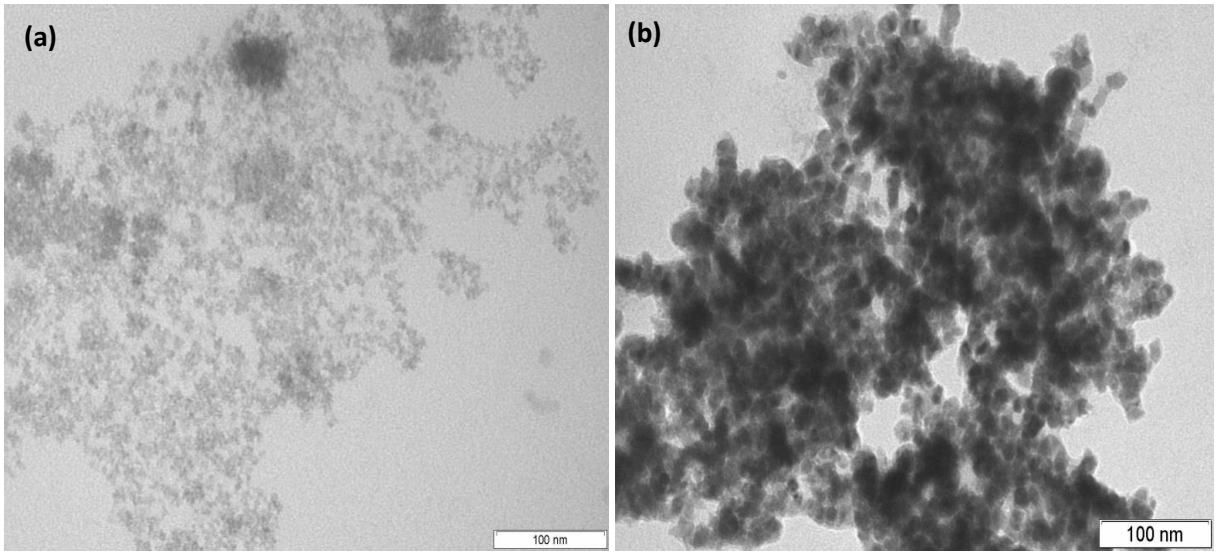

Fig. 5.1 TEM images of (a) HDA capped Sn and (b) OA capped Sn at 230 ^{o}C for 2 h.

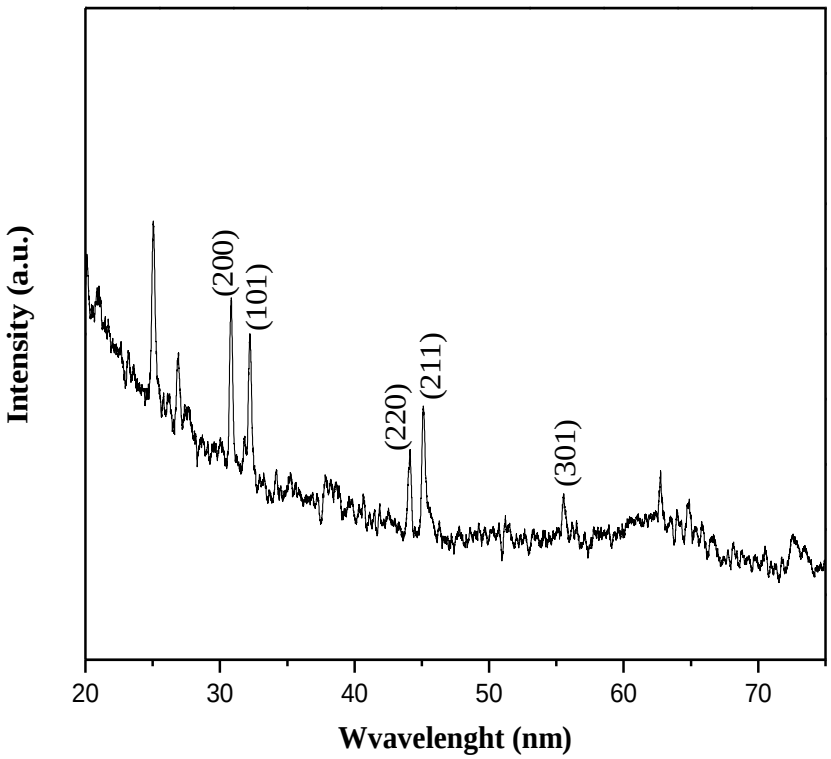

Fig. 5.2 The XRD pattern of HDA capped tin nanoparticles synthesized at 190 ^{o}C during 2 h reaction time.

5.3.2 HDA and OLA capped SnS nanoparticles

The TEM images in Fig. 5.3. (a)-(c) show OLA capped SnS nanoparticles prepared when the reaction time varies from 30 min, 1 h and 2 h. Most of the particles during the 30 minutes growth time seem spherical with an average particle size of 32.7 ± 10.3 nm. There was an occurrence of elongated polydispersed particles. Some appear aggregated due to the appearance of dark spots with some clear shaped particles. With the increase in reaction time to 1 h, the average size was reduced to 20.1 ± 6.9 nm. This is contrary to what was expected during synthesis which is due to the breaking down of large particles to small particles influenced by surface energy. There are some triangular shaped particles that start to appear at this stage with elongated ones also

present. The reaction progressed after 2 h time to yield average particles size of 12.8 ± 4.5 nm which appear more uniformly. There have been previous reports of the synthesis of SnS rectangular nanosheets [19]. It appears that the reaction conditions favour the formation of large SnS particles which breakdown into smaller particles as the reaction time proceeds. The formation of these larger particles with sheet-like morphology may be thermodynamically favoured early in the reaction.

The same conditions were used to prepare HDA capped SnS nanoparticles as shown in Fig.5.3(d). The particles are well dispersed with the shape of spherical and elongated to some extent, with aggregation of the materials also evident making size determination difficult. The XRD for the HDA capped SnS nanoparticles prepared at 230 ^{o}C is shown in Fig. 5.4. The diffraction peaks are broadened due to poor crystallinity and nanosize nature of the nanoparticle. There are however some peaks which can be assigned to the orthorhombic phase..

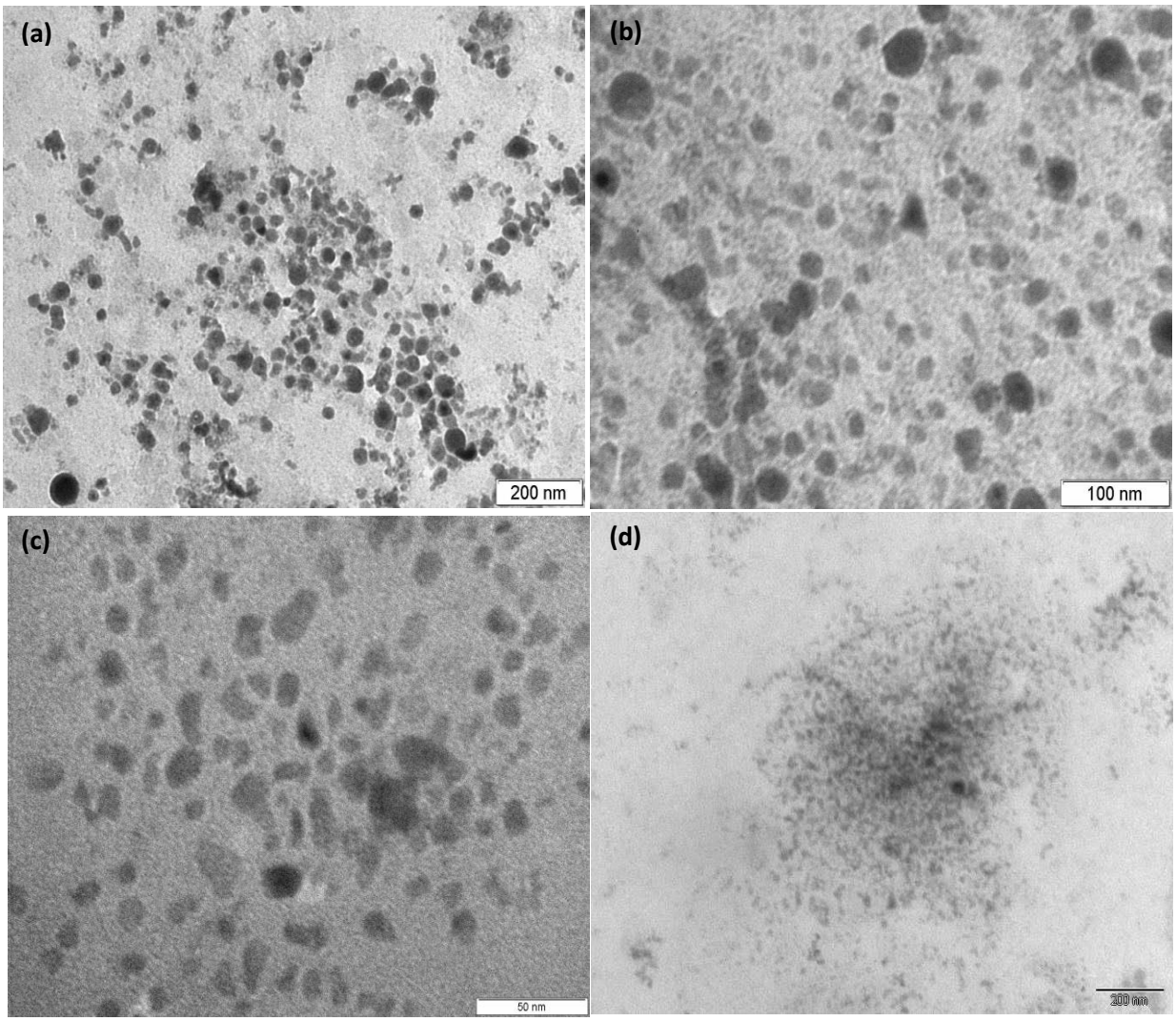

Fig. 5.3 TEM images of OLA capped SnS nanoparticles at 230 ^{o}C after (a) 30 min, (b) 1 h, (c) 2 h, (d) HDA capped Sn nanoparticles after 2 h.

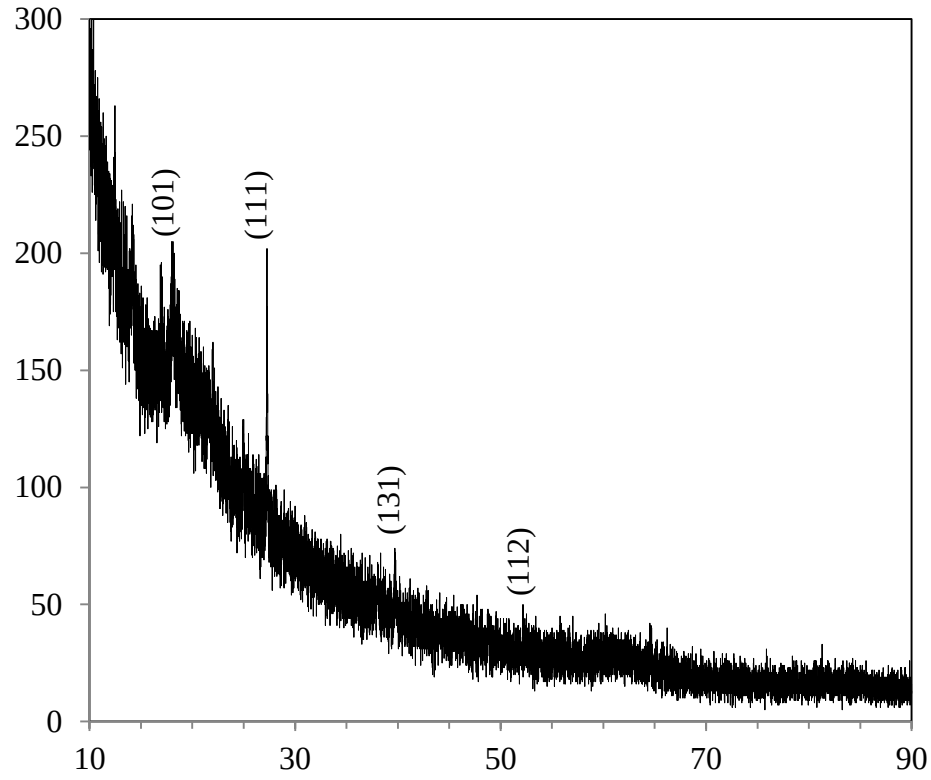

Fig. 5.4 XRD spectra of HDA capped SnS prepared at 230 ^{o}C.

5.4 Conclusion

HDA and OLA capped Sn nanoparticles have been synthesized. Both the HDA and OLA capped Sn nanoparticles show some degree of agglomeration in the TEM images making size determination difficult. The XRD pattern of the HDA capped Sn shows diffraction peaks which could be assigned to tetragonal phase of Sn. The HDA and OLA were also used to cap SnS nanoparticles. Spherical particles of SnS were obtained using both capping groups. The OLA capped SnS particles synthesized at 230 °C had an average particle size of 32.7 nm after 30 minutes growth time, 20.10 nm after 1 h and 12.80 nm after 2 h. The HDA capped SnS nanoparticles were predominantly orthorhombic.

5.5 References

[1] Y. Zhao, Z. Zhang, H. Dang, *Mater. Sci. Eng*. A **359** (2003) 405.

[2] A. Caballero, J. Morales, L. Sanchez, *Electrochemical and Solid-State Letters*, **8** (9) (2005) A464.

[3] M. G. Kim, Y. Kim, Y. Lee, J. Cho, *Electrochemical and Solid-State Letters*, **9** (1) (2006) A34.

[4] H. Jiang, K. Moon, H. Dong, F. Hua, C. P. Wong, *Chem. Phys. Lett*. **429** (2006) 492.

[5] Z. Li, X. Tao, Y. Cheng, Z. Wu, Z. Zhang, H. Dang, *Ultrasonics Sonochemistry*. **14** (2007) 89.

[6] Y. H. Jo, I. Jung, C. S. Choi, I. Kim, H. M. Lee, *Nanotechnology*, **22** (2011) 225701.

[7] Z. Chang-dong, G. Yu-lai, Y. Bin, Z. Qi-jie, *Trans. Nonferrous. Met. Soc. China*, **20** (2010) 248.

[8] H. H. An, J. H. Kim, S. J. Lee, W. B. Han, J. H. Lee, H. Kim, S. H. Suh, I. T. Yoon, Y. Shon, C. S. Yoon, *Applied. Surface. Science*. **257** (2011) 8702.

[9] H. Wang, P. Gao, S. Lu, H. Liu, G. Yang, J. Pinto, X. Jiang, *Electrochimica. Acta*, **58** (2011) 44.

[10] Y. H. Jo, I. Jung, C. S. Choi, I. Kim, H. M. Lee, *Nanotechnology*, **22** (2011) 225701.

[11] O. R. Musaev, M. S. Driver, E. A. Sutter, A. N. Caruso, J. M. Wrobel, M. B. Kruger, *Appl. Phys. A.*, **113** (2013) 355.

[12] W. Albers, C. Haas, H. J. Vink, J. D. Wasscher, *J. Appl. Phys*., **32** (1961), 2220.

[13]S. G. Hickey, C. Waurisch, B. Rellinghaus, A. Eychmuller, *J. Am. Chem Soc.* **130** (2008) 14978.

[14]H. T. Liu, Y. Liu, Z. Wang, P. He. *Nanotechnology*, **21** (2010) 105707.

[15] K. Cho, Y. Sung, *Nanoscale*. (2013) 4162.

[16] Z. Deng, D. Han, Y. Liu, *Nanoscale*, **3** (2011) 4346.

[17] J. Ning, K. Men, G. Xiao, L. Wang, Q. Dai, B. Zou, B. Liu, G. Zou, *Nanoscale*. **2** (2010) 1699.

[18] E. C. Greyson, J. E. Barton, T. W. Odom, *Small*. **2** (2006) 368.

[19] Y. Zhang, J. Lu, S. Shen, H. Xu, Q. Wang, *Chem. Commun*, **47** (2011) 5226.

6.0 ZnTe nanoparticles

6.1 Introduction

The synthesis of semiconductor nanoparticles such as cadmium chalcogenides is a major focus of research in nanomaterials synthesis [1–3]. However, the toxicity of cadmium has been a drawback which has compelled researchers to look at less toxic materials such as zinc chalcogenides [4]. Among the zinc chalcogenides, ZnTe, is an attractive semiconductor for various applications in optoelectronic and thermoelectric devices [5,6]. However, when compared with the sulphur and selenide zinc analogs there are fewer reports on the preparation of ZnTe nanocrystals. Some routes for the synthesis of ZnTe nanoparticles include the solvothermal process [7], pulsed laser ablation [8], mechanical milling [9] and microwave plasma routes [10]. Jun *et al*. reported the use of a monomeric molecular precursor, $[Zn(TePh)_2][TMEDA]$ for the 'one pot' synthesis of dodecylamine capped ZnTe nanoparticles [11]. The size and shape of the nanoparticles were controlled by temperature and the capping ligands. The synthesis of wurtzite nanorods with controllable aspect ratios was reported [12]. The dimensions of the particles were controlled by adopting active polytellurides as the tellurium precursor in conjunction with variation of the precursor concentration, reaction temperature and/or reaction time. The synthesis of HDA capped ZnTe nanoparticles using a hybrid solution based thermolysis method is reported. The work is a follow up on previous work by the Revaprasadu group on CdTe and PbTe nanoparticles [13,14].

6.2 Experimental

6.2.1 Synthesis of HDA capped ZnTe nanoparticles

Tellurium powder (0.041 g, 0.32 mmol) was mixed with deionised water (10.0 mL) in a three-necked flask. A 10.0 mL aqeoues solution of sodium borohydride (0.031 g, 0.79 mmol) was carefully added to this mixture and the flask was immediately purged with nitrogen gas to create an inert atmosphere. After 2 h, 20.0 mL aqueous solution of $ZnCl_2$ (0.0436 g, 0.32 mmol) was added to the light pink coloured NaHTe solution. The solution was stirred for 30 min followed by the addition of excess methanol. The resultant solution was then centrifuged. The ZnTe produced was dispersed in tri-n-octylphosphine, TOP (6.0 mL) and stirred continuously to form a TOP–ZnTe solution, which was then injected into hot hexadecylamine (6.0 g) 23 or 270 ^{o}C. A sudden decrease in temperature was observed between. The temperature was kept constant at the reaction temperature for 2 h. An immediate addition of methanol resulted in the reversible flocculation of the nanoparticles. The flocculate was separated from the supernatant by centrifugation. The resultant particles were dissolved in toluene.

6.2.2 Synthesis of Cysteine and TEA capped ZnTe nanoparticles

Tellurium powder (0.041 g, 0.32 mmol) was mixed with deionised water (10.0 mL) in a three-necked flask. 10.0 mL aqueous solution of sodium borohydride (0.031 g, 0.79 mmol) was carefully added to this mixture and the flask was immediately purged with nitrogen gas to create an inert atmosphere. After 2 h, 20.0 mL aqueous solution of $ZnCl_2$ (0.0436 g, 0.32 mmol) and 20.0 mL of L-cysteine ethyl ester hydrochloride solution (1.1883 g, 6.40 mmol) with a molar ratio of 1:20 (Cd^{2+}: cysteine ester) was added simultaneously to the pink tellurium ion solution. The pH of the solution was raised to 7 by using HCl (0.10 M) and NH_3 (0.10 M) solutions after

which the solution was then heated at 100 ^{o}C for 3 h. After completion of the reaction, excess methanol was added resulting in the reversible flocculation of the nanoparticles. The flocculate was separated from the supernatant by centrifugation. The resultant particles were dissolved in acetone for characterization.

The reaction procedure described above was carried for the TEA-capped ZnTe nanoparticles with TEA (0.9548 g, 6.40 mmol) replacing the L-cysteine ethyl ester hydrochloride.

6.3 Results and discussion

6.3.1 Organically soluble ZnTe nanoparticles

We have synthesized ZnTe nanoparticles at 230 °C and 270 °C using the method previously described for CdTe and PbTe [13,14]. The reaction temperatures were chosen as the optimum temperature based on our previous work with the cadmium and lead telluride systems. The synthesis method involves the reduction of tellurium powder using sodium borohydride ($NaBH_4$) as the reducing reagent to give an oxygen free tellurium ion (NaHTe) followed by the addition of an aqueous solution of zinc chloride. The sequence of reactions is shown in Step. 1 and 2:

Step 1: $4\ NaBH_4 + 2\ Te + 7\ H_2O \rightarrow 2\ NaHTe + Na_2B_4O_7 + 14\ H_2$

Step 2: $NaHTe + ZnCl_2 \rightarrow ZnTe + NaCl + HCl$

The resultant ZnTe particles were isolated by centrifugation then dispersed in tri-n-octylphosphine (TOP) and injected into hot hexadecylamine (HDA) which serves as a

coordinating solvent. HDA is a primary amine with less steric hinderance creating a large capping density as a result of its small stereochemical interference [15,16].

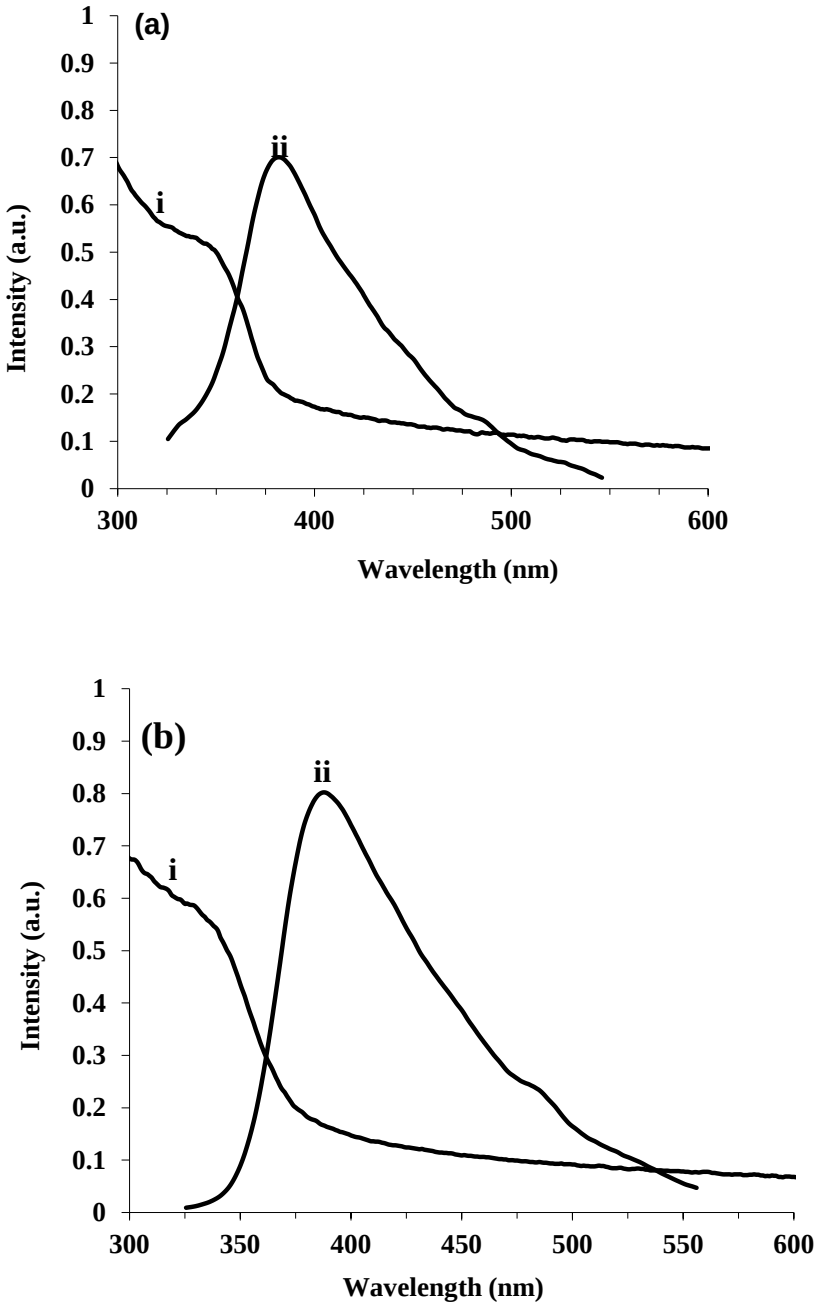

Fig. 6.1. Absorption (i) and emission spectra (ii) for HDA capped ZnTe nanoparticles at (a) 230 and (b) 270 °C.

The absorption spectra for the samples obtained at both reaction temperatures show distinguishable absorption peaks. The absorption spectrum (Fig. 6.1a(i)) of the HDA capped ZnTe nanoparticles synthesized at 230 °C shows a relatively sharp band edge located at 338 nm (3.67 eV), a blue shift of 110 nm in relation to bulk ZnTe (548 nm). The corresponding photoluminescence spectrum shows an emission curve with the maximum at 384 nm and a full width at half maxima (FWHM) of 81 nm (Fig. 6.1a(ii)). An increase in reaction temperature to 270 °C did not have a significant effect on the optical data. The absorption band edge was observed at 385 nm and the corresponding emission maximum was at 388 nm (Fig. 6.1b). The slight increase in particle size is consistent with the increase in temperature. There are few reports of luminescence reported for ZnTe. In this work, the shape of the absorption spectrum and width of the emission curve for both samples synthesized at both temperatures is in good agreement with previous reports on luminescent ZnTe [11]. The position of the emission maxima is in contrast to previous reports which reported the emission maxima in the 400–600 nm region [11,17]. The enhanced blue shift in the emission maxima is due to the presence of smaller sized particles compared to the emission from rod shaped particles.

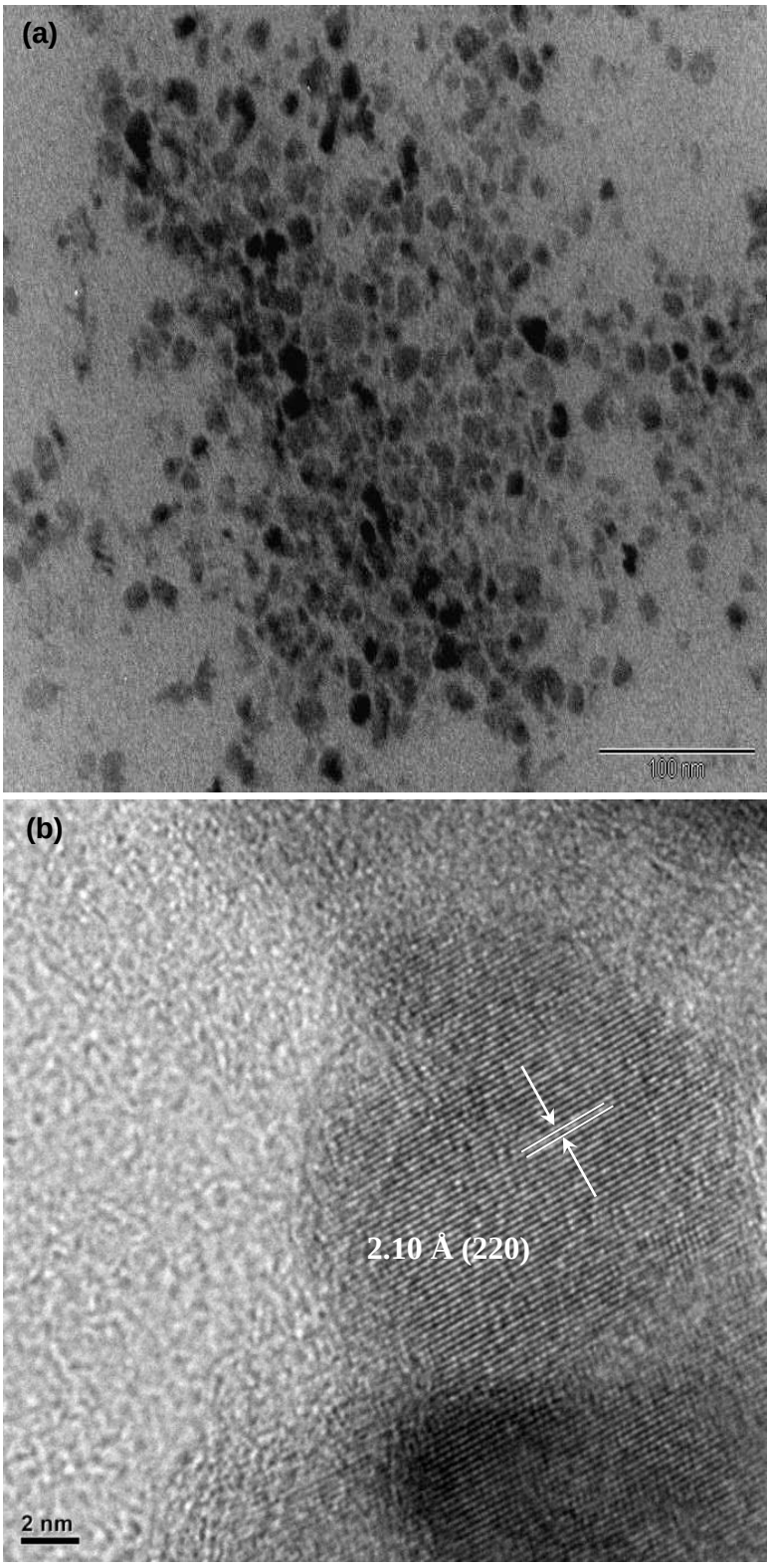

Fig. 6.2.(a) TEM and (b) HRTEM images for HDA capped ZnTe nanoparticles at 230 °C.

Fig. 6.2a show the TEM image of HDA capped ZnTe nanoparticles synthesized at 230 °C. The ZnTe particles appear close to spherical aggregated with an average particles size of 10.22 ± 3.39 nm. The corresponding high resolution transmission electron microscopy (HRTEM) image (Fig. 6.2b) shows a well defined particle with distinct lattice fringes. The lattice spacing of 2.10 Å matches the (220) plane of the cubic structure of ZnTe. The TEM image of the particles synthesized at 270 °C shows well defined, spherical particles with an average size of 10.18±1.20 nm (Fig. 6.3a). The HRTEM image (Fig. 6.3b) shows a single particle with lattice fringes. There are no defects or discontinuities in the lattice fringes suggesting that growth occurs via the Ostwald ripening process. The capping group, HDA selectively adsorbs onto the crystal planes in a dynamic manner allowing for particle growth to occur [18]. Our previous work on CdTe shows that growth via an oriented attachment mechanism can also occur under certain reaction conditions resulting in anisotropic particles [13]. We did not observe any anisotropic particles at the higher temperature.

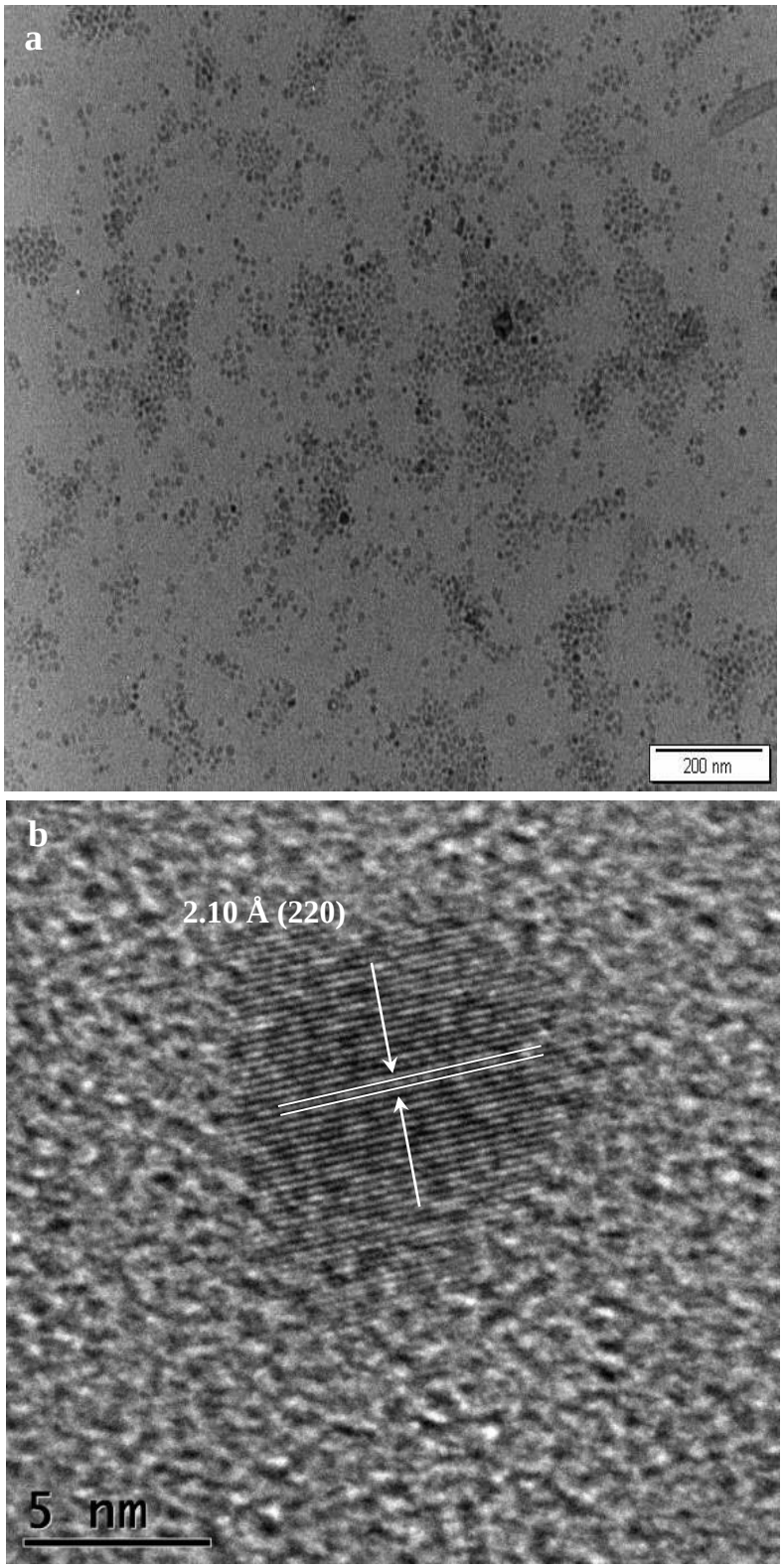

Fig. 6.3.(a) TEM and (b) HRTEM images for HDA capped ZnTe nanoparticles at 270 °C.

The X-ray diffraction (XRD) pattern of the ZnTe nanoparticles synthesized at 230 °C is shown in Fig. 6.4. The broadened diffraction peaks correspond to the cubic zinc-blend structure of ZnTe. The zinc blende structure of ZnTe is the most common phase with only a few reports of the wurtzite phase [11,19]. No peaks due to impurities such as Zn or Te were observed.

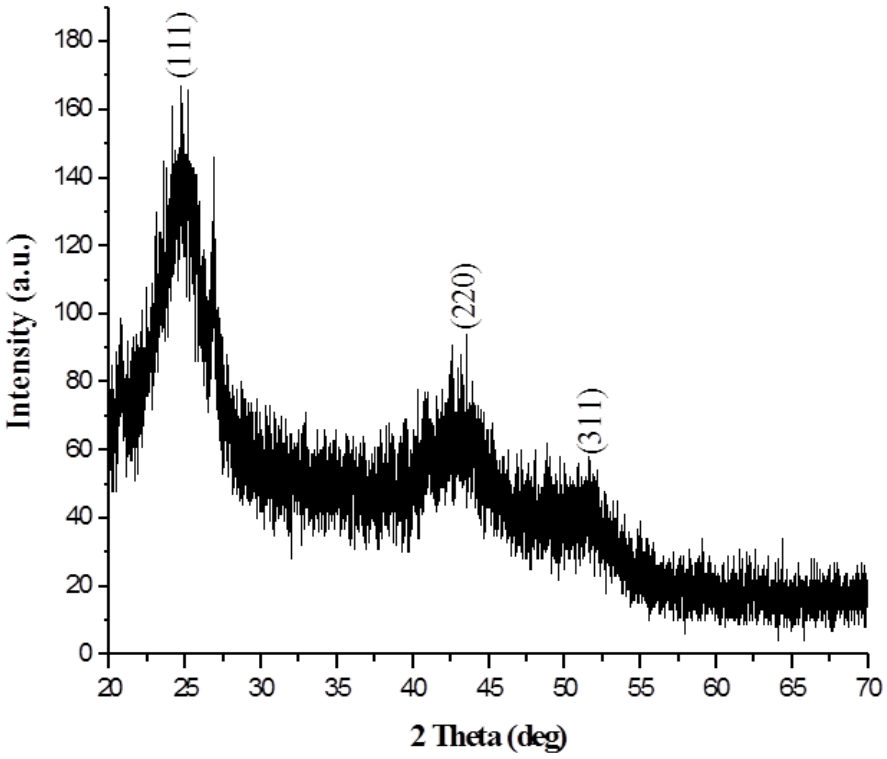

Fig. 6.4. Powder X-ray diffraction of HDA-capped ZnTe nanoparticles after 2 h reflux time at 230 ^{o}C.

6.3.2 Water soluble ZnTe nanoparticles

In Fig. 6.5, water soluble ZnTe nanoparticles are synthesized using TEA (a) and cysteine (b) where rods and quasi-spherical shaped aggregated particles are observed, respectively. These particles are not very clear because they are aggregated to the inadequate presence of the capping ligand. This affects the surface energy of the nanoparticles to increase the energy related to the surface forces in the ligand sphere. The nanorods have been observed before by Wan *et al*. [20]. They obtained nanorods of ZnTe with widths of 150-300 nm and lengths of several micrometers. They were prepared in hydrazine hydrate at low temperatures of 80 ^{o}C which were annealed to 480- 520 ^{o}C.

The XRD patterns showed weak diffractive peaks which were difficult to assign.

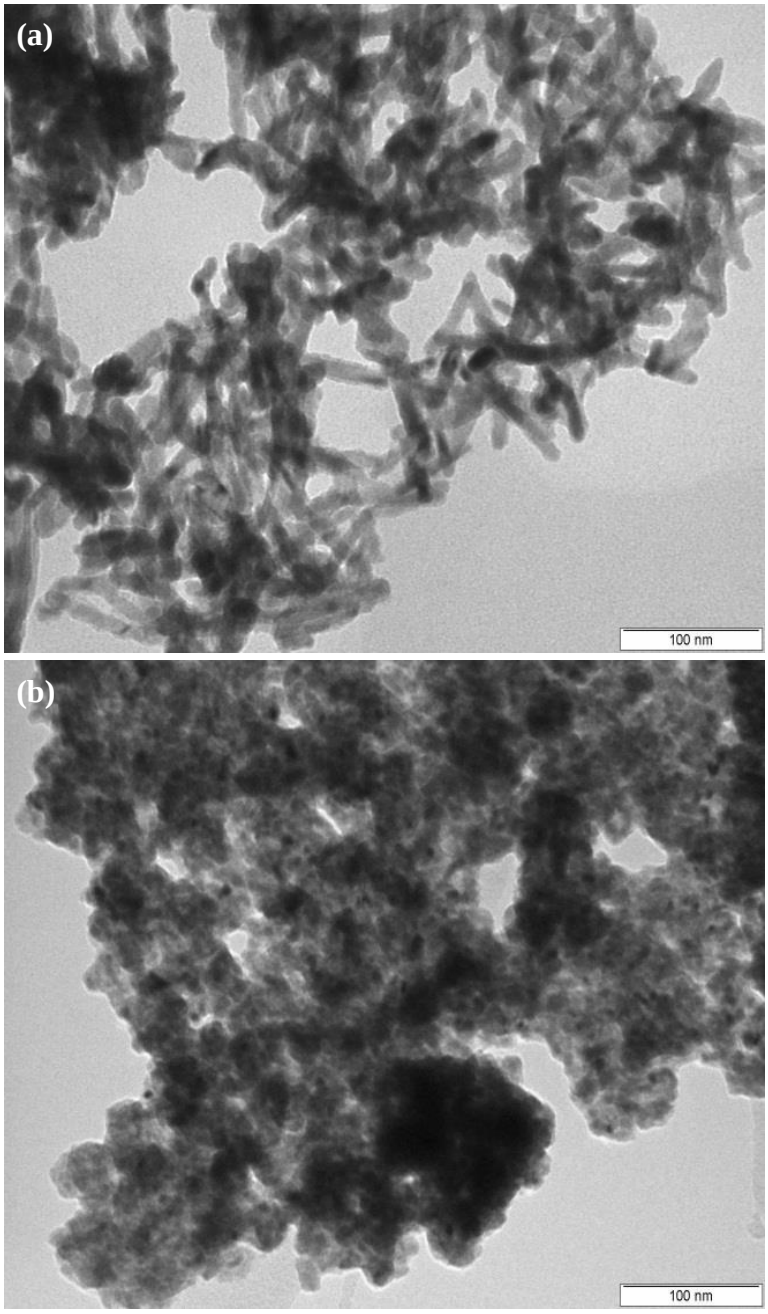

Fig. 6.5 TEM of (a) TEA and (b) Cys capped ZnTe nanoparticles synthesized at pH 7 after 2 h reflux time.

6.4 Conclusion

In summary, we have synthesized HDA capped ZnTe nanoparticles via a facile hybrid route. The band gap is blue shifted from the bulk material, with the emission maxima also in the blue region, consistent with their reduced size. The reaction carried out at different temperatures produced spherical or nearly spherical particles with a cubic phase. The electron microscopy results confirm the crystalline nature of the particles. For the water soluble ZnTe, the TEA capped particles gave nanorods whereas the cysteine capped particles were quasi-spherical in shape. Both the capping groups gave particles which were aggregated due to their poor capping.

6.5 References

[1] S. Baskoutas, A. F. Terzis, *J. Appl. Phys*. **99** (2006) 013708.

[2] S. D. Bunge, K. M. Krueger, T. J. Boyle, M. A. Rodriguez, T. J. Headley, V. L. Colvin, *J. Mater. Chem*. **13** (2003) 1705.

[3] N. Li, X. Zhang, S. Chen, X. Hou, Y. Liu, X. Zhai, *Mater. Sci. Eng. B***176** (2011) 688.

[4] K. G. Li, J. T. Chen, S. S. Bai, X. Wen, S. Y. Song, Q. Yu, *Toxicol in vitro*, **23** (2009) 1007.

[5] D. W. Kisker, *J. Cryst. Grwth*. **98** (1989) 127.

[6] W. S. Kuhn, B. Qu'Hen, O. Gorochov, R. Triboulet, W. Gebhardt, *Prog. Cryst. Growth. Charact. Mater*. **31** (1995) 45.

[7] Y. Li, Y. Ding, Z. Wang, *Adv. Mater*. **11** (1999) 847.

[8] T. Orii, M. Hirasawa, T. Seto, *J. Phys: Conf. Ser,* **59** (2007) 716.

[9] S. Patra, S. K. Pradhan, *J. Alloys. Cmpd*. **509** (2011) 5567.

[10] T. Suriwong, S. Thongtem, T. Thongtem, *Mater. Lett*. **63** (2009) 2103.

[11] Y. Jun, C. Choi, J. Cheon. *Chem. Commun*. (2001) 101.

[12] J. Zhang, S. Jin, H. C. Fry, S. Peng, E. Shevchenko, G. P. Wiederrecht, *J. Am. Chem. Soc*. **133** (2011) 15324.

[13] N. Mntungwa, V. S. R. Rajasekhar Pullabhotla, N. Revaprasadu, *J. Mater. Chem. Phys*. **126** (2011) 500.

[14] N. Ziqubu, K. Ramamsy, V. S. R. Rajasekhar Pullabhotla, N. Revaprasadu, P. O'Brien, *Chem. Mater*. **22** (2010) 3817.

[15] D. V. Talapin, A. L. Rogach, A. Kornowski, M. Haase, H. Weller, *Nano. Lett*. **1** (2001) 207.

[16] L. Qu, X. Peng, *J. Am. Chem. Soc*. **124** (2002) 2049.

[17] S. H. Lee, Y. J. Kim, J. Park, *Chem. Mater*. **19** (2007) 4607.

[18] X. Peng, *Nano. Res*. **2** (2009) 425.

[19] S. Xu, C. Wang, Q. Xu, H. Zhang, R. Li, H. Shao, *Chem. Mater*. **22** (2010) 5839.

[20] B. Wan, C. Hu, B. Feng, J. Xu, Y. Zhang,Y. Tian, *Mater. Sci. Eng. B***171** (2010) 11.

7.0 CdTe nanoparticles

7.1 Introduction

Water soluble semiconductor nanoparticles have been extensively studied because of their biological applications [1-3]. Semiconductor nanoparticles possess unique properties such as tunable emission and absorption wavelengths, sharp emission spectra, resistance to chemical degradation, photobleaching and versatility in surface modifications. There are two main approaches for the synthesis of water soluble nanoparticles. The first approach is to replace the organically soluble surface-capping molecules on the particles with water-soluble thiols or a silica shell [4, 5-6]. The substitution of the surface capping molecule by hydrophilic molecules can result in a decrease in photoluminescence [7, 8]. The second approach is to directly synthesize the nanoparticles in an aqueous solution using water-soluble stabilizers such as thiols [7, 9]. This method is inexpensive, simpler, less toxic and yields particles that exhibit higher quantum yields.

Cadmium telluride (CdTe) is an example of a semiconductor that can be stabilized by both organic and water soluble molecules. Highly luminescent water-soluble CdTe nanoparticles have found use in finger print detection [10], light-emitting devices (LEDs) [11], solar cells [12] and biological labelling [13]. Thioglycerol and mercaptoethanol were initially used as ligands for the synthesis of water soluble CdTe [14]. Subsequently various other thiol based ligands have also been used for the passivation of CdTe nanoparticles. [9,15,16]. Weller and co-workers [9] explored the effects of thiol ligands such as mercapto acids, mercapto alcohols, and mercapto amines on the preparation of CdTe in the aqueous phase. Zou *et al*. [15] reported a facile aqueous phase route to prepare high-quality nanocrystalline CdTe with mercaptopropionic acid

as the capping agent. El-Sadek *et al*. [16] synthesized water-soluble CdTe nanoparticles in aqueous solution with the assistance of mercaptoacetic acid (MAA) molecules by a wet chemical route method. The synthesis of CdTe nanoparticles in L-cysteine has been reported by a few groups [17, 18]. By varying the Cd/Te ratio highly luminescent nanoparticles and nanorods were formed [18].

Recently our group has developed a new, relatively safe and inexpensive route to water soluble CdSe [19, 20, 21]. The route involves the reduction of selenium by sodium borohydride forming sodium hydrogen selenide followed by the addition of the metal salt and capping group such as cysteine, triethanoamine (TEA) or ascorbic acid under controlled reaction conditions.

In this chapter the synthesis of cysteine and TEA capped CdTe nanoparticles using the reduction method described above is reported. The cadmium salts were varied to study their effect on the optical properties and morphology.

7.2 Experimental

7.2.1. Chemicals

Tellurium powder, sodium borohydride ($NaBH_4$), deionised water, cadmium chloride, cadmium acetate, cadmium carbonate, cadmium nitrate, methanol, acetone, L-cysteine ethyl ester hydrochloride and triethanolamine (TEA) were purchased from Aldrich. All chemicals were of analytical grade and used directly as purchased without further purification.

7.2.2 Synthesis of Cysteine and TEA capped CdTe nanoparticles

In a typical room temperature reaction, tellurium powder (0.041 g, 0.32 mmol) was mixed with deionised water (10.0 mL) in a three-necked flask. 10.0 mL aqueous solution of sodium borohydride (0.031 g, 0.79 mmol) was carefully added to this mixture and the flask was immediately purged with nitrogen gas to create an inert atmosphere. After 2 h, 20.0 mL aqueous solution of $CdCl_2$ (0.059 g; 0.32 mmol) and 20.0 mL of L-cysteine ethyl ester hydrochloride solution (1.1883 g, 6.40 mmol) with a molar ratio of 1:20 (Cd^{2+}: cysteine ester) were added simultaneously to the pink tellurium ion solution. The pH of the solution was raised to 7 by using HCl (0.10 M) and NH_3 (0.10 M) solutions after which the solution was then heated at 100 ^oC for 3 h. After completion of the reaction, excess methanol was added resulting in the reversible flocculation of the nanoparticles. The flocculate was separated from the supernatant by centrifugation. The resultant particles were dissolved in acetone for characterization.

The reaction procedure described above was carried for the TEA-capped CdTe nanoparticles with TEA (0.9548 g, 6.40 mmol) replacing the L-cysteine ethyl ester hydrochloride. All measurements shown in this chapter were performed without any post preparative size separation of nanocrystals.

7.2.3. Variation of cadmium Source

The above experimental procedure was repeated for both capping groups with the cadmium chloride being replaced by $Cd(CH_3COO)_2$: 0.0853 g; $Cd(NO_3)_2$: 0.075 g; $CdCO_3$: 0.052 g.

7.4 Results and discussion

Colloidal CdTe nanoparticles have been synthesized by the simultaneous addition of an aqueous solution or suspension of a cadmium source and ligand, to a freshly prepared oxygen-free NaHTe solution. The reaction was then refluxed at 100 ^{o}C for 3 h. The capping ligands used were cysteine and triethanolamine (TEA). The reactions are shown below in Scheme 7.1:

$$4\ NaBH_4 + 2\ Te + 7\ H_2O \xrightarrow[N_2,\ R.T]{2\ h} 2\ NaHTe + Na_2B_4O_7 + 14\ H_2 \quad (1)$$

$$NaHTe + CdX \xrightarrow[100\ ^{o}C,\ 3\ h]{Ligand} \text{Ligand-capped CdTe} + NaCl + HCl \quad (2)$$

$X = Cl^-, NO_3^-, CO_3^{2-}$ and CH_3COO^-

Scheme 7.1. Equation for the formation of ligand-capped CdTe nanoparticles at 100 ^{o}C (R.T = room temperature, Ligand = cysteine, TEA).

We have selected two ligands, cysteine and triethanolamine as capping groups to functionalise CdTe nanoparticles. The molecular structures of the cysteine and triethanolamine are shown in Figure 7.1.

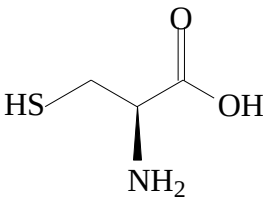

L-Cysteine

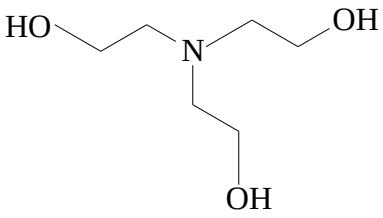

Triethanolamine

Figure 7.1. The molecular structures of cysteine and triethanolamine.

Cysteine has been reported as a capping group having shown better efficiency than mercaptopropionic acid (MPA) and thioglycolic acid (TGA) [22]. Cysteine is relatively inexpensive and has been shown to play a significant role in controlling the size of QDs [17]. There have been very few reports of the use of Triethanolamine (TEA) as a passivation agent. Our group has recently reported the synthesis of water soluble, crystalline triethanolamine capped CdSe nanoparticles [20].

7.4.1 Optical properties

Fig. 7.2 shows the absorption spectra of TEA and cysteine capped CdTe nanoparticles prepared under similar reaction conditions. The absorption peak at 264 (cysteine)(a) and 255 nm (TEA)(b) can be attributed to the Cd-ligand complex. Similar observations have been reported for water-soluble cysteine-capped CdS and CdSe nanoparticles [23,24]. The cysteine capped CdTe nanoparticles shows an absorption peak (439 nm) with a band edge at 523 nm, blue shifted in relation to bulk CdTe (863 nm) [25]. The TEA capped particles shows a very strong-ligand complex absorption peak with several low intensity peaks due to the absorption by nanoparticles. The inset of Fig. 7.2 shows the room temperature photoluminescence spectra of CdTe nanoparticles excited at 275 nm for the two surfactants. The emission maxima are observed at 418 nm (cysteine) and 415 nm (TEA) with a full width at half maximum (FWHM) of 92 and 97 nm respectively. There is very little difference in PL maxima position and intensity for both samples.

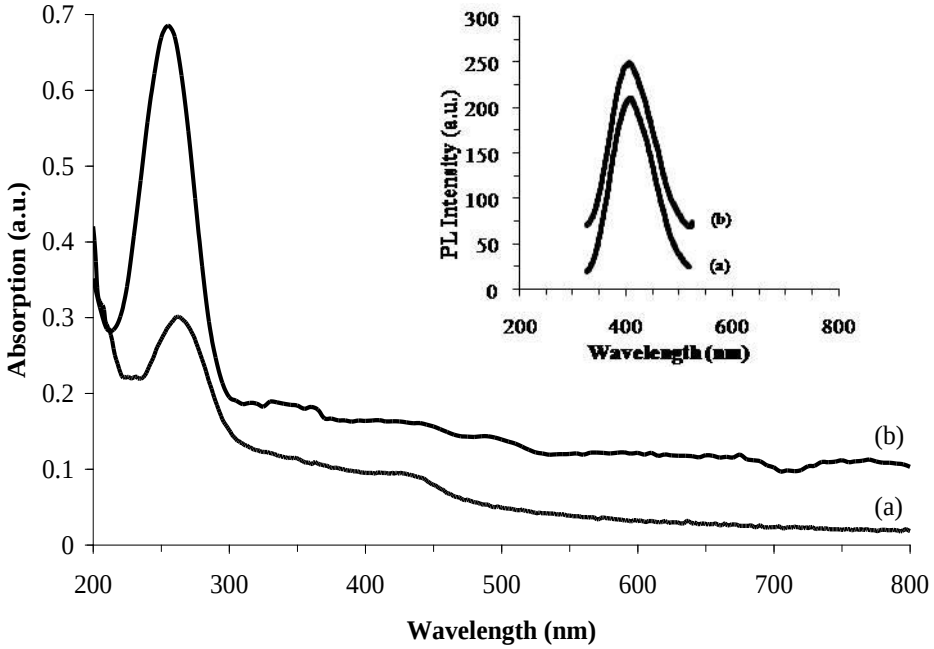

Fig. 7.2. UV-Vis absorption and inset, photoluminescence spectra of CdTe nanoparticles capped with (a) cysteine and (b) TEA.

7.4.1. Structural properties

Fig. 7.3 shows TEM and HRTEM images of CdTe particles capped with cysteine and TEA. Fig. 7.3a shows that cysteine capped CdTe particles are quasi-spherical in nature, with an average size of 3.07 ± 0.66 nm. The corresponding HRTEM image of the cysteine capped CdTe nanoparticles shown in Fig. 7.3b reveals the existence of distinct lattice planes confirming the crystallinity of particles. The lattice spacing of 3.60 Å is assigned to the (100) plane of hexagonal CdTe. The HRTEM image shows particles which are imperfectly aligned with some dislocations and stacking faults in the lattice visible (shown by arrows). The existence of particles within capping matrix makes it difficult to observe single particles. The TEA capped particles as shown

in Fig. 7.3c are also quasi-spherical with an average particle size of 3.26 ± 0.41 nm. The HRTEM image for the TEA capped particles (Figure 7.3d) reveals clearly observed lattice planes confirming the crystallinity of the CdTe nanoparticles. The lattice spacing of approximately 3.76 Å corresponds to the (111) plane of the cubic phase of CdTe. There are no discontinuities or stacking faults observed in the image of the particle.

The XRD pattern of the cysteine capped CdTe nanoparticles is shown in Fig. 7.4. Seven distinct diffraction peaks at 2θ values of 25.4^{o}, 27.0^{o}, 28.6^{o}, 37.4^{o}, 44.3^{o}, 48.5^{o} and 52.5^{o}, are observed corresponding to the respective (100), (002), (101), (102), (110), (103) and (112) diffraction planes of hexagonal CdTe (JCPDS card no. 19-0193). The high intensity of (002) peak indicates that the nanocrystals are elongated along the c-axis and the particles contain a large number of (002) planes, thus making that peak the dominant reflection in the first diffraction feature. This is in contrast to previous reports of CdTe nanoparticles via the aqueous method, where it yielded the cubic-zinc blende phase [26,27,28-29]. The hexagonal phase is usually obtained under the high-temperature organometallic route [30,31]. The X-ray diffraction pattern (Fig. 7.5) of the TEA-capped CdTe nanoparticles can be indexed to the cubic zinc-blende CdTe structure. The distinct diffraction peaks at 2θ values of 23.2^{o}, 27.7^{o}, 38.4^{o}, 46.2^{o}, 49.9^{o}, 57.1^{o}, 62.9^{o} and 72.3^{o} are corresponding to the respective (111), (200), (220), (311), (222), (400), (331) and (442) diffraction planes of CdTe (JCPDS card no. 15-0770). Other additional reflection peaks were observed which indicate the presence of impurities.

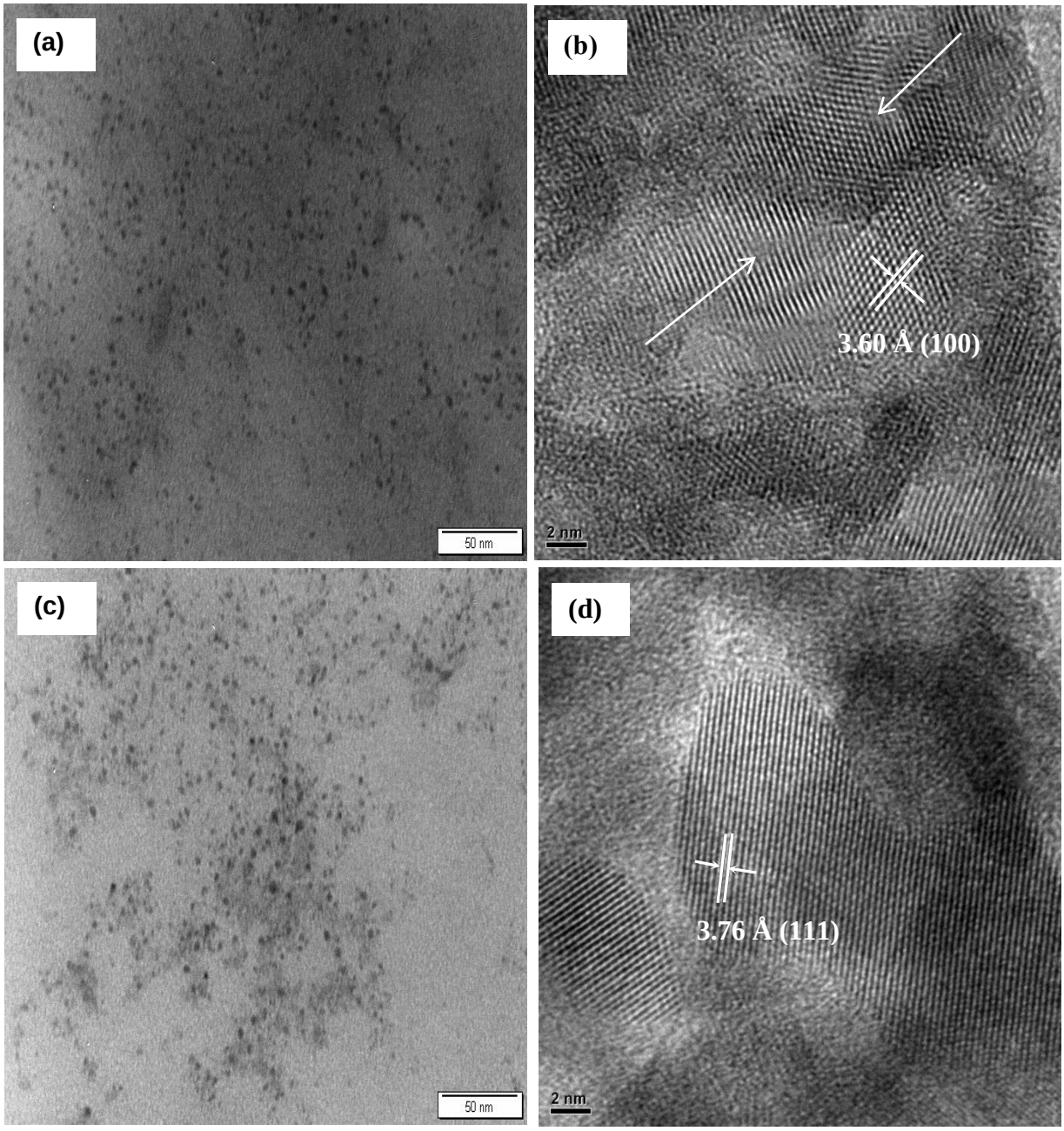

Fig. 7.3. TEM and corresponding HRTEM image of CdTe nanoparticles synthesized and capped with (a), (b) cysteine and (c), (d) TEA.

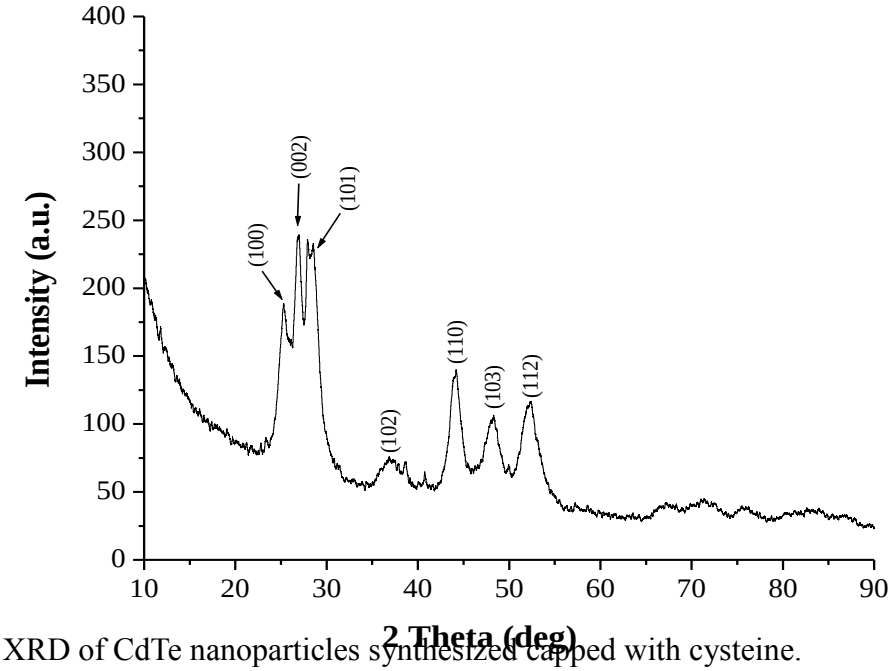

Fig. 7.4. XRD of CdTe nanoparticles synthesized capped with cysteine.

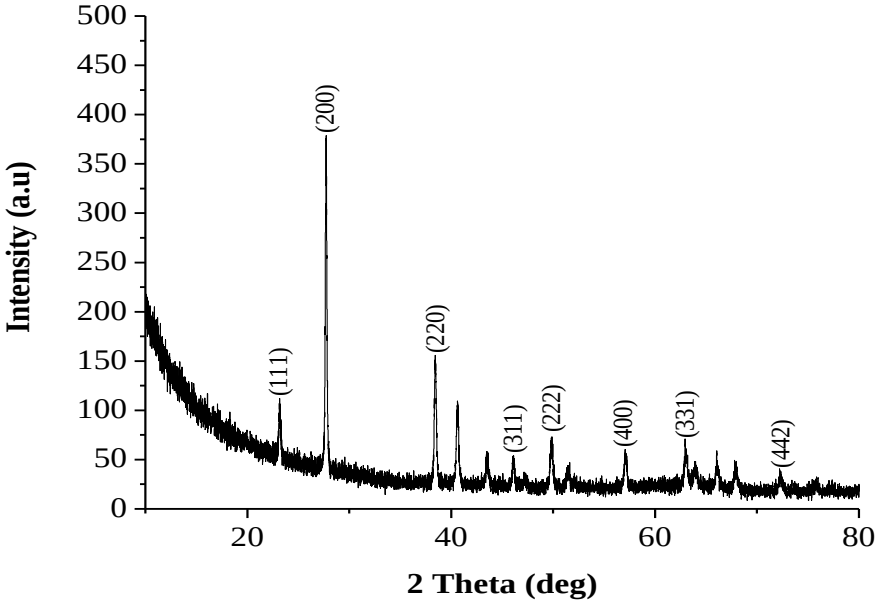

Fig. 7.5. XRD of CdTe nanoparticles synthesized capped with TEA.

The presence of cysteine on the surface of CdTe nanoparticles was investigated by the FT-IR spectral analysis. The FT-IR of the L-cysteine ethyl ester hydrochloride and the cysteine-capped CdTe nanoparticles are shown in Fig. 7.6. Generally, amino acids exist as zwitterions (internal salts) and exhibit spectra characteristic of both the carboxylate and primary amine salt. They show a NH_3^+ stretch (very broad), N-H bend (asymmetric/symmetric) as characteristic vibrations [32]. The amino acid cysteine is water soluble and would readily bind to the surface of CdTe via the thiolate linkage. On comparison of the two spectra, the most significant observation is the bands at 2471 and 950 cm^{-1} corresponding to the S-H stretching and bending mode which are sharp and long for the free cysteine molecule, but are broad and small in the spectrum for cysteine capped CdTe particles. This provides strong evidence for the surface binding of cysteine to CdTe particles via a Cd-S linkage. This may be attributed to the cleavage of most S-H bonds and the formation of a new S-Cd bond of the Cd-thiolate complex on the nanoparticle surface. It can also be observed that the bands at 1743 and 1223 cm^{-1} of cysteine which corresponds to the COO^- asymmetric and symmetric stretch, a band at 1473 cm^{-1} corresponding to N-H asymmetric bend are shifted to slightly lower wave numbers in the cysteine passivated CdTe nanoparticles, whereas the very broad band of NH_3^+ stretch observed in the 2735-3200 cm^{-1} is shifted to higher wavenumbers. The shift in the COO^- and NH_3^+ stretching position is probably due to a change in the dipole moment when cysteine binds on the metal surface with high electron density [33]. These observations confirm the capping of nanoparticles surface by cysteine i.e. the ester has been hydrolyzed during the reaction to produce the parent amino acid, which coordinates to the CdTe via the thiolate group [18]. The formation of TEA capped CdTe nanoparticles were further investigated by FT-IR. As shown in Fig. 7.7, the strong band at 2995-3606 cm^{-1} (O-H group vibration) and those at 1026 and 1045 cm^{-1} (C-O group vibration) in Fig. 7.7 are observed. The

bands at 2988-3658 cm^{-1} (O-H group vibration), 1028 and 1070 cm^{-1} are shifted to high wave numbers from their corresponding band of the free TEA ligand (Fig. 7.7b). It is inferred from the present results that the nitrogen atom of TEA coordinates with the Cd^{2+} ion on the CdTe QD surface, and the hydrophilic hydroxyl groups face outward and render CdTe QDs water-soluble [32].

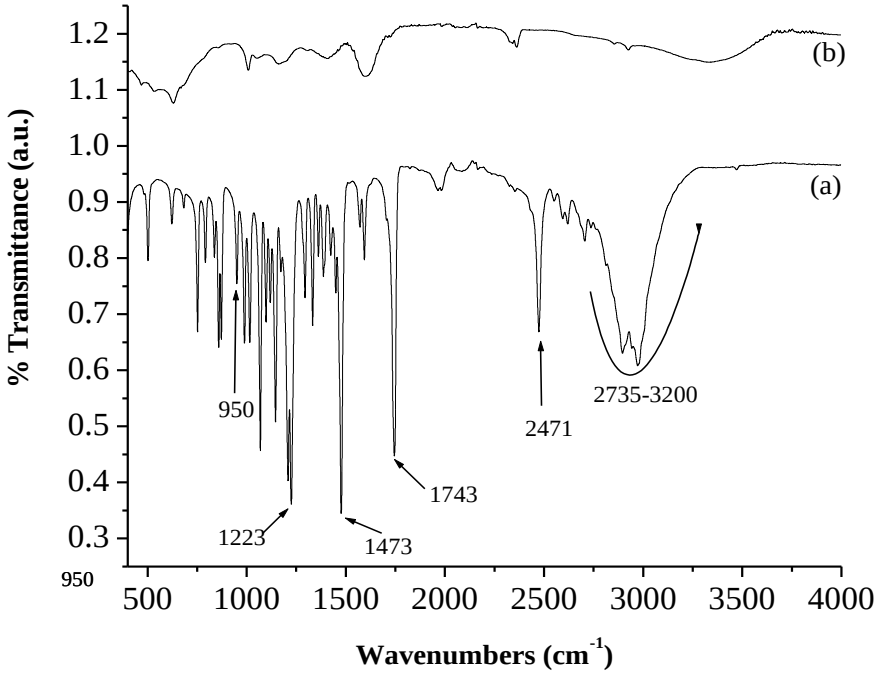

Fig. 7.6. FT-IR spectra of (a) L-cysteine ethyl ester hydrochloride and (b) CdTe capped with cysteine from $CdCl_2$ at pH 7 after 3 h reflux time.

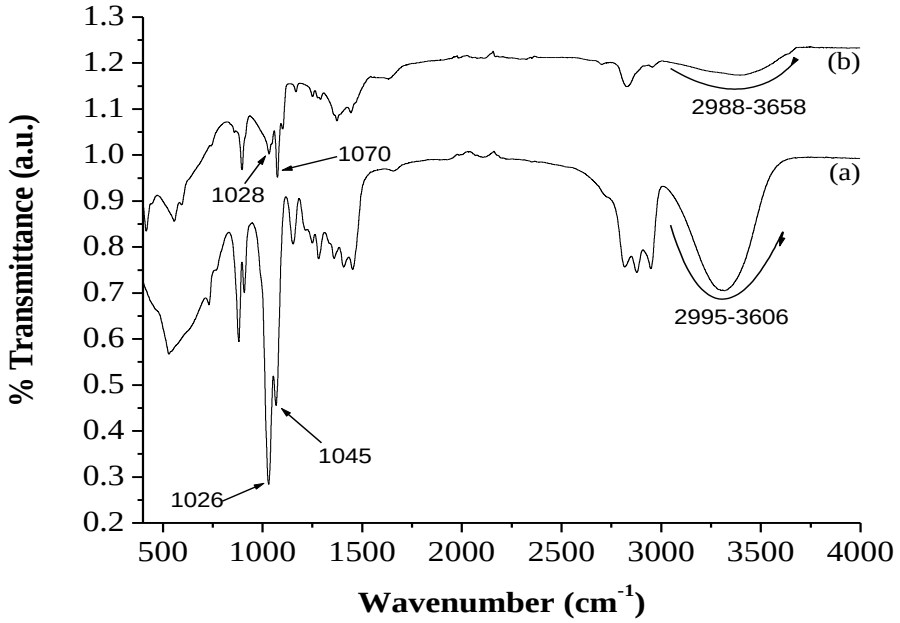

Fig. 7.7. FT-IR spectra of (a) TEA and (b) TEA capped CdTe nanoparticles from $CdCl_2$ at pH 7 after 3 h reflux time.

7.4.2. Variation of cadmium source

We have observed from our previous work on nanocrystalline CdTe, PbTe and CdSe that the cadmium or lead source plays an important role in determining the final morphology of the particles [34,35,36]. When cadmium chloride or nitrate was used as a source of cadmium, distinct spherical particles were observed. However when the carbonate was used, rod shaped particles were formed. For organically capped CdTe two growth mechanisms were proposed, one for the carbonate source and one for the other sources of cadmium. We decided to vary the cadmium source for the water soluble CdTe particles. Three further cadmium sources; cadmium acetate [$Cd(CH_3COO)_2$], cadmium nitrate [$Cd(NO_3)_2$] and cadmium carbonate ($CdCO_3$) were also used for the synthesis of water soluble cysteine capped CdTe nanoparticles. All the reactions were carried out using similar reaction conditions as that of the chloride salt.

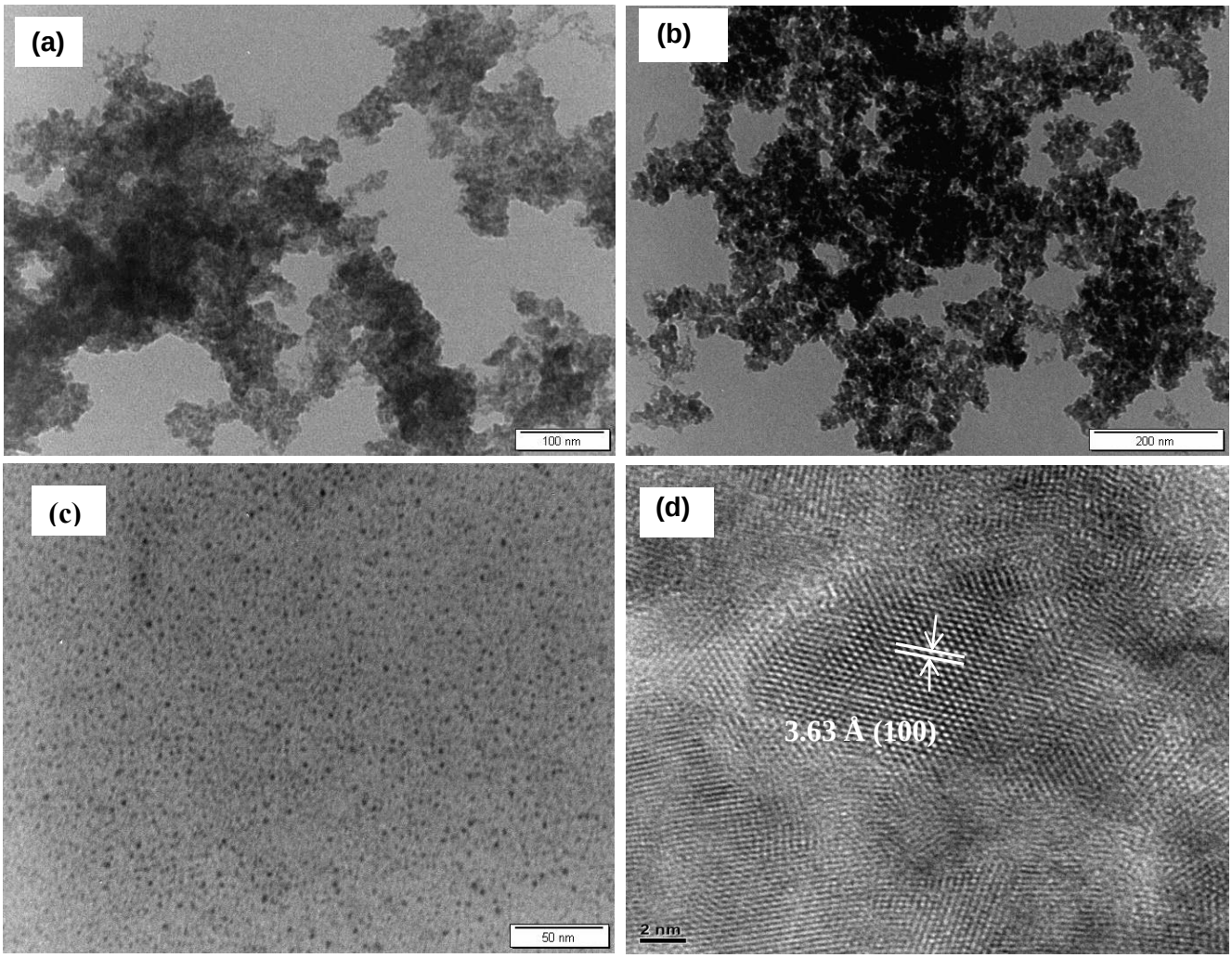

Fig. 7.8. TEM images of cysteine capped CdTe nanoparticles synthesized at pH 7 after time from different cadmium precursors (a) $Cd(CH_3COO)_2$, (b) $CdCO_3$, (c), $Cd(NO_3)_2$and (d) corresponding HRTEM of $Cd(NO_3)_2$.

The optical results of the cysteine and TEA capped CdTe nanoparticles obtained when using the acetate, carbonate and nitrate salts were similar to those obtained for the chloride source. The excitonic absorption peak due to the Cd-cysteine complex is evident in all samples. The morphology of the particles also remained unchanged. Spherical particles were observed for all cadmium sources (Fig. 7.8). The nitrate source gave particles which were well dispersed whereas the carbonate and acetate salts gave particles which were aggregated in the capping matrix. The average size of the particles obtained from the nitrate source is 3.11 ± 0.66 nm. The HRTEM

shows a well defined particle with distinct lattice fringes. The lattice spacing of 3.63 Å corresponds to the (100) plane of the hexagonal phase of CdTe. The TEA capped CdTe nanoparticles synthesized using the acetate and nitrate sources show spherical particles with an average particle size of 4.10 ± 0.81 nm and 3.26 ± 0.41 nm respectively (Figure 7.9a,c). However when $CdCO_3$ is used, spherical particles within the matrix of the capping agent were obtained (Fig. 7.9b). The nitrate source gave very well defined monodispersed particles. The HRTEM image (Figure 7.9d) shows the presence of a well defined particle. From this study it seems that the nitrate source gives well defined, monodispersed and crystalline particles.

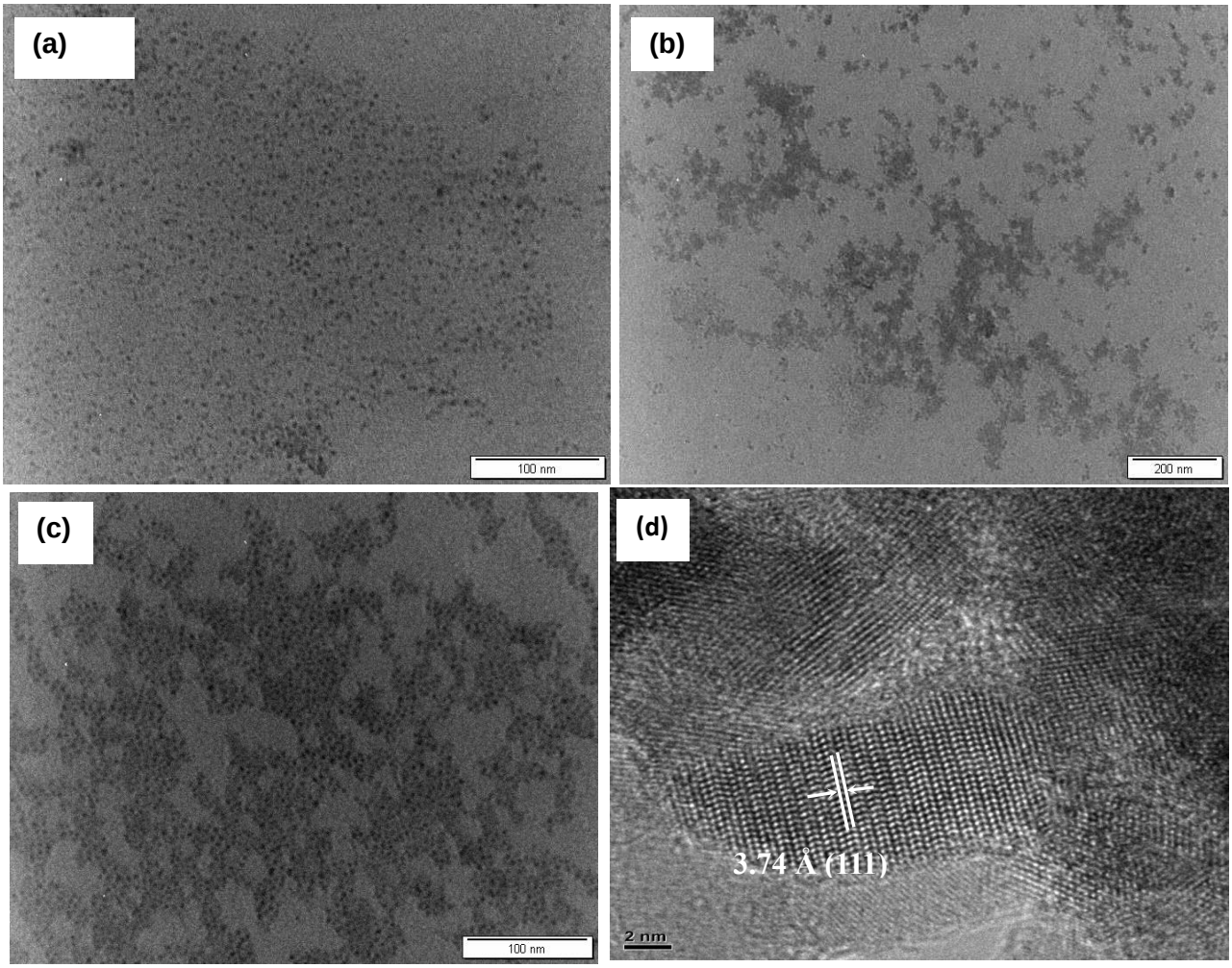

Fig. 7.9 TEM images of TEA capped CdTe nanoparticles synthesized at pH 7 after 3 h reflux time with different cadmium sources namely (a) $Cd(CH_3COO)_2$, (b) $CdCO_3$, (c) $Cd(NO_3)_2$. And (d) corresponding HRTEM.

7.5 Conclusions

Cysteine and triethanolamine capped CdTe nanoparticles have been synthesized via an aqueous route involving the reduction of selenium, followed by the simultaneous addition of the cadmium salt and capping agent. The results showed that both cysteine and TEA are effective capping groups for water soluble CdTe nanoparticles. The optical properties of the particles synthesized in both capping groups revealed absorption features due to the Cd-ligand complex. The

photoluminescence spectra showed reasonably narrow emission peaks. The cadmium salt was varied to study its effect on the morphology of the CdTe nanoparticles. The nitrate source gave well defined, crystalline, close to spherical nanoparticles. The FT-IR measurements confirmed the presence of the capping ligand on the surface of CdTe nanoparticles.

7.6 References

[1] D. Zhao, Z. Jimei, D. Quanxi, G. Ning, X. Shichao, S. Bo and B. Yuehua, *Chin. J. Chem.* Eng., **15** (2007) 791.

[2] X. Huang, L. Li, H. Qian, C. Dong and J. Ren, *Angew. Chem. Int. Ed*., **45** (2006) 5140.

[3] X. Li, J. Li, J. Tang, J. Kang and Y. Zhang, *J. Lumin*., **128** (2008) 1229.

[4] H. Mattoussi, J. M. Mauro, E. R. Goldman, G. P. Anderson, V. C. Sundar, F. V. Mikulec and M. G. Bawendi, *J. Am. Chem. Soc*., **122** (2000) 12142.

[5] J. Aldana, Y. A. Wang and X. Peng, *J. Am. Chem. Soc*., **123** (2001) 8844.

[6] D. M. Willard, L. L. Carillo, J. Jung and A. V. Orden, *Nano Lett*., **1** (2001) 469.

[7] D. V. Talapin, A. L. Rogach, I. Mekis, S. Haubold, A. Kornowski, M. Haase and H. Weller, *Colloids. Surf*., **202** (2002) 145.

[8] D. V. Talapin, A. L. Rogach, E. V. Shevchenko, A. Kornowski, M. Haase and H. Weller, *J. Am. Chem. Soc*., **124** (2002) 5782.

[9] N. Gaponik, D. V. Talapin, A. L. Rogach, K. Hoppe, E. V. Shevchenko, A. Kornowksi, A. Eychmuller and H. Weller, *J. Phys. Chem*., **106** (2002) 7177.

[10] J. Liu, Z. Shi, Y. Yu, R. Yang and S. Zuo, *J. Coll. Int. Sci*.**, 324** (2010) 278.

[11] P. T. K. Chin, J. W. Stouwdam, S. S. Bavel and R. A. J. Janssen, *Nanotech*, **19** (2008) 205602.

[12] D. Verma, A. R. Rao, V. Dutta, *Sol. Energy Mater. Sol. Cells*, **93** (2009) 1482.

[13] E. Ying, D. Li, S. Guo, S. Dong, J. Wang, *PLoS One*, **3** (2008), p. e2222.

[14] A. L. Rogach, L. Katsikas, A. Kornowksi, D. Su, A. Eychmuller, H. Weller, *Ber. Bunsen-Ges. Phys. Chem*., **100** (1996) 1772.

[15] L. Zou, Z. Gu, N. Zhang, Y. Zhang, Z. Fang, W. Zhu, X. Zhong, *J. Mater. Chem*., **18** (2008) 2807.

[16] M. S. Abd El-sadek, J. R. Kumar, S. M. Badu, *Curr. Appl. Phys*., **10** (2010) 317.

[17] M. Li, H. Zhou, H. Zhang, P. Sun, K. Yi, M. Wang, Z. Dong, S. Xu, *J. Lumin*., **130** (2010) 1935.

[18] D. Deng, Y. Qin, X. Yang, J. Yu, Y. Pan, *J. Cryst. Growth*., **296** (2006) 141.

[19] S. O. Oluwafemi, N. Revaprasadu, A. J. Ramirez, *J. Cryst. Growth*., **310** (2008) 3230.

[20] S.O. Oluwafemi, N. Revaprasadu, O.O. Ayeyemi, *Colloids. Surf. B. Biointerfaces*.,**79** (2010) 126.

[21] N. N. Dlamini, V. S. R. Rajasekhar Pullabhotla and N. Revaprasadu, *Mat. Lett*., 65 (2011) 1283.

[22] M. Idowu, J. Y. Chen, T. Nyokong, *New J. Chem*., **32** (2008) 290.

[23] A. Chatterjee, A. Priyam, S. K. Das, A. Saha, *J. Coll. Interf. Sci*., **294** (2006) 334.

[24] D. Hayes, O. L. Micic, M. T. Nenadovic, V. Swayambunathan, D. Meisel, *J. Phys. Chem*., **93** (1989) 4603.

[25] S. Ma, J. Seo, W. Yu, Q. Yang, B. Tabibi, D. Temple, N. Min, S. Jung, W. Kim, *J. Phys*. **109** (2008) 012025.

[26] M. Green, H. Harwood, C. Barrowman, P. Rahman, A. Eggeman, F. Festry, P. Dobson, T. Ng, *J. Mater. Chem*., **17** (2007) 1989.

[27] Z. Tang, N.A. Kotov, M. Giersog, *Science*, **297** (2002**)** 237.

[28] X. Cao, X. Lan, Y. Guo, C. Zhao, *Crystal. Growth. Design*., **8** (2008) 575.

[29] T. Wang, Z. Jin, Y. Shi, W. Li, J. Yang, *Crystal. Growth. Design*., **9** (2009) 5077.

[30] S. Kumar, T. Nann, *Chem. Commun*., **19** (2003) 2478.

[31] D. Kim, H. D. Jang, E. J. Kim, K. Koo, *Ultramicroscopy*, **108** (2008) 1278.

[32] D. L. Pavia, G. M. Lampman, G. S. Kriz, Introduction to Spectroscopy, 3rd ed., USA, 2001.

[33] A. Santosh, B. K .C. Remant, N. Dharmaraj, N. Bhattarai, C.H. Kim, H.Y. Kim, Spectrochim. *Acta Part A***, 63** (2006) 160.

[34] N. N. Maseko, N. Revaprasadu, V. S. R. Rajasekhar Pullabhotla, R. Karthik, P. O'Brien, *Mater. Lett*., **64** (2010) 1037.

[35] N. Ziqubu, K. Ramasamy, Pullabhotla V. S. R. Rajasekhar, N. Revaprasadu, P. O'Brien, *Chem. Mater*., **22** (2010) 3817.

[36] N. Mntungwa, Pullabhotla V. S. R. Rajasekhar, N. Revaprasadu, *Mater. Chem. Phys*., **126** (2011) 500.

8.0 Recommendations and Publications

8.1 Recommendations for Future Work

The route is an effective one for the synthesis of nanoparticles. Future work on this route could include:

- Synthesis of other metal chalcogenide nanoparticles e.g AsE (E = S, Se and Te)
- A detailed investigation into the growth mechanism of the particles.
- Use of other organic ligands e.g decaylamine and other water soluble ligands e.g starch, polyvinyl acetate (PVA) as capping groups.
- The application of these nanoparticles in Li-ion batteries and solar cells.

Overall the study opens up many avenues for further research into other nanoparticles.

8.2 Publications

(1) Nhlakanipho Mntungwa, Viswanadha Srirama Rajaserkhar Pullabholta, Neerish Revaprasadu, A facile route to shape controlled CdTe nanoparticles, *Mat. Chem. Phys*. **126** (2011) 500–506.

(2) Nhlakanipho Mntungwa, Viswanadha Srirama Rajasekhar Pullabhotla, Neerish Revaprasadu, Facile Synthesis of Organically Capped CdTe Nanoparticles, *J. Nanosci. Nanotechnol*. **12** (2012) 2640-2644.

(3) Nhlakanipho Mntungwa, Viswanadha Srirama Rajasekhar Pullabhotla, Neerish Revaprasadu, A simple route to bismuth nanoparticles in the form of dots, branched nanorods and self assembled cubes, *Mater. Lett*. **92** (2013) 220–223.

(4) Nhlakanipho Mntungwa, Pullabholta V S R Rajaserkhar, Neerish Revaprasadu, Facile synthesis of cysteine and triethanolamine capped CdTe nanoparticles, *Colloids and Surfaces B: Biointerfaces* **101** (2013) 450– 456.

(5) Nhlakanipho Mntungwa, Viswanadha Srirama Rajasekhar Pullabhotla, Neerish Revaprasadu, A facile hybrid route to luminescent ZnTe nanoparticles, *Mater. Lett*. **81** (2012) 108-111.

(6) Nhlakanipho Mntungwa, Pullabhotla V.S.R. Rajasekhar, Karthik Ramasamy and Neerish Revaprasadu, A Simple Route to Bi_2Se_3 and Bi_2Te_3 Nanocrystals, *Superlattices and Microstructures,* **69** (2014) 226-230.

8.3 Conferences attended

(1) **Science Faculty Postgraduate Symposium at UZ.**

Poster presentation title: The synthesis of antimony nanoparticles via a hybrid route.

(2) **NanoAfrica 2012 at the University of Free State.**

Poster presentation title: Effect of Te reduction time on the synthesis of CdTe Nanoparticles.

(3) **11th International Conference on Frontiers of Polymers and Advanced Materials** held from 22 to 27 May 2011 at UP.

Poster presentation title: **A facile route to functionalized CdTe nanoparticles**

(4) **NRF Winter Research School** held from 24 June 2011-17 July 2011 at NMMU George campus**.**

(5) **Spring School on TEM and HRTEM** held from 27-30 September 2011 at UKZN (Westville campus).

(6) **South African Nanoscience and Nanotechnology Summer School** held from 27 November to 2 December 2011 at NMMU PE campus.